CANCER DIAGNOSTICS USING DYNAMIC NEAR-INFRARED OPTICAL IMAGING AND FLUORESCENT CONTRAST AGENTS

A Dissertation

by

MIKHAIL GURFINKEL

Submitted to the Office of Graduate Studies of
Texas A&M University
in partial fulfillment of the requirements for the degree of

DOCTOR OF PHILOSOPHY

May 2004

Major Subject: Chemical Engineering

CANCER DIAGNOSTICS USING DYNAMIC NEAR-INFRARED OPTICAL IMAGING AND FLUORESCENT CONTRAST AGENTS

A Dissertation

by

MIKHAIL GURFINKEL

Submitted to Texas A&M University
in partial fulfillment of the requirements
for the degree of

DOCTOR OF PHILOSOPHY

Approved as to style and content by:

Eva M. Sevick-Muraca (Co-Chair of Committee)	Chun Li (Co-Chair of Committee)
Daniel F. Shantz (Member)	Lihong Wang (Member)
	Kenneth R. Hall (Head of Department)

May 2004

Major Subject: Chemical Engineering

ABSTRACT

Cancer Diagnostics Using Dynamic Near-Infrared Optical Imaging and Fluorescent Contrast Agents. (May 2004)

Mikhail Gurfinkel, B.S., University of Oklahoma

Co-Chairs of Advisory Committee: Dr. E.M. Sevick-Muraca
Dr. C. Li

A new optical imaging modality has been developed for small animal *in vivo* imaging of near-infrared fluorescence resulting from fluorescent contrast agents specifically targeted to molecular markers of cancer. The imaging system is comprised of an intensified charge-coupled device (ICCD) for the detection of ultra-low levels of re-emitted fluorescence following the delivery of an expanded beam of excitation light. The design of the ICCD detection system allows for both continuous wave (CW) and frequency-domain modes of operation. Since the accurate acquisition of frequency-domain photon migration (FDPM) data is important for tomographic imaging, the imaging system was also validated using experimentally obtained FDPM measurements of homogenous turbid media and diffusion theory to obtain estimates of the optical properties characteristic of the media. The experiments demonstrated that the absorption and reduced scattering coefficients are determined least accurately when relative measurements of average light intensity I_{DC}^{rel} are employed either alone or in a combination with relative modulation amplitude data I_{AC}^{rel} and/or relative phase shift data θ^{rel}. However, when FDPM measurements of θ^{rel} are employed either alone or in

combination with I_{AC}^{rel} data, the absorption and reduced scattering coefficients may be found accurate to within 15% and 11%, respectively, of the values obtained from standard single-pixel measurements; a result that suggests that FDPM data obtained from an ICCD detection system may in fact be useful in tomographic imaging.

Furthermore, intensified-detection allows for sub-second exposure times, permitting the acquisition of dynamic fluorescence images immediately following administration of the contrast agent. Experimental results demonstrate that when coupled with a suitable pharmacokinetic model describing targeted dye distribution throughout the body, dynamic fluorescence imaging may be used to discriminate spontaneous canine adenocarcinoma from normal mammary tissue. A separate experiment demonstrates that pharmacokinetic analysis of dynamic fluorescence images enables one to estimate the rate constant governing Kaposi's sarcoma tumor uptake of an $\alpha_v\beta_3$ integrin-targeted dye and integrin receptor turnover rate. The rate constant for uptake was calculated to be 0.16-sec^{-1} while the turnover rate of the integrin receptor was estimated to occur within 24-hours.

To my grandmother

ACKNOWLEDGEMENTS

The completion of a dissertation is a significant achievement that, although an individual accomplishment, cannot be realized without the support of numerous people. Thus, my sincere gratitude goes out to family, friends, and academics that I have had the good fortune to work with in pursuit of the doctoral degree. First and foremost I would like to thank my major advisor, Dr. Eva Sevick-Muraca, whose guidance and instruction has shaped this dissertation and whose courage to pursue ideas considered by some to be outside the realm of chemical engineering has allowed me to become part of highly productive multi-disciplinary collaborations and helped me develop into a good scientist and engineer. I would also like to particularly thank my co-advisor, Dr. Chun Li, who gave me the opportunity to apply engineering knowledge and principles to solve challenging problems relevant to the development of novel fluorescent contrast agents for near-infrared optical imaging. My committee members, Dr. Daniel Shantz, Dr. Lihong Wang, and Dr. Theresa Good, are deserving of a special thanks for offering good advice at critical points along the way.

Many others have contributed in significant ways to the completion of this work. I owe a debt of gratitude to Shi Ke who, after learning the operation of the ICCD imaging system, provided me with more data than I knew what to do with. I also wish to thank additional collaborators from M.D. Anderson Cancer Center, namely QingPing Wu, Xiaoxia Wen, Wei Wang, and Xianyi Cao, whose work on the small animal models of carcinoma and chemical synthesis of the fluorescent probes directly contributed to the

results presented in Sections 6 – 8. Needless to say, without the contributions of these collaborators, this dissertation would not have been completed.

Others have been kind enough to contribute their valuable time and effort to the work presented in this dissertation. I wish to thank Randy Marek and Nathan Okonski for assistance in fabricating the instrumentation. I am grateful to Alan Thompson, Daniel Hawrysz, and Jeffery Reynolds who collected the data on canine imaging of spontaneous breast cancer detailed in Section 5. Furthermore, I am appreciative of the assistance of Tianshu Pan who performed the single-pixel measurements presented in Section 4.

I would like to thank past and present members of the Photon Migration Laboratories with whom I have had the good fortune of working. I would especially like to thank Alan Thompson, Daniel Hawrysz, Jessica Houston, Anuradha Godavarty, and Steven Richter who not only provided invaluable advice in times of confusion but also have become treasured friends.

I would be remiss not to acknowledge the support of my family – my parents, grandparents, brother, and sister have exemplified the meaning of love. Finally, I will eternally be indebted to my wife Brenda who has supported me in this momentous endeavor in every possible sense. She, above all others, deserves my deepest gratitude for I could not have done this without her.

TABLE OF CONTENTS

Page

Page

Page

LIST OF FIGURES

Page

Page

Page

Page

Page

Page

Page

LIST OF TABLES

Page

NOMENCLATURE

Abbreviations:

AC	alternating current
A/D	analog-to-digital
CCD	charge-coupled device
CT	computed tomography
CW	continuous-wave
DC	direct current
EES	extravascular, extracellular space
EGF	epidermal growth factor
EGFr	epidermal growth factor receptor
FDPM	frequency-domain photon migration
FFT	fast Fourier transform
fps	frames per second
GPIB	general purpose interface bus
HPPH-car	modified hexylpyropheophorbide modified with carotene
HSA	human serum albumin
ICCD	intensified charge-coupled device
ICG	indocyanine green
IMAG	imaginary component
ITTC	indotricarbocyanine
MCP	micro-channel plate
MMP	matrix metalloprotease
NIR	near-infrared
PDT	photo-dynamic therapy
PET	positron-emission tomography
REAL	real component
RGD	arginine-glycine-aspartic acid
SNR	signal-to-noise ratio
TDPM	time-domain photon migration
Tf	transferrin

Symbols:

α_o	one-half of detector acceptance angle
α	complex rate constant, pharmacokinetic parameter
β	complex rate constant, pharmacokinetic parameter
ε	extinction coefficient
κ	non-radiative relaxation rate
Γ	radiative relaxation rate
Φ	photon fluence rate
ϕ	fluorescence quantum efficiency
θ	phase lag of intensity modulated light
η	phase delay
ρ	surface-projected source-detector separation distance
τ	fluorescence lifetime
μ_a	absorption coefficient
μ_s'	reduced scattering coefficient
ω	angular modulation frequency
A	proportionality constant
A	pre-exponential pharmacokinetic parameter
B	pre-exponential pharmacokinetic parameter
c	speed of light in medium of interest
C_B	concentration of dye in blood
C_T	concentration of dye in tissue
C_{EES}	concentration of dye in extravascular, extracellular space
C_C	concentration of dye in cellular compartment
D	diffusion coefficient
g	mean cosine of scattering angle
G	modulated compounded gain at intensifier
i	principal square root of -1
I_{AC}	modulation amplitude of intensity modulated light
I_{DC}	steady-state intensity
k_p	rate constant for dye distribution from blood to tissue or EES
k_r	reflux rate constant for distribution of dye from tissue or EES into blood
k_{el}	rate constant for elimination
k_c	rate constant for distribution of dye from EES into cellular compartment
l_s	boundary at which photon fluence rate tends to zero
L	detected modulated signal at intensifier
n	refractive index
N_d	dark count
N_r	read noise
QE	quantum efficiency

Symbols continued:

r	position
R	diffuse reflectance
R	rate constant for distribution of dye from EES into cellular compartment
R_{eff}	effective reflection coefficient
$R_{Fresnel}$	Fresnel reflection coefficient
S	isotropic photon source density
S_{obs}	observed steady-state signal at intensifier
t	time
w	weighting function

1. INTRODUCTION

Non-invasive imaging of the human body is of great importance in medicine and plays a critical role in the early detection and intervention of disease.[1] A number of current imaging modalities such as conventional x-ray and nuclear imaging are employed for the diagnosis of diseases such as breast cancer, thyroid disease, and diseases of the gastro-intestinal tract. While these techniques vastly improve the overall odds of survival following diagnosis,[1,2] they nonetheless suffer from a number of shortcomings. Techniques employing x-rays utilize ionizing radiation and nuclear techniques employ contrast agents that are radioactive, and thus, potentially hazardous especially for repeated use. In addition they may also be expensive to implement and are generally non-portable. Additionally, because x-rays provide anatomical information, that is, images of tissue structure, and because nuclear imaging methods require high concentrations of contrast agents, neither method is particularly adept at providing functional information or information at a molecular level.

Near infrared (NIR) optical imaging, a technology emerging over the past quarter century, has garnered a considerable amount of interest for possible applications in medicine. Among them, optical techniques may serve as diagnostic tools to identify malignant or precancerous lesions or to assess response to treatment; as surgical tools to identify sentinel lymph nodes or delineate the margins for tumor resection; and as a research tool to help identify possible molecular targets for highly specific delivery of

---

This dissertation follows the style of *Journal of Biomedical Optics*.

diagnostic and therapeutic agents. Moreover, optical imaging methods are particularly appealing because they overcome the aforementioned shortcomings of conventional techniques, offering a potentially inexpensive, non-ionizing alternative or adjunct imaging technology.

An optical imaging technique of particular interest employs an intensified charge-coupled device (ICCD) detection system for the acquisition of ultra-low level light signals. The ICCD serves as an area detector of surface reflectance and, as such, allows for the collection of a large amount of data from a relatively large surface area in a relatively short period of time. As a result, this system lends itself to possible future clinical applications. This dissertation describes the development of an ICCD detection system and its use in a number of subsequent animal studies aimed at evaluating the use of optical imaging for cancer detection. Specifically, because most clinically relevant applications of optical imaging require the use of exogenous contrast agents due to a lack of intrinsic contrast, the experiments are designed to evaluate the efficacy of novel targeted fluorescent contrast agents for *in vivo* imaging of carcinogenesis. Thus, a synergistic collaboration between engineers focused on instrumentation development and organic chemists devoted to contrast agent development must necessarily occur before NIR optical imaging can be established as a bona fide imaging modality for cancer diagnostics. For this reason, the small-animal imaging studies described herein represents a collaboration with scientists at the University of Texas M.D. Anderson Cancer Center (MDACC) who developed the targeting fluorescence contrast agents, maintained the animal subjects, and produced the small animal models of carcinogenesis.

While the work presented in this dissertation focuses on the development of an optical imaging instrument and pharmacokinetic models to describe contrast agent distribution *in vivo* for the purposes of evaluating novel targeting fluorescent contrast agents, it is not the intent of the author to comment on the chemistry and the development of these novel fluorescent contrast agents; that portion of the work was conducted entirely by collaborators at MDACC, under the direction of Dr. Chun Li. Therefore, where appropriate, the reader is referred to other works detailing the chemistry and development of the contrast agents. Instead, the subsequent experimental work is designed to validate the instrumentation, the proposed theories, and evaluate the novel contrast agents solely for purposes of diagnostic imaging.

The dissertation is organized as a series of sections, each section independent of the others. This first section presents a brief motivation for near-infrared optical imaging. Section 2 provides a background on contrast-enhanced optical imaging, including the current state of fluorescent contrast agents and the differing approaches employed to acquire fluorescence measurements. Section 3 details the instrumentation employed in optical imaging and focuses specifically on the ICCD system used for the acquisition of pharmacokinetic and FDPM data presented in the subsequent sections.

Section 4 begins the sections describing experimental work acquired during the author's tenure at the Photon Migration Laboratories at Purdue University and later Texas A&M University. Section 4 summarizes the experimental work used to characterize the ICCD instrumentation, verifying accurate FDPM data acquisition for the purposes of estimating optical properties of tissue-like turbid media. As of the time of

the writing of this dissertation, the body of the work presented in Section 4 has been submitted for publication consideration to *Journal of Biomedical Optics*.

Beginning with Section 5, NIR fluorescence optical imaging studies employing animal subjects are discussed. Because much of the clinical work, including all animal studies, presented in this dissertation represents a collaborative research effort, it is appropriate to acknowledge the work of the collaborators. Therefore, where appropriate, the work of the collaborators is noted so that the author's contribution can be kept in proper context. Specifically, Section 5 presents experimental studies using a compartmental pharmacokinetic analysis of *in vivo* fluorescence data following intravenous administration of contrast agents to discriminate tumor from normal tissue in a canine model of spontaneous breast cancer. The results, which appeared in the journal *Photochemistry and Photobiology*, (vol. 72, pp. 94-102, 2000) represent the first time pharmacokinetics of fluorescent contrast agents have been used to discriminate diseased from normal tissue.

Section 6 expands upon the pharmacokinetic model developed in the analysis of the studies presented in Section 5. This expanded three-compartment pharmacokinetic model is then used to evaluate the molecular specificity of an integrin receptor-targeted fluorescent contrast agent. As of the time of the writing of this dissertation, the work within this section has been submitted for publication consideration in *Nature Biotechnology*.

Section 7 presents experimental work investigating fluorescence imaging of the epidermal growth factor receptor for diagnostic imaging of breast cancer. The

experimental work within this section has appeared in part in the *Proceedings of the SPIE* (vol. 4967, pp. 108-116, 2000) and has been accepted for publication and will appear in the journals *Cancer Research* and *Disease Markers* in November, 2003.

Section 8 finalizes the experimental studies with some preliminary results on continuous wave (CW) fluorescence imaging studies of bone and prostate cancer, and preliminary results on FDPM imaging of breast cancer, bone, and prostate cancer, studies conducted in collaboration with researchers at M.D. Anderson Cancer Center. The final section, Section 9, concludes the dissertation with a brief summary and suggestions for future work in the area of *in vivo* fluorescence imaging. Figure 1.1 provides the organization of this dissertation.

The work presented in this dissertation has several significant implications. First, the studies of Section 4 demonstrate that optical imaging, particularly frequency-domain photon migration (FDPM) imaging, may be used to accurately determine optical properties of tissue-like scattering media. FDPM imaging differs from conventional CW imaging in that, in addition to capturing the average light intensity of the detected signal, it provides time-resolved measurements, or measurements that reflect the time-dependent propagation of the detected light wave through the medium. The added information provided by FDPM measurements enable the mathematical recovery of optical properties characteristic of the medium. The results suggest that area measurements of FDPM may be used to extract optical properties of biological tissue which may infer anatomical and physiological status. Second, the studies presented in Sections 5-7 demonstrate that optical imaging can be easily implemented in animal

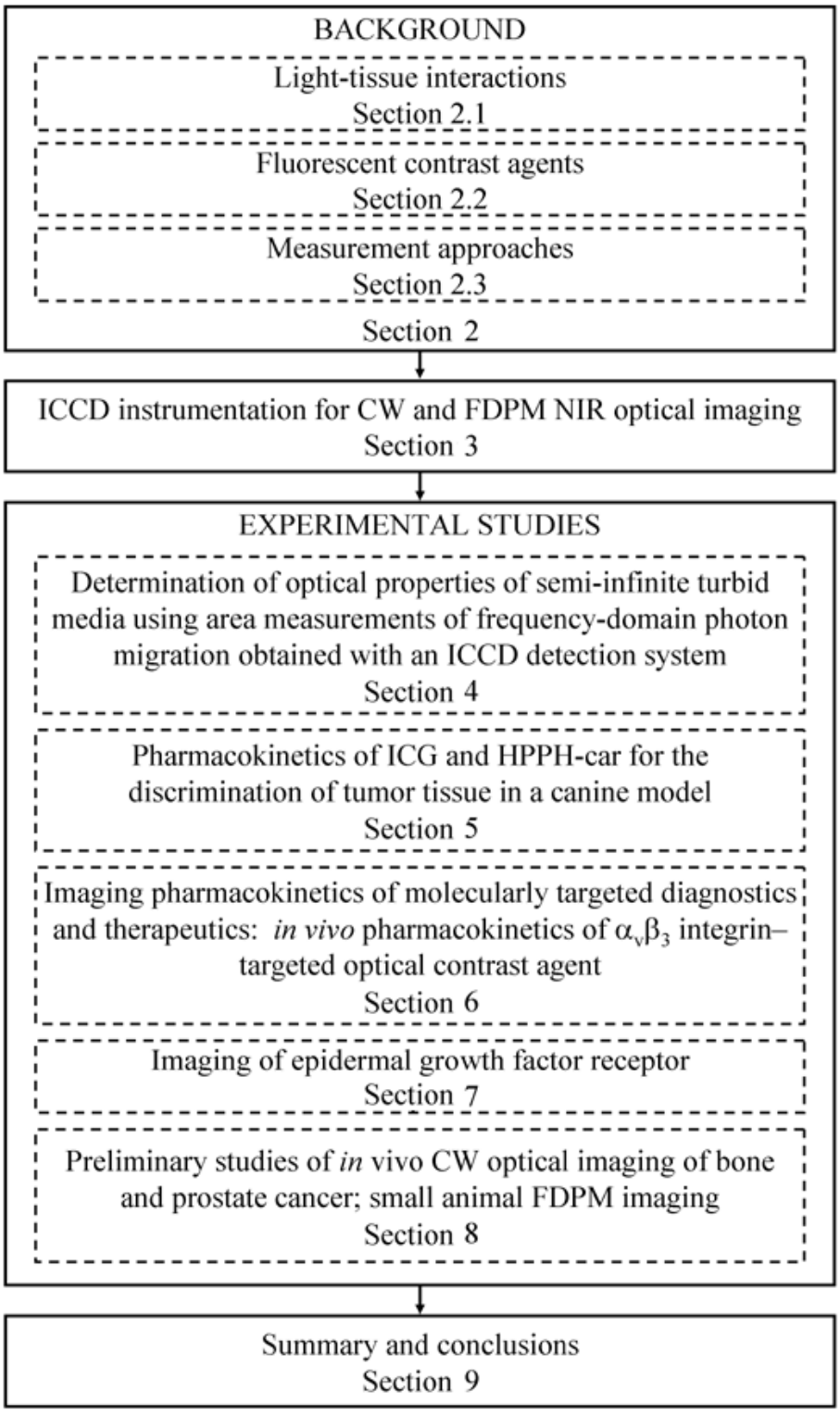

Figure 1.1. Organization of dissertation.

studies in order to elicit relevant data to evaluate a contrast agent's efficacy in diagnostic imaging. Finally, the studies of Section 6 demonstrate that the pharmacokinetic analysis of fluorescence data may be used to not only infer a contrast agent's specificity for its intended target, but also to potentially evaluate *in vivo* molecular phenomena such as cell-surface receptor expression level and turnover rate, important factors for the design and development of novel targeted cancer therapeutics.

2. BACKGROUND: CONTRAST-ENHANCED OPTICAL IMAGING

2.1 Light-Tissue Interaction

A number of endogenous light absorbing molecules abound in biological tissue. The absorbance spectra for a number of these chromophores, including oxy- and deoxyhemoglobin, melanin, and water, are shown in Figure 2.1. As a result, tissue is dense and opaque to most forms of electromagnetic radiation. There are, however, a number of notable exceptions. Most biological tissue is transparent to x-rays and gamma rays, for instance, and therefore, it is readily imaged using a number of techniques such as conventional x-ray imaging, x-ray computed tomography (CT), conventional nuclear imaging, and positron-emission tomography (PET). Regrettably, these methods suffer from a number of shortcomings, including the use of ionizing or radioactive radiation, non-portability, and expense of operation. Fortunately, near-infrared optical imaging is an emerging technology that overcomes these limitations.

Near-infrared optical imaging utilizes light in the 700 – 900-nm wavelength range to probe tissue. Because light in this wavelength range is minimally absorbed by the primary endogenous chromophores[3] (see Figure 2.1), it is predominantly scattered and may travel through several centimeters or more before it is finally re-emitted or extinguished by absorption. The degree of scattering and absorption is described by the inverse of the mean free path before a scattering or absorption event, denoted by μ_s' and μ_a, respectively. Because scattering and absorption are functions of the local environment, and diseased tissue may reside in different biochemical environments

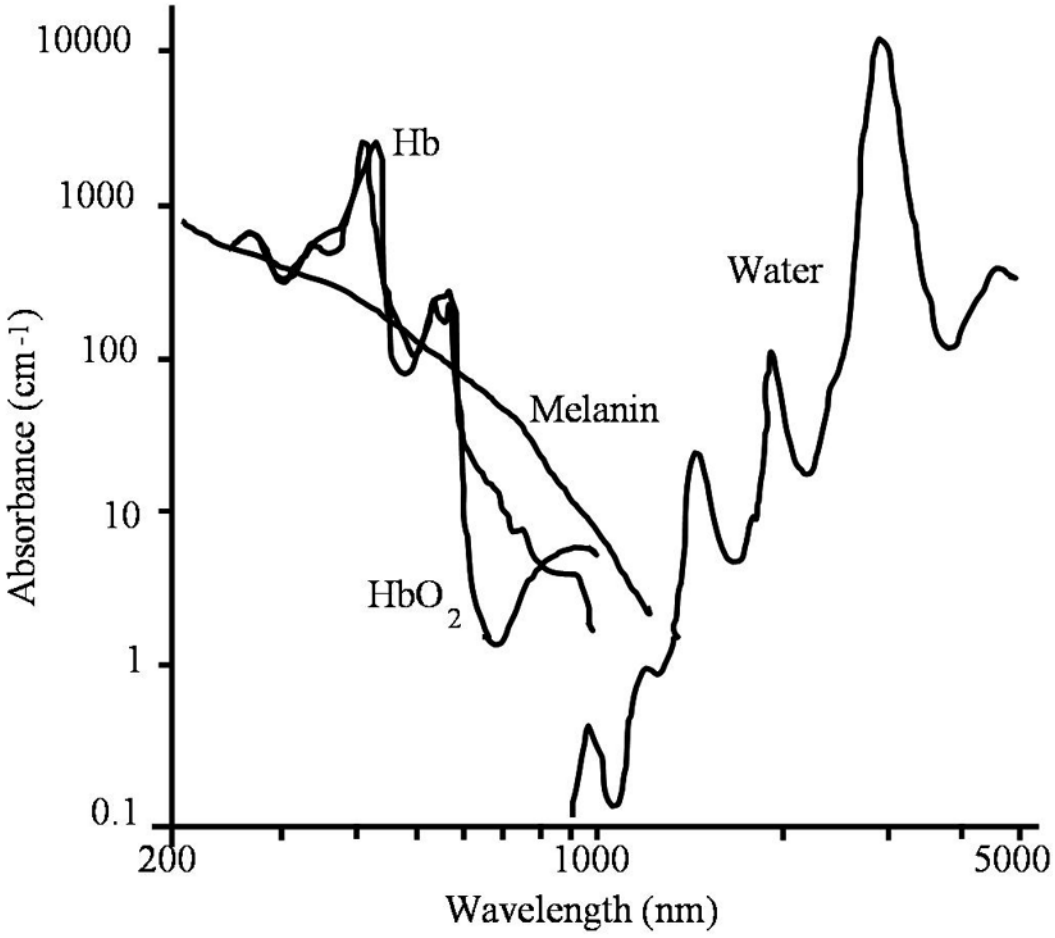

Figure 2.1. Typical absorbance spectra of tissue. Reproduced from Lim and Soter.[3]

resulting in different optical properties, interior maps of the optical properties μ_s' and μ_a can in theory provide the size and position of heterogeneous volumes including tumors. Unfortunately, previous work has demonstrated that the difference in optical properties between normal and diseased tissues may be statistically insignificant,

especially at the early stages of tumor development.[4] However, this potential setback may be overcome by use of fluorescent dyes to improve optical contrast.[5,6]

When fluorescent agents are used in conjunction with conventional optical imaging techniques, the properties of the dye can be used to help establish regions of diseased tissue. If the dye is designed and formulated to exhibit molecular specificity for tumor associated markers or targets, fluorescence-enhanced optical imaging can be a very powerful diagnostic tool. Thus, the success of an optical imaging technique for diagnostic imaging will ultimately require a synergistic union between organic chemistry and engineering for contrast agent and for instrumentation design and development, respectively.

2.2 Fluorescence Contrast Agents

To improve optical contrast in near-infrared optical imaging, fluorescent contrast agents may be employed. Fluorescence refers to the process by which certain molecules absorb energy in the form of light of a particular wavelength and re-emit light of a lower energy and longer wavelength. When light of a certain wavelength encounters a fluorophore (in this case a molecule of the dye) electrons are said to be 'excited' to a higher electronic level. The 'relaxation' of these electrons back to their ground state can occur non-radiatively (without the emission of photons) or result in emissions of photons known as fluorescence (see Fig. 2.2). The average length of time a fluorophore remains in the excited state is the lifetime, τ , and can be calculated as $\tau = 1/(\kappa + \Gamma)$ where κ and Γ are the rates for non-radiative and the radiative relaxation.[7] Furthermore, the relative amount of fluorophores that 'relax' back to the ground state via fluorescence is known as

the quantum efficiency, ϕ, and can be calculated as the ratio of rate constants $\phi=\Gamma/(\kappa+\Gamma)$.[7] The absorption properties due to the presence of fluorophore, $\mu_{a_{xf}}$, and the fluorophore lifetime, τ, may further be used to characterize the nature of tissue.

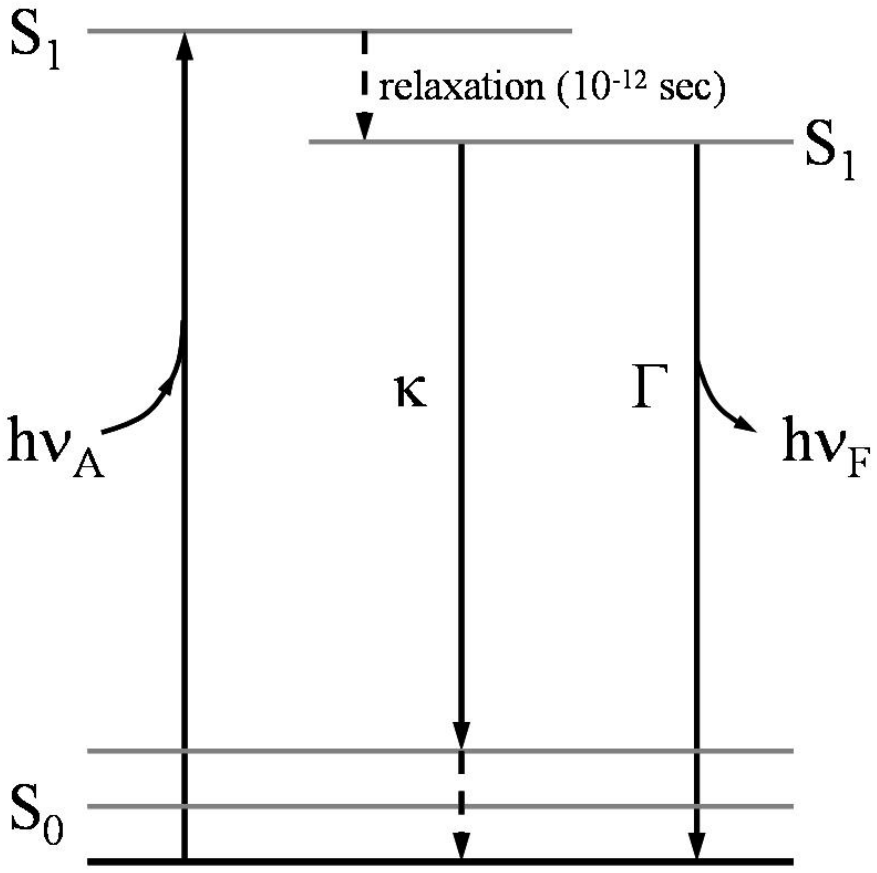

Figure 2.2. Modified Jablonski diagram illustrating the physical processes that occur after a molecule absorbs a photon. Adapted from Lakowicz[7] and Harris.[8]

Characteristics important to consider in optimizing imaging properties of NIR fluorescing dyes include the following:

[1] the fluorophore should possess an excitation/emission spectra with maxima in the near-infrared wavelengths (700 – 900-nm) to allow for minimal absorption by endogenous chromophores such as hemoglobin, lipids, and water;

[2] the fluorophore should possess a high quantum efficiency;

[3] the fluorophore should be chemically and optically stable; and,

[4] the conjugated fluorophore should exhibit suitable pharmacological properties including a high specificity for the desired target and little non-specific interactions.

An additional feature of fluorescence imaging that may impart contrast pertains to the fluorophore's lifetime. In general, in CW imaging techniques fluorescence emanating from a deeply embedded probe may be masked by background fluorescence from fluorophores located at or just beneath the surface. However, the use of time-resolved techniques permits the resolution of deeply embedded fluorophores from those residing near the surface. Typically, a lifetime on the order of nanoseconds permits the detection of deep tissue fluorescence using the time-resolved techniques discussed in the following section.[9] Furthermore, if the targeted fluorophore is conjugated such that it exhibits lifetime sensitivity to its immediate biochemical environment, the change in lifetime can be monitored using a time-resolved imaging technique and can provide additional

contrast enhancement. Over the last several years, NIR fluorophores with optimal photochemical properties have been developed.

2.2.1 Indocyanine Green and the CyDye™ Fluors

Of the NIR fluorophores currently in use as optical contrast agents, the indocyanine green is perhaps the most popular. Indocyanine green dye (ICG) remains the best candidate for enhancing optical contrast due to favorable excitation and emission at 805-nm and 835-nm [see Fig. 2.3(a)], respectively, which occur at wavelengths where blood and tissue are relatively transparent, its approval by the Food and Drug Administration (FDA) for systemic administration in humans, and its commercial availability. Clinical use of ICG was approved as early as 1956 (IC-Green™, Akorn, Inc., Buffalo Grove, IL). The dye has maintained a remarkably good safety profile since its introduction into clinics. ICG provides optimal imaging of choroidal circulation, making it an excellent adjunct to fluorescein angiography. ICG has also been used clinically for monitoring cardiac output and for assessing hepatic function.[10,11] Furthermore, ICG is highly bound to plasma protein as compared with fluorescein dye (98% vs. 45%) and, as a result, does not leak from vessels as readily.[12] Consequently, it is used primarily as a blood-pool agent for NIR imaging.

In addition to its nonspecificity, ICG undergoes a well-documented aggregation process in aqueous media, resulting in a wavelength shift of the main absorbance peak and a concurrent loss of absorption and fluorescence.[13] Therefore, there exists a need for a novel composition that improves the dye stability in solution, is simple to prepare, and most importantly, retains the high fluorescence yield *in vivo*. Rajagopalan *et al.* reported

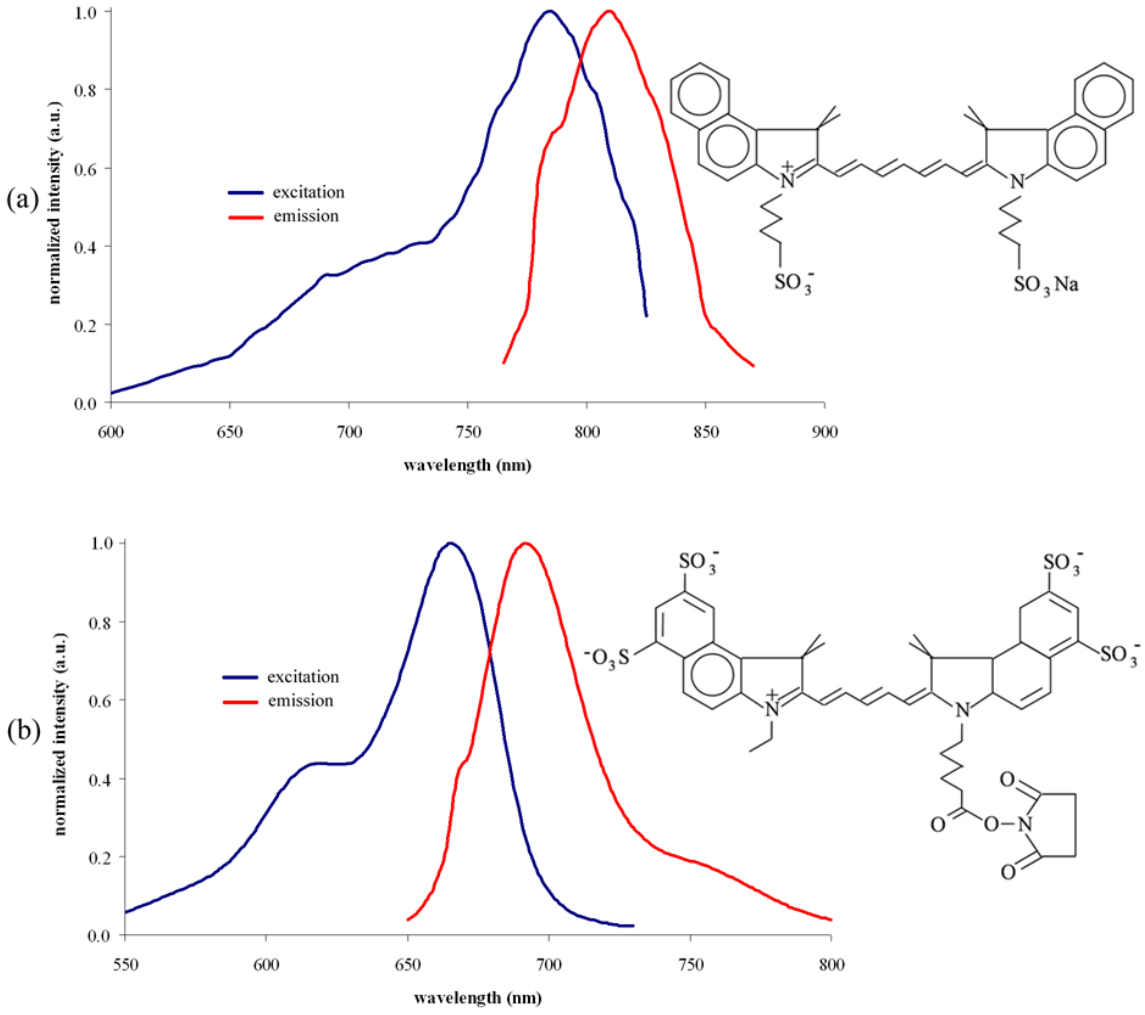

	ICG	Cy5.5
MW (kD)	730	1128
Extinction coefficient ($M^{-1}cm^{-1}$)	130 000	190 000
Quantum yield	0.016	0.23
Fluorescence lifetime (ns)	0.56	1.0

Figure 2.3. Chemical structures and excitation/emission spectra of (a) ICG and (b) Cy5.5. Emission spectra for ICG and Cy5.5 were obtained at 780-nm and 660-nm excitation, respectively. The table, compiled from data obtained from references 14-16, summarizes the some of the important properties of ICG and Cy5.5.

noncovalent interaction of an anionic polymer, sodium polyaspartate, with ICG produced an enhanced stability of the fluorescent dye in aqueous solution.[17] When left in aqueous solution and kept in clear bottles under normal laboratory lighting conditions, ICG loses most of its fluorescence due to aggregation. However, when mixed with polyaspartate ICG retains strong fluorescence even at day 24 under the same storage conditions.[17]

Others have attempted to devise analogues of ICG with improved physiochemical properties, and more importantly, to obtain NIR dyes with functional groups that can be readily used to label biomolecules such as peptides, proteins, drugs, and oligonucleotides.[18,19]

Close analogues of ICG are the CyDye™ fluors marketed by Amersham Biosciences (Piscataway, NJ). Although the excitation and fluorescence emission spectra of these dyes are blue shifted compared to ICG (emission maxima for Cy3, Cy5, and Cy5.5 occur at 575-nm, 675-nm, and 700-nm, respectively) [see Fig. 2.3(b)], the CyDye™ fluors are well suited for conjugation to antibodies and peptides for specific targeting of cancer.[15,20,21] The relatively broad wavelength range of fluorescence emission available, the relative ease with which they can be conjugated for specific targeting, and their commercial availability make CyDye™ fluors a popular choice for fluorescent labeling.[16]

2.2.2 Tumor Targeting Dye-Antibody Conjugates

To achieve receptor localization and specific imaging of cancer, fluorescent dyes have been attached to various ligands. The benefit to such specific targeting schemes is clear–

the high selectivity and affinity of receptor ligands result in a high signal to noise ratio while at the same time enabling the use of low (picomolar to nanomolar) concentrations of the compounds.[22] Most of the published fluorescent probe studies are targeted at cancers (at the tumor cells, themselves, or at molecular markers of the disease) in order to identify malignant lesions, for defining tumor spread to adjacent tissues, and as a guide for optimizing treatments of solid tumors.

Targeting fluorescent dyes for surface imaging was first attempted by the direct conjugation of cyanine dyes to monoclonal antibodies that are directed against certain tumor associated antigens.[21,23,24] Folli *et al.* showed specific tumor targeting first using an anti-carcinoembryonic antigen monoclonal antibody coupled with fluorescein (anti-CEA mAb–fluorescein)[23] and later using the monoclonal antibody E48 coupled to indopentamethinecyanin (mAb E48–indocyanin) to target squamous cell carcinomas in mice.[24] The studies reported tumor localization by both conjugates with tumor to normal tissue ratios of ten and eight for the case of the mAb–fluorescein conjugate and the mAb–indocyanin conjugate, respectively. Furthermore, the mAb–indocyanin conjugate resulted in a clearly detectable fluorescent signature due to its excitation and emission wavelengths at 640-nm and 667-nm, respectively, whereas the fluorescence from mAb E48–fluorescein was detected only after removal of the mouse skin due to fluorescein's emission at lower wavelengths (~500-nm).[24] These results further demonstrate that the efficiency of tumor immunophotodiagnosis can be improved by coupling to fluorochromes absorbing and emitting in the red or infrared wavelengths.

Ballou *et al*. prepared fluorophore conjugates of the cyanine dyes Cy3, Cy5, and Cy5.5 and two well-understood tumor-targeting antibodies, namely anti-SSEA-1 which localizes tumors expressing the SSEA-1 antigen and antibody 9.2.27 which is directed to a human melanoma antigen.[21] Compared to fluorescein, these dyes exhibit more favorable fluorescent signatures, emitting in the red wavelengths. In their studies, mice were tail-vein injected with 10-100 μg of the fluorophore-antibody conjugates and imaged using either a cooled CCD or intensified video camera. The resulting fluorescence images demonstrated that although Cy3-antibody conjugates targeted tumors, the Cy5 and Cy5.5 conjugates were more effective in visualizing the tumors, particularly in deeper tissue, again due to their fluorescence at longer wavelengths. The studies also showed that the conjugate-tumor interaction was so effective that fluorescence was still visualized from the tumor tissue 5 days after injection.

Additionally, it is well known that the epidermal growth factor receptor (EGFR) is overexpressed in many types of cancer. Soukos *et al.* reports the use of an anti–EGFR monoclonal antibody to target a diagnostic fluorescent dye, Cy5.5, and a photochemically active dye, $chlorin_{e6}$, for photodynamic therapy in the hamster cheek pouch carcinogenesis model.[25] Using a CCD camera and simple continuous wave fluorescence imaging, they observed specific targeting of the antibody-Cy5.5 conjugate and noted that the best contrast between normal and carcinogen–treated cheek pouches occurred between four and eight days after injection.[25] Using the antibody-$chlorin_{e6}$ construct, they were able to specifically target tumor cells and subsequently perform photodynamic therapy to reduce the size of the tumors. The results demonstrate the

potential for development of immunophotodiagnosis as both a diagnostic tool and a method of monitoring response to photodynamic therapy. Together, these works gave credence to and set the stage for the burgeoning field of molecular based optical imaging for disease diagnosis.

2.2.3 Tumor Targeting Dye-Peptide Conjugates

Although dye-antibody conjugates were a major breakthrough in the field of optical imaging, several unfavorable features were inherent in the approach. Large biomolecules, such as antibodies, would often elicit an adverse immunogenic reaction.[26] The long plasma half-life of the antibodies would also result in high background fluorescence as well as long blood clearance times.[26,27] Additionally, the biomolecules are often preferentially taken up by the liver.[28] Finally, for the detection of solid tumors that require the diffusion of contrast agents from the vasculature, the penetration of high molecular weight dye conjugates is unfavorable due to the net positive pressure within the tumor.[29] As a result, researchers have recently devised a viable alternative to the dye-antibody conjugate. In this paradigm, the fluorescent dye is attached to a small bioactive peptide that specifically targets overexpressed tumor receptors.

Making use of a simple continuous wave optical imaging system for *in vivo* fluorescence detection in a rat model, Achilefu *et al*. and Bugaj *et al*. studied peptide conjugates of the dye cypate, an ICG analogue.[27,28,30] They demonstrated that the cypate dye–octreotate peptide conjugates, designated cytate–1 and cytate–66, specifically target somatostatin receptor–rich tumors and specifically bind to the sst_2 receptors through the octreotate peptide.[27,28,30] Furthermore, they demonstrated that the cypate dye–bombesin

peptide conjugates, designated cybesin–1 and cybesin–66, selectively target bombesin receptor–rich tumors.[27,28,30] In a separate analysis, Becker *et al.* used an intensified CCD camera to perform *in vivo* imaging of mouse xenografts after injecting the cyanine dye–peptide conjugate, indotricarbocyanine–octreotate. The study yielded similar high tumor specificity for the dye–peptide conjugate, with a tumor fluorescence threefold higher than that of normal tissue up to 24 hours after injection.[22]

Methodologies employing protein–dye conjugates to target cell surface receptors have also been investigated. Becker *et al.* investigated the use of macromolecules as carriers of a fluorescent contrast agent for the optical imaging of human colon cancer xenografts in nude mice.[31] In their study, they compared two protein–dye conjugates; the first consisted of an indotricarbocyanine (ITCC) derivative covalently bound to transferrin (Tf–ITTC); the second, ITCC bound to human serum albumin (HSA–ITTC). They report that both compounds induced increased fluorescence contrast of tumors *in vivo* due to the accumulation of the macromolecules in the solid tumors as a result of enhanced vascular permeability and ineffective lymphatic drainage of tumor interstitium. However, the Tf–ITTC conjugate induced a higher fluorescence contrast, perhaps due in part to receptor-mediated internalization of the compound in tumor cells.[31]

Finally, in addition to small peptides and proteins, researchers have also investigated the use of small molecules as delivery vehicles for fluorescent dyes. Zaheer *et al.* report the use of a pamidronate–IRDye78 conjugate, termed Pam78, to specifically bind hydroxyapatite, the major mineral product of osteoblasts and calcifying vascular cells.[32] In their study, a CCD camera was used to acquire *in vivo* fluorescence images

following the intravenous injection of Pam78 in nude mice. In addition to demonstrating that the dye conjugate could be used to visualize most of the bony structures of the animal, they directly compared the fluorescence images with radioscintigraphy, the current gold standard for imaging hydroxyapatite. The fluorescence images provided high sensitivity, a higher resolution, and a shorter integration time (the radioscintigraphic image required a 30-min integration for 0.4-mCi of ^{99m}Tc radiocolloid injected compared to a 500-ms exposure for a NIR fluorescence image using 2.6-nmol of Pam78).[32] Their study further demonstrates the wide scope of applications possible with NIR fluorescence imaging.

2.2.4 Activatable Probes

Other methodologies for targeting fluorescent dyes to tumors have been proposed and investigated. Among them are schemes involving acid and enzyme cleavable conjugates of dye–biomolecules.[33,34] Weissleder *et al.* conjugated Cy5.5 onto a graft copolymer consisting of a poly-L-lysine backbone and methoxypolyethylene glycol side chains.[33] The dye molecules were conjugated in close proximity to each other in order to quench fluorescence. However, following intravenous injection into tumor-bearing nude mice, the fluorescent probe accumulated in the tumors due to its long circulation time and permeable neovasculature. An intratumoral fluorescent signal was generated by lysosomal proteases that cleaved the macromolecule and released previously quenched fluorophore. *In vivo* fluorescence imaging determined a 12-fold increase in fluorescent signal and allowed for the detection of submillimeter-sized tumors.[33]

Matrix metalloproteinase (MMP) activity is known to play a key role in many diseases including cancer. As a result, MMP inhibitors have been developed as anti-cancer drugs. In a recent study, Bremer *et al.* developed an activatable fluorescent probe for sensing MMP activity *in vivo* in tumor-bearing mice.[35] The MMP sensitive probe consisted of quenched NIR fluorophore (Cy5.5) conjugated to a MMP peptide substrate and a graft copolymer of methoxy-polyethylene-glycol-derivatized poly-L-lysine. The probe would fluoresce when MMP enzymes cleaved the peptide substrate and released previously quenched fluorophore. The fluorescent probe was injected into mice exhibiting the HT1080 human fibrosarcoma tumor model due to its high MMP production. Subsequent *in vivo* imaging resulted in a significantly higher fluorescence signal from HT1080-bearing mice compared with control mice with tumors devoid of MMP activity.[35] Furthermore, Bremer *et al.* demonstrated that the fluorescent probe could be used to image MMP inhibition *in vivo*.[35] Mice with HT1080 tumors were treated with prinomastat, a potent MMP inhibitor, for two days and subsequently imaged. The images revealed that there was significantly less MMP fluorescent signal in treated tumors compared to untreated tumors.[35]

As alluded to earlier, activatable probes that do not fully quench could be best imaged with time-dependent methods of NIR imaging. Again, this is because background fluorescence from unquenched fluorophore can often mask the fluorescence signal from underlying, deeply embedded fluorophore. Additionally, specificity of imaging could be enhanced if temporal fluorescence decay parameters were tomographically reconstructed.

2.3 Measurement Approaches

There are three distinct methods for monitoring the propagation of NIR light and the emission of generated fluorescence light in response. These methods are continuous wave (CW), time-domain photon migration (TDPM), and frequency-domain photon migration (FDPM).

2.3.1 Continuous-Wave Imaging

The earliest and simplest methods of measuring NIR light interaction with tissue involve intensity-based or CW techniques. CW techniques generally involve measuring the spatial distribution of light intensity at the tissue surface resulting from illumination by a source of constant intensity. CW techniques may be used to measure NIR fluorescence from exogenous contrast agents with a point or area light source at the excitation wavelength incident on the tissue surface. The collection of the fluorescence re-emitted from the tissue surface occurs through a point or area detector that discriminates the re-emitted fluorescence from the excitation light. Because the excitation light fluence [which represents the amount of light in terms of its local concentration (photons/volume) times the speed of light (length/time), or alternatively in terms of a flux (photons/area/time)] exponentially attenuates as it travels from the tissue surface, the excitation fluence always remains greatest at the tissue surface. Furthermore, the amount of generated fluorescence at any given position within the tissue is proportional to the product of the local fluorophore concentration and the local excitation fluence. As a result, a low concentration of fluorophore at or near the tissue surface can produce the bulk of the detected signal emitted and collected in CW techniques. A consequence of

CW methods is that the signal from a deeper embedded target containing a high concentration of fluorophore may be easily masked by a very low concentration of fluorophore at or near the tissue surface. As discussed below, methods that measure the time-dependence of light propagation may escape this limitation.

2.3.2 Time-Domain Imaging

In addition to measuring the spatial distribution of light intensity, time-dependent measurement approaches are also capable of measuring the temporal distribution of the detected light. Time-resolved techniques employ an excitation light source whose intensity varies with time. Time-domain photon migration (TDPM) techniques make use of ultra-short (femtosecond-picosecond) light pulses and detectors which are either fast, time-gated, or single-photon counting devices. A light pulse is delivered to the tissue, which, as a result of multiple scattering, broadens with nanosecond "time-of-flight" and attenuates as it propagates through the tissue [see Figure 2.4(a)]. In the presence of an NIR excitable fluorophore, a fluorescence pulse is generated within the tissue that is increasingly broadened and attenuated owing to the fluorescence decay kinetics of the fluorophore. Because the region of highest excitation light fluence is not constant and propagates away from the tissue surface with time, the spatial location of the generated fluorescent pulse also varies resulting in the deeper origin of fluorescent signals re-emitted at the tissue surface. As a result, as long as the lifetime or the average time for relaxation of the fluorophore is less than or comparable to the "time-of-flight" associated with light propagation, the detected fluorescence may, as a function of time,

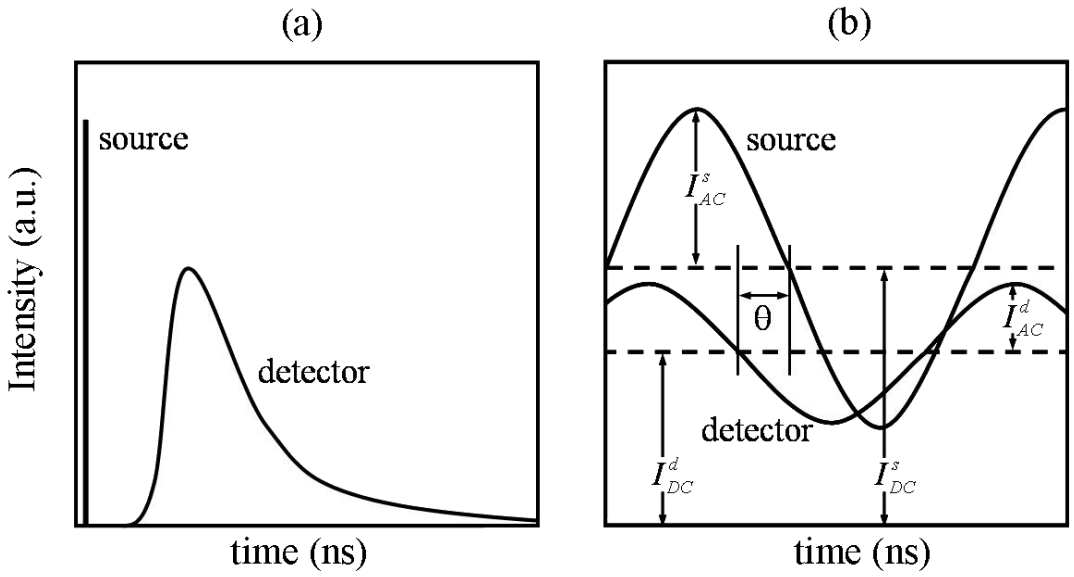

Figure 2.4. Schematic representation of the time-dependent propagation of light in the (a) time-domain and (b) the frequency domain.

originate from various depths within the tissue in time-dependent measurement methods.[9]

2.3.3 Frequency-Domain Imaging

An alternative time-dependent measurement methodology, which is directly related to TDPM through the Fourier transform, is known as frequency-domain photon migration (FDPM). In this approach, a light source that is sinusoidally intensity-modulated at radio frequencies is used to launch photons into the tissue. Typically, modulation frequencies range from 30-200 MHz. As the intensity-modulated light (also referred to as a "photon density wave") propagates through the tissue, its amplitude is attenuated and it experiences a phase-lag relative to the incident light. In the presence of a NIR fluorophore, the intensity-modulated excitation fluence results in a fluorescent "photon

density wave" or intensity-modulated emission fluence which is further amplitude attenuated and phase-delayed owing to the fluorescent decay kinetics of the dye in its current environment.[7] The phase-lag, θ, and amplitude, I_{AC}, of the detected fluorescent photon density wave, measured relative to the incident light wave using a fast detector or array of detectors, are pronounced owing to the fluorophore's decay kinetics [see Figure 2.4(b)]. As a result, fluorescence-enhanced FDPM may be used to exploit the fluorescent relaxation process in order to improve contrast in the phase-lag and amplitude attenuation of the detected signal.

Similar to TDPM, the excitation light fluence in FDPM also varies in time and space, and the region of highest excitation fluence is not consistently located at the tissue surface. Consequently, as long as the product of the fluorophore lifetime and modulation frequency is less than one, the detected fluorescence may originate from deep within the tissue - even in the presence of background dye.[36] Another important feature of FDPM measurements concerns their inherent insensitivity to ambient light. Because the amplitude of the detected fluorescent signal is unaffected by non-modulated ambient light, FDPM enables greater sensitivity and depth of penetration than conventional CW techniques.[6,37]

In practice, FDPM consists of launching an intensity–modulated plane wave or spherical wave of near-infrared (NIR) light into a tissue of interest. Since NIR light (700-900 nm wavelengths) can penetrate several centimeters of tissue without the harmful radiation effects of gamma rays, x-rays, or ultraviolet light, it is especially

useful for biomedical imaging and can be used to image as deep as possibly five centimeters from the tissue surface.[37]

The NIR excitation wave propagates through the tissue and when it encounters a fluorescent agent, it interacts with the fluorophore generating a red–shifted emission wave. As the excitation and emission waves transit through tissue, they experience an attenuation in amplitude as well as a phase–lag or phase delay relative to the incident light. The magnitude of the attenuation and the phase delay of the propagating waves depends upon the spatial map of local tissue optical properties, denoted by the tissue absorption coefficient, $\mu_{a\,x,m}$, and the isotropic scattering coefficient, $\mu'_{s\,x,m}$, at both excitation and emission wavelengths (subscripts *x* and *m*, respectively). The wave generated by the radiative relaxation of the fluorophore is dependent upon the fluorophore's local concentration (represented by the absorption coefficient owing to the fluorophore, $\mu_{a_{xf}}$) as well as the local biochemical environment. Specifically, the local biochemical environment of the fluorescent dye impacts the kinetics of relaxation which can be described by the mean lifetime of the excited singlet state, τ, as well as its quantum efficiency, ϕ, or the proportion of the excited singlet states that relax radiatively to release emission light (recall Figure 2.2). Hence, the emission wave detected at the tissue boundary is impacted by the integrated effects of varying optical properties, ($\mu_{a\,x,m}$, $\mu'_{s\,x,m}$) as well as by the properties owing to the fluorophore and its kinetics ($\mu_{a_{xf}}$, τ, ϕ).

Using the measurements of amplitude demodulation and phase-shift characteristic of the generated fluorescence photon density wave, fluorescence FDPM imaging seeks to recover three–dimensional spatial maps of fluorescent properties in order to accomplish diagnostic imaging.[38-41] Such three–dimensional maps are obtained using a reconstruction algorithm to essentially iteratively solve an inverse boundary–value problem. Because of the multiply scattering nature of tissue, the solution of the inverse problem is the only way to extract the size, exact location, and metabolic status of the disease, especially if the target is located relatively deep below the tissue surface.[38-41] Hence, the solution of such an ill–posed inverse problem is itself a topic of ongoing research.

Tomographic optical imaging using fluorescence requires special contrast agents that exhibit either molecular specificity, lifetime sensitivity, or are activated upon association with the targeted disease. Furthermore, the clinical translation of fluorescence-enhanced optical imaging for deep tissue imaging will only occur once tomography is coupled with specific fluorescence contrast agents. Unfortunately, to date there exists not a single targeted fluorescence contrast agent approved by the FDA for routine diagnostic imaging. Therefore, there remains an opportunity for the design and development of specific fluorescent contrast agents for diagnostic optical imaging. Small animal imaging provides a convenient platform to test the development of novel fluorescence contrast agents and their biological activity *in vivo* in model systems of disease. Additionally, testing novel fluorescence contrast agents in small animals *in vivo* provides the added advantage that, due to the animals' relatively small volume,

tomographic reconstruction is unnecessary; as evidenced bythe *in vivo* fluorescence images of mammary disease in a canine subject (Section 5) and the studies conducted on small animals (Sections 6-8), for malignancies located relatively shallow beneath the tissue surface, fluorescence images can provide two–dimensional information about the relative location of the malignancy without requiring the solution to the inverse problem. Before describing the experimental work, the following section details the instrumentation employed in making measurements of FDPM and the imaging system employed in the animal *in vivo* fluorescence imaging studies.

3. INSTRUMENTATION

The bulk of the experimental data presented in this dissertation was obtained using an intensified charge-coupled device (ICCD) imaging system developed at the Photon Migration Laboratories. Therefore, it is appropriate to prelude the discussion of experimental results with a section devoted to a detailed description of the instrumentation used for the acquisition of the data presented in the following sections. In addition to detailing the imaging system, this section describes inherent shortcomings of *in vivo* fluorescence imaging and several experimental measures devised to minimize their effects.

3.1 Image Intensification

Extreme low light level conditions exist during fluorescence imaging at clinically relevant frame rates, i.e. sub-second exposure times. Such low-exposure imaging techniques require that the optical image be amplified with low noise in order to produce a final image with a good signal-to-noise ratio.

One such way to accomplish this amplification is via the use of image tube intensifiers. Initially developed for night vision military applications, image intensifiers are now finding widespread applications in scientific arenas.[42,43] Image intensifier tubes consist of three key components: the photocathode, the microchannel plate (MCP), and the phosphor screen. The basic components of an intensifier tube are shown schematically in Figure 3.1.

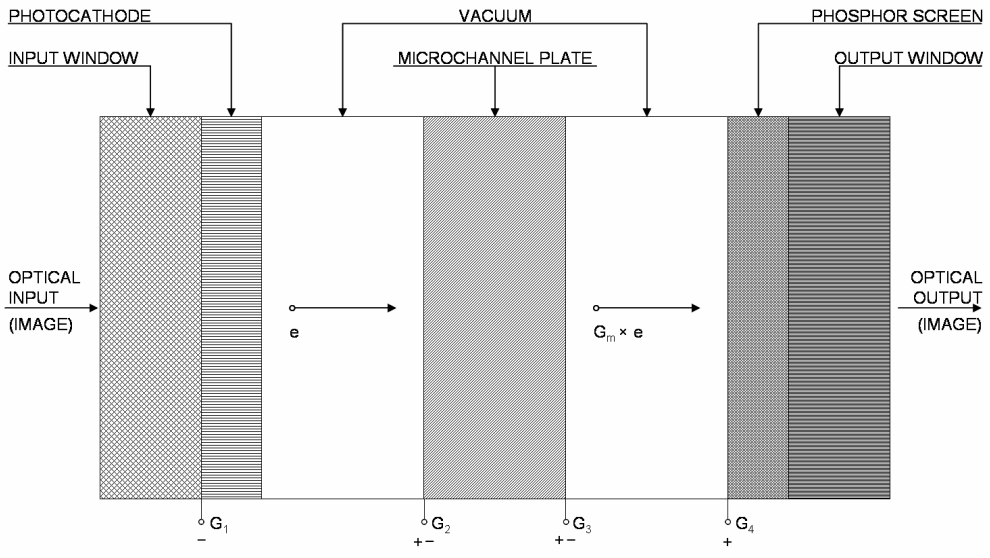

Figure 3.1. Schematic depiction of an image tube intensifier illustrating the three key components: the photocathode, microchannel plate, and the phosphor screen. Reproduced from Johnson and Owen.[43]

The photocathode converts the incident optical image (photons) into an electronic image (photoelectrons). A high voltage power supply (Fig. 3.2) maintains the photocathode at a negative bias (-200 – -65V) to provide a sufficient source of electrons. The photocathode response to incident light is an important factor that directly impacts the intensifiers quantum efficiency or photoresponse. The spectral quantum efficiency of the photocathode, defined as the average number of photoelectrons produced per input photon, is a measure of photocathode response.[43] Alternatively, the photoresponse may be expressed as radiant sensitivity, a ratio of photocathode current per watt of incident illumination, as a function of wavelength.[43] For the image tube intensifier employed in the studies presented in the following sections (model FS9910C, ITT Nightvision, Roanoke, VA), Figure 3.3 presents typical curves of the spectral quantum efficiency and

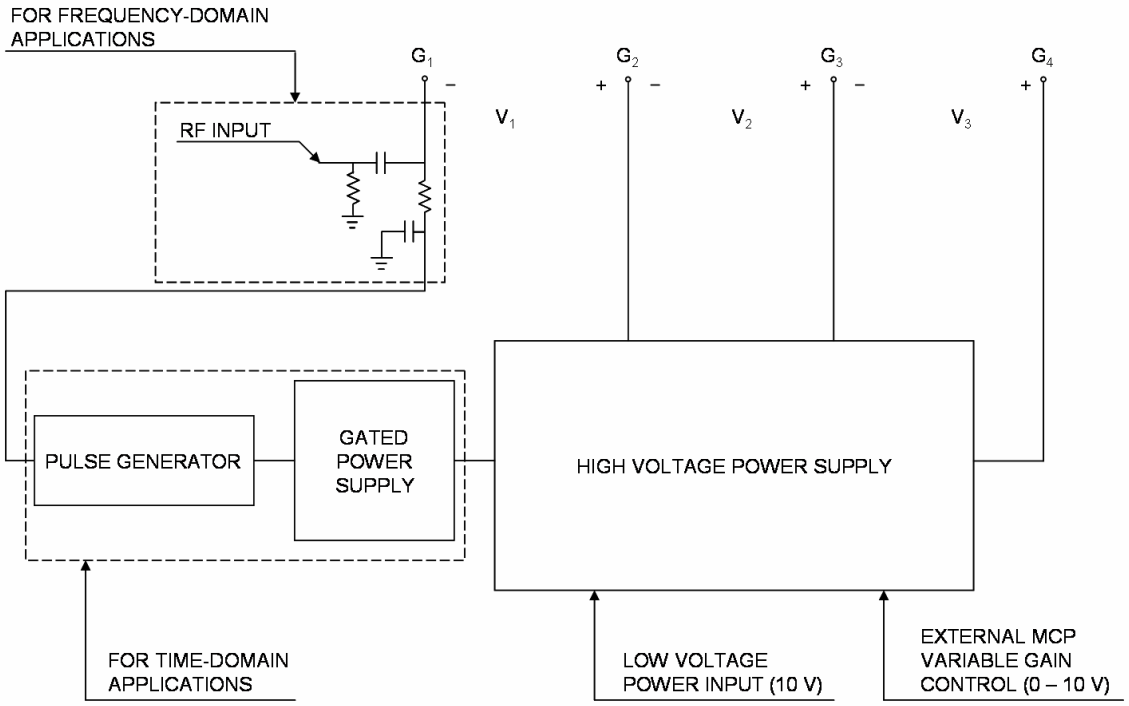

Figure 3.2. High voltage power supply used to provide the necessary voltage biases to operate the image intensifier. The electrodes G_1 G_2 G_3, and G_4 are maintained such that the voltage potential between the electrodes are $V_1 = -200\text{V}$ or -65V, depending on CW or frequency-domain operation, respectively, $V_2 = 0 - 1000\text{V}$, variable voltage to control the gain, and $V_3 = 4000\text{V}$. Additional instrumentation and circuitry allows either time-domain or frequency-domain operation. Adapted from Johnson and Owen.[43]

radiant sensitivity. Therefore, in order to optimize detector sensitivity, it is critical that the photocathode possesses a high photoresponse in the wavelength range of interest.

After the incident photons are converted into photoelectrons by the photocathode, the photoelectrons are amplified by the microchannel plate. The MCP consists of a network of closely packed hexagonal arrays of channel electron multipliers.[42,43] As the photoelectrons pass through the channels and strike the channel walls, more electrons are

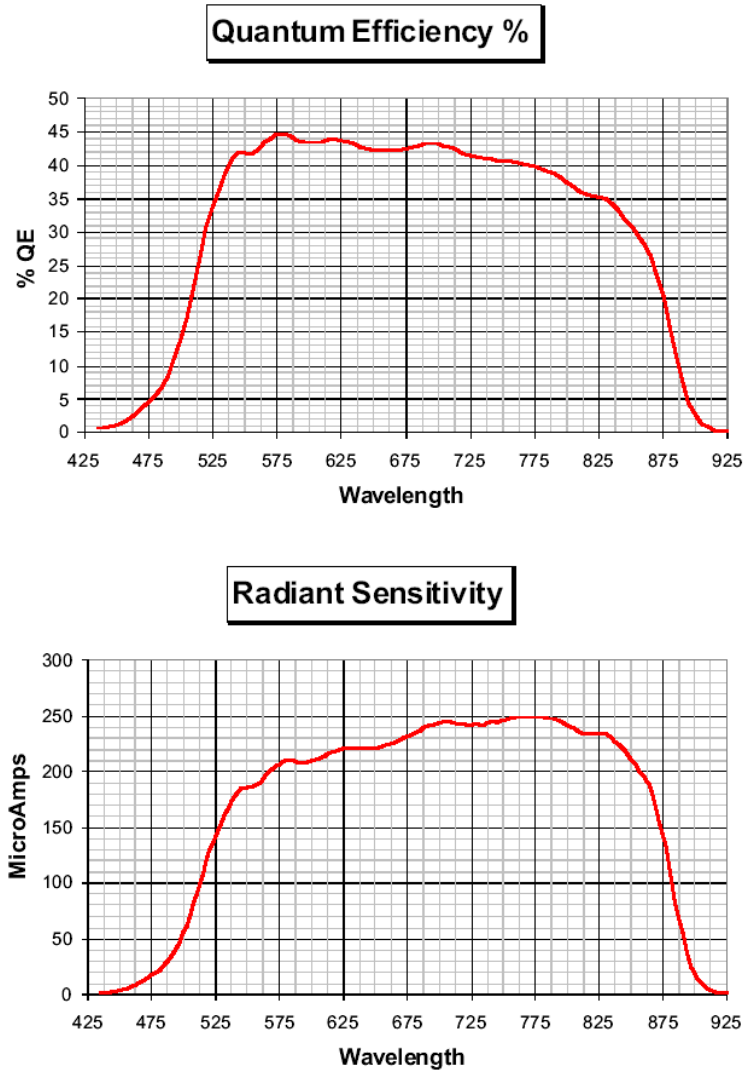

Figure 3.3. Typical spectral response curves of the image tube intensifier employed in the studies presented within this dissertation.[44]

produced. Each channel operates independently to amplify and preserve the spatial orientation of the electronic image. The MCP is biased positively relative to the photocathode, permitting the flow of photoelectrons into the MCP.[43] The degree of amplification is a function of the voltage differential applied across the input and output

electrodes of the MCP (0 – 1000V). Image intensifier tubes capable of providing electron gains of 10^7 (e^- output/ e^- input) are not uncommon.[43] The spacing between the channel amplifiers determines the limiting resolution of the image intensifier tube. For the intensifier employed in the following studies, a spacing of 6-μm between channel centers leads to a resolution of >64 line-pairs/mm.[45]

Having been amplified by the MCP, the spatially-preserved electronic image is converted back into an optical image at the phosphor screen.[43] An electrode on the MCP-side of the phosphor screen is used to accelerate the MCP output photoelectrons to high energy (~ 4000V), improving the photoconversion that occurs when the photoelectrons strike the phosphor screen. The decay time, or persistence of the phosphor, depends on the phosphor type employed in the screen and plays an important role in the frequency-domain operation discussed in Section 3.3. The intensifier employed in the studies presented herein incorporates a P-43 phosphor screen whose peak emission occurs at 550-nm and whose decay time to 1% is 3-msec.[42,44]

3.2 Image Acquisition

The amplified optical image produced at the phosphor screen of the image intensifier must be captured, digitized, and stored for further data processing and analysis. A convenient method to capture the amplified phosphor image requires the use of a charge-coupled device (CCD) camera. CCD cameras come in a variety of designs and grades and may be tailored to their particular application, from astronomy to microscopy to medical imaging. However, common among all the cameras is the use of a light sensitive silicon chip, the CCD itself, as the photodetector. The most critical feature of

the CCD is its quantum efficiency, or the ability to produce electronic charge from incident photons. For intensified charge-coupled device (ICCD) systems, it is desirable that the CCD exhibits high quantum efficiency at the peak wavelength of the phosphor emission of the image tube intensifier. For the ICCD system employed in the acquisition of experimental data presented in the following sections, the quantum efficiency of the SITe scientific-grade SI-003A full-frame CCD (Scientific Imaging Technologies, Inc., Beaverton, OR) complements the 550-nm peak phosphor emission of the image tube intensifier (see Fig. 3.4). Other features of CCD cameras, discussed in the following sections, afford a great deal of flexibility that may be exploited to tailor an imaging system to a particular application.

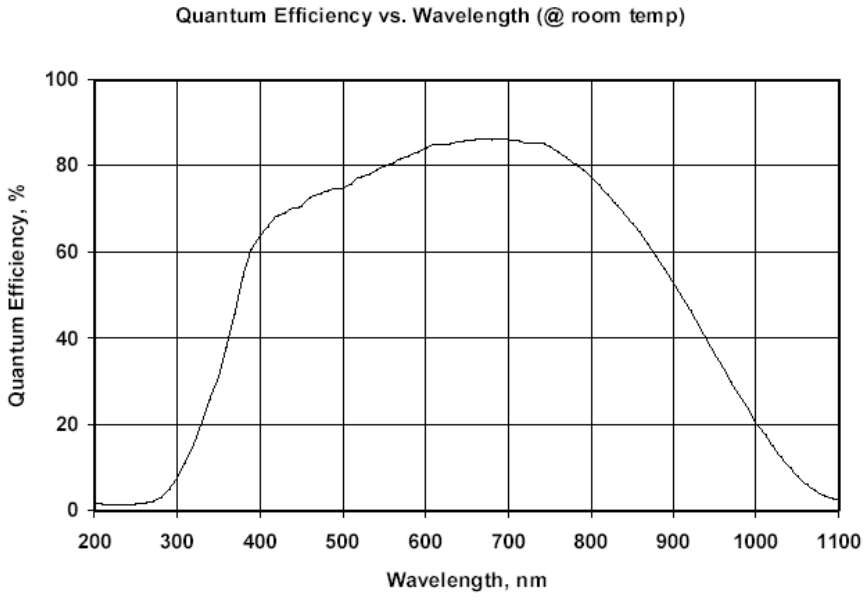

Figure 3.4. Spectral quantum efficiency of SITe scientific-grade SI-003A full-frame CCD used in the experiments presented in the following sections.[46]

3.2.1 Lens-Coupled vs. Fiber-Optic-Coupled ICCDs

In a lens-coupled ICCD assembly the image produced on the phosphor screen of the intensifier is coupled, as the name implies, by a lens into the optical input of a conventional CCD. This type of design, shown schematically in Figure 3.5, offers flexibility because the intensifier is not a permanent fixture of the ICCD and its removal permits the operation of the system as a traditional CCD detection system.[47] Furthermore, in this type of setup, replacing the intensifier is simple and straightforward. Alternatively, in a fiber-optic-coupled ICCD assembly, the output of the image intensifier is coupled directly to the CCD via a fiber-optic bundle or taper. The taper is larger in area at the intensifier end and smaller at the end bound onto the CCD. Thus, the fiber-optic taper is commonly referred to as a reducing taper. To achieve a smooth

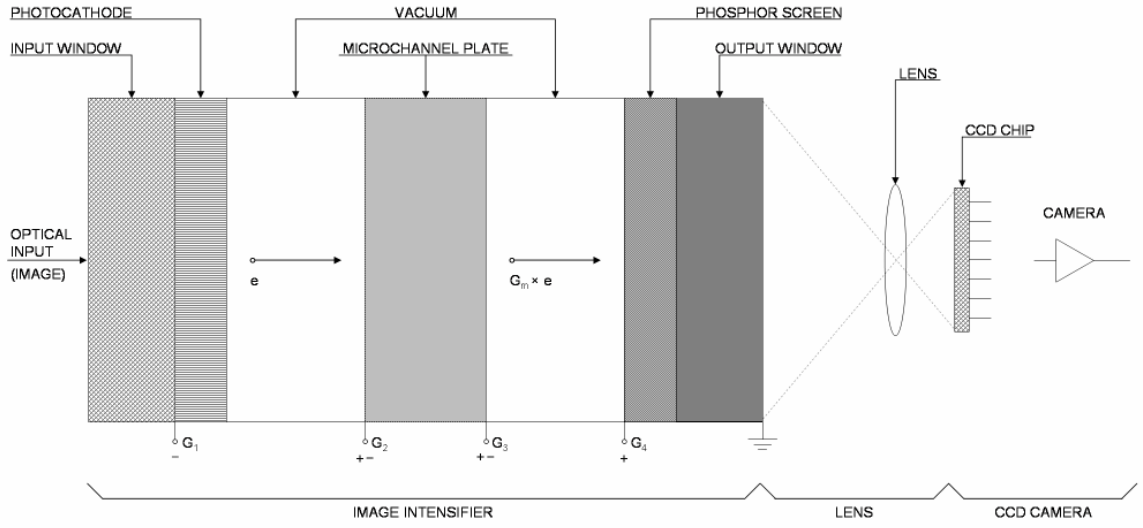

Figure 3.5. Schematic design of a lens-coupled ICCD assembly. Reproduced from Johnson and Owen.[43]

transition between the intensifier's phosphor screen and the fiber-optic taper and maintain high resolution, an index of refraction-matching gel is applied at the interface and the gap is kept as short as possible.[43] In this design, the coupling between the intensifier and the CCD is usually permanent, as de-coupling the assembly often results in the fiber-optic taper delaminating the CCD chip. The fiber-optic coupled assembly has a higher light-transfer efficiency than does the lens-coupled system, but its image distortion and resolution performance is inferior to the lens-coupled design.[43] Also the chance for possible adverse RF interference at the sensitive CCD by the intensifier's high voltage power supply is greater than for the lens-coupled assembly. A schematic of the fiber-optically coupled ICCD is provided in Figure 3.6.

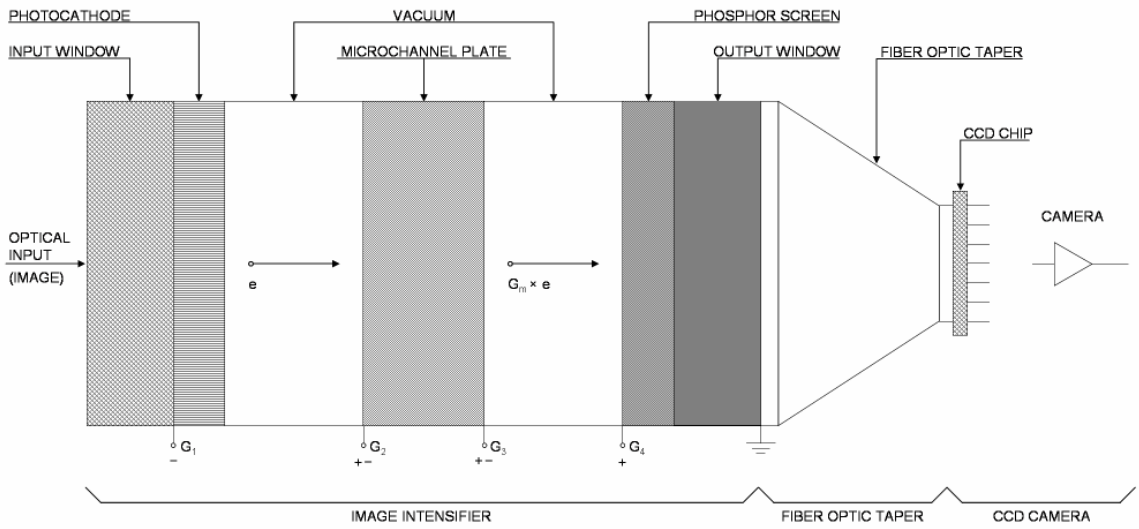

Figure 3.6. Schematic design of a fiber-optically coupled ICCD assembly. Reproduced from Johnson and Owen.[43]

3.2.2 Full-Frame vs. Frame-Transfer CCDs

Upon striking the CCD chip, photons produce electrons via the photoelectric effect. The number of electrons produced, or more correctly, the magnitude of the created charge, is proportional to the intensity of the detected light signal. The way the CCD transfers and reads this signal charge is referred to as the architecture. There are primarily two distinct CCD architectures: full-frame and frame-transfer.

Full-frame CCDs are perhaps the simplest in architecture. In the classical full-frame CCD format, the total area of the CCD is available for photodetection. The CCD design employs a single vertical or parallel register for sensing incoming photons during the exposure period. The parallel register is a large array of pixels for photon exposure, charge integration, and charge transport. At the completion of the exposure, the accumulated charge in the parallel register is ready to be read out and converted into a digital signal. First, rows of pixels are shifted vertically toward the readout or serial

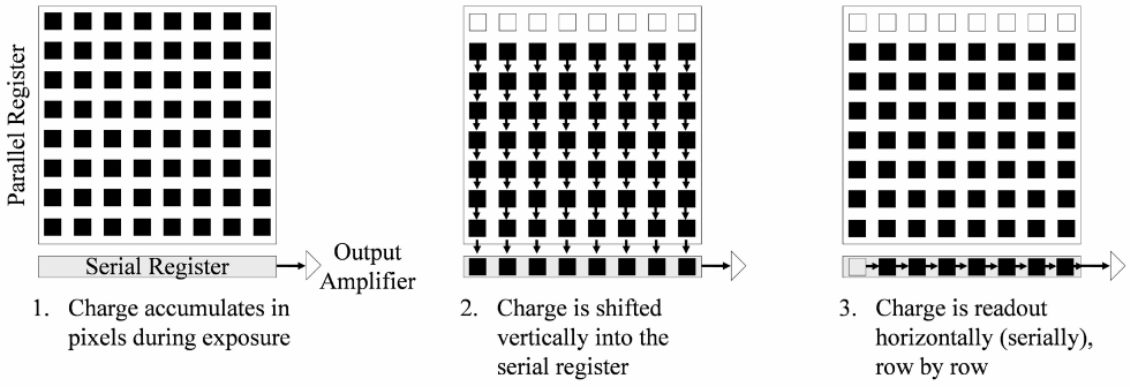

Figure 3.7. Schematic depicting the full-frame CCD architecture.[48]

register. Once in the serial register, the charge is further shifted in the horizontal direction out of the serial register and into the A/D converter where the analog data is converted into a digital signal (Fig. 3.7).[46,48] This process of parallel and serial shifts occurs until all the charge is read out, row by row, to form an image. A mechanical shutter must be used to control the exposure and prevent light from striking the CCD during the read process. Otherwise, a phenomenon known as charge smearing would occur resulting in blurred and distorted images.[48]

Unlike a full-frame CCD, a frame-transfer CCD has its parallel register divided into two distinct areas: the image array, where images are focused, and the storage array,

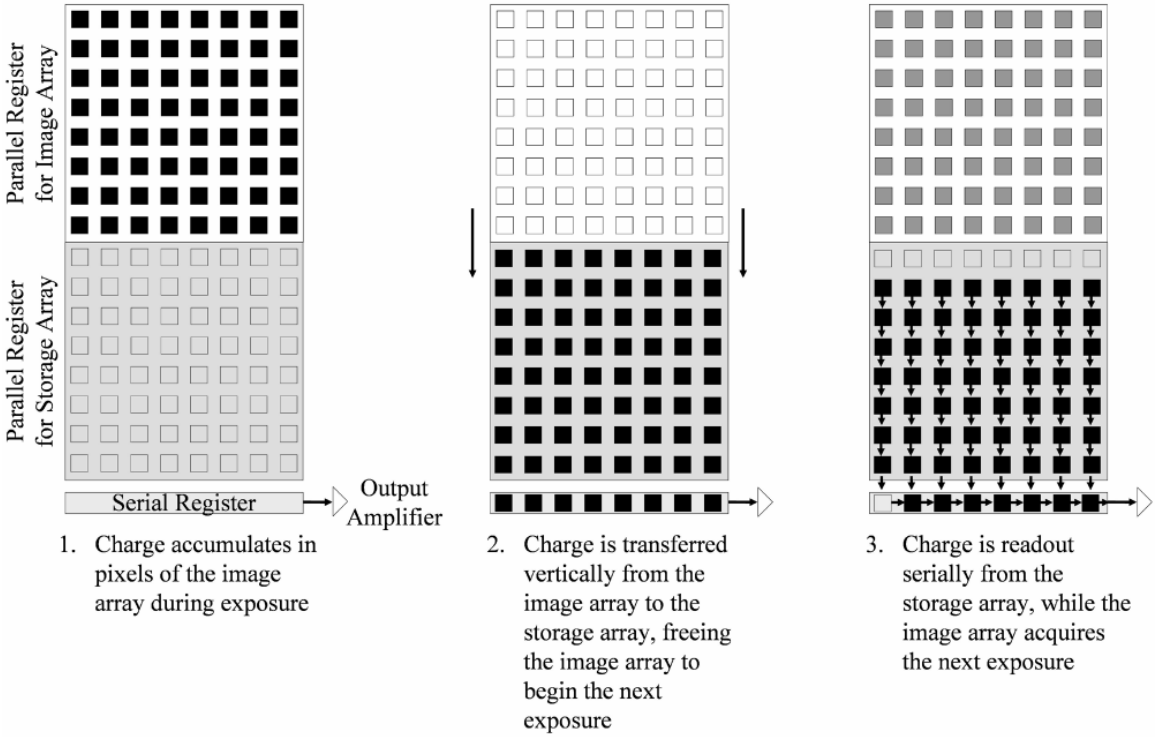

Figure 3.8. Schematic depicting the frame-transfer CCD architecture.

where the integrated image is temporarily stored prior to readout (Fig. 3.8). As a result, only one-half of the CCD pixels are utilized for photodetection. Typically, the image and storage arrays are identical in size but the storage array is covered with an additional opaque mask to shield the underlying pixels from light. After the image array is exposed to light, the accumulated charge is rapidly shifted to the storage array. This very rapid shift-under-the-mask operation is typically performed in less than 300 microseconds and allows the frame-transfer CCD to operate continuously without a mechanical shutter and with no observed charge smearing.[48] The readout of the charge from the storage array then proceeds via a series of parallel and serial shifts, similar to readout in a full-frame CCD. However, unlike the full-frame CCD that must wait for all charge to be readout prior to beginning the next exposure, the image array begins to integrate charge for the next image while the masked storage array is being read. The storage array is typically readout in full in less than 100-msec.[49] As discussed in the following section, this multitasking feature of the frame-transfer CCD drastically improves the frame rate.

3.2.3 Frame Rate

The frame rate or the speed at which a CCD camera acquires and reads out an image is an important criterion in imaging studies. It is equivalent to the inverse of the time needed for the CCD to acquire and readout an image, or the sum of the frame acquisition time and the frame read time and is typically expressed in frames per second (fps). In most cases, the frame acquisition time can be approximated as the image exposure time while the frame read time can be estimated as the product of the number of pixels to be

digitized and the serial conversion time or the time required to digitize a single pixel.[50] Thus, the frame rate may be expressed as:

$$\text{frame rate} = \frac{1}{\text{exposure time} + \dfrac{\#\text{ of pixels}}{\text{digitizer rate}}}. \tag{3.1}$$

As an example, for the SITe 1024×1024 pixel scientific-grade SI-003A full-frame CCD (the CCD employed in the experimental studies) operating with a readout rate and integration time of 200-KHz and 800-msec respectively, the frame rate is approximately 0.17 fps.[46] For a frame-transfer CCD having a typical readout rate of 5-MHz,[49] an image of the same size may be acquired at a rate of 1.4 fps, or approximately 8 times the rate of the full-frame CCD. As can be seen from the example, frame-transfer CCD cameras can vastly improve the frame rate. The increase in the frame rate is even greater when the number of pixels to be digitized is increased. Unfortunately the increase in frame rate of the frame-transfer CCD often comes at the expense of dynamic range or signal-to-noise ratio.[50]

3.2.4 Dynamic Range

Dynamic range refers to the ability to quantitatively detect very dim and very bright parts of a single image. The dynamic range of a CCD sensor is independent of the application and will indicate the bit-depth of the analog-to-digital (A/D) conversion that might be appropriate for the given system. Dynamic range may be defined mathematically as:

$$\text{dynamic range} = \frac{\text{linear full well}}{\text{read noise}} \tag{3.2}$$

where linear full well, a specific measure of pixel well capacity, and read noise, the noise associated with a single readout event, are expressed in number of electrons.[50]

As a specific example, consider again the SITe 1024×1024 pixel scientific-grade SI-003A CCD, which has a full well capacity of 330,000 electrons.[46] At a typical readout rate of 200-KHz, the read noise is 12 electrons.[51] The dynamic range of this chip is therefore 330,000:12 or 27,500. In order to take full advantage of this dynamic range, the camera that incorporates the SITe SI-003A CCD utilizes a 16-bit A/D converter (2^{16} or 65,536 clean shades of gray). Digitization at lower than a 16-bit depth would sample the signal at a level below the limit imposed by the noise. The dynamic range is often further optimized by thermoelectrically cooling the camera unit. A lower temperature results in a lower read noise and thus, yields the largest dynamic range possible. For comparison, an uncooled video camera has a much higher read noise, and the resulting dynamic range is usually 8 bits or lower.[43]

The degree of accuracy required by the system will affect the speed and cost. In general, a lower read noise and a larger full well capacity yields a higher dynamic range. Furthermore, because lower read noise is obtained at slower readout rates, these combined effects contributing to a higher dynamic range favor a full-frame CCD architecture. Finally, camera cost generally increases with increasing dynamic range. As a result, dynamic range requirements should be considered very carefully when selecting a CCD camera.

3.2.5 Signal-to-Noise Ratio

Signal-to-noise ratio or SNR describes the quality of a measurement. In CCD imaging, SNR is computed on a per-pixel basis and refers to the relative magnitude of the signal compared to the uncertainty in that signal. Specifically, it is the ratio of the measured signal to the overall measured noise among repeated exposures at a particular pixel. [50] Because light and electrical charge are quantized, the number of photons or electrons that pass a point during a period of time are subject to statistical fluctuations. In a CCD, because the electrons comprise the signal, they also contain the inherent natural variation of the incident photon flux at a given point. Additionally, inherent CCD noise sources create electrons that are indistinguishable from the electrons comprising the actual signal. As a result, all noise sources need to be considered when calculating overall SNR.

The inherent time-dependent variations in the photon flux incident on the CCD create a fluctuation in the signal that is known as photon or shot noise. Photons collected by the CCD follow a Poisson distribution.[50] Thus, the shot noise, or the standard deviation of the signal, may be expressed as the square root of the mean signal,

$$\text{shot noise} = \sqrt{\text{signal}} = \sqrt{I \times QE \times t}\,, \tag{3.3}$$

where I is the photon flux expressed in units of photons/pixel/second, QE is the quantum efficiency of the CCD, and t is the integration time in seconds.

Among CCD noise sources is the readout noise created by both the CCD sensor and the electronics themselves. Readout noise introduces a degree of uncertainty in the measurement and diminishes the overall SNR. The charge output at a particular pixel in a CCD sensor may vary given identical charge accumulation in the well. Readout noise

refers to the uncertainty introduced during the process of quantifying the electric charge in the pixel wells.[52] Typically, the readout noise is dominated by noise that arises from signal amplification, although noise introduced by the A/D conversion can also be significant.[50]

The final source of CCD noise is known as dark noise. Dark noise refers to the generation of electronic charge in a CCD pixel well in the absence of light. Because electrons can be thermally generated in the pixel wells, dark noise is a strong function of temperature. Dark noise, which also follows a statistical Poisson distribution, may be expressed as the square root of the number of thermally generated electrons or dark count within a given exposure.[50] Although the dark count may be subtracted from an image during processing, the dark noise cannot.[50] To reduce the dark noise many CCDs are thermoelectrically cooled. Cooling the CCD from room temperature to -25°C can reduce the dark noise by more than 100 fold.[50]

Considering all the sources of noise, the overall SNR for a CCD camera at a particular pixel can be calculated from the following expression:

$$SNR = \frac{I \times QE \times t}{\sqrt{\left(I \times QE \times t\right) + \left(N_d \times t\right) + N_r^2}}, \tag{3.4}$$

where the quantities I, QE, and t, were previously defined, N_d is the dark count expressed in units of electrons/pixel/second, and N_r is the read noise in electrons.

In low-light-level imaging conditions the low signal level will yield poor SNR values. Also, in these conditions the read noise typically exceeds shot noise and the image data is said to be read-noise limited. To improve the SNR, the integration time

may be increased. Although the dark count and hence dark noise also increase with increasing integration time, the net effect of increasing the integration time is an increase in the SNR. The integration time can be increased until shot noise exceeds both read noise and dark noise. At this point, the image data is said to be shot-noise limited. In terms of SNR, the shot-noise limit represents the optimum in camera performance.

An additional way to increase the SNR is to employ a technique known as pixel binning. Binning refers to the process of combining charge from adjacent pixels in a CCD during readout. Binning of 1×1 implies that the pixel charge is readout from the individual pixels as is. In two-fold or 2×2 binning, the charge from four adjacent pixels (two pixels in each the parallel and serial directions) of the CCD array are combined to yield a single 'superpixel' that contains four times the charge of the original pixels. In addition to increasing the SNR, pixel binning has the added benefit of increasing the frame rate. For example, two-fold binning approximately quadruples the frame rate.

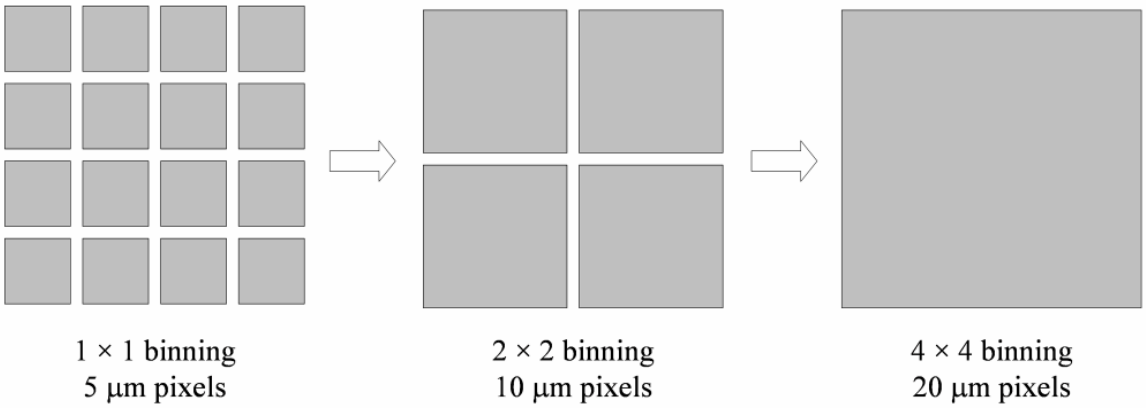

Figure 3.9. Schematic depicting the process of pixel binning. Pixel binning improves SNR and readout rate but results in diminished spatial resolution.

Finally, although the shot-noise limit may be reached more quickly by binning neighboring pixels, it comes at the expense of spatial resolution. Because spatial resolution is proportional to pixel size, an additional consequence of pixel binning is diminished spatial resolution: 2×2 binning reduces the spatial resolution by half, 4×4 binning reduces the resolution by a factor of four, etc. Figure 3.9 graphically illustrates the effect of pixel binning.

3.3 Instrument Specifications

Sinusoidal intensity–modulated excitation light is provided by a laser diode (660-nm, 35-mW, model HL6501MG, or 785 -nm, 80-mW, model DL7140-201, ThorLabs, Inc., Newton, NJ). For fluorescence-enhanced imaging an appropriate wavelength is selected to elicit fluorescence from an embedded fluorophore. A laser diode driver and temperature controller (ThorLabs, Inc., models LDC500 and TEC2000, respectively, Newton, NJ) maintain a constant dc bias and wavelength, while a frequency synthesizer (Marconi Instruments, model 2022D, United Kingdom) superimposes a 13–dBm, 100–MHz sinusoidal signal on the dc current. A Nikon 50-105 mm f/1.8 zoom AF Nikkor camera lens and appropriate optical filters combine to focus diffuse light of the desired wavelength onto the photocathode of the gain-modulated image intensifier (ITT Night Vision, model FS9910C, Roanoke, VA). For fluorescence-enhanced imaging the optical filters consist of a holographic notch-plus band rejection filter (660-nm or 785-nm center wavelength, Kaiser Optical Systems, Inc., Ann Arbor, MI) and a bandpass or interference filter (710-nm center wavelength, model F10-710.0-4-2.00 or 830-nm center wavelength, model F10-830.0-4-2.00, CVI Laser Corporation, Albuquerque, NM) to

reject backscattered excitation light and isolate fluorescence light. Figures 3.10 and 3.11 provide the transmission spectra of the holographic and bandpass filters used in the studies. A second frequency synthesizer (Programmed Test Sources, Inc., model 310M201GYX-53, Littleton, MA) and power amplifier (ENI, model 604L–01, Rochester, NY) provide the modulation to the dc current supplying the photocathode of

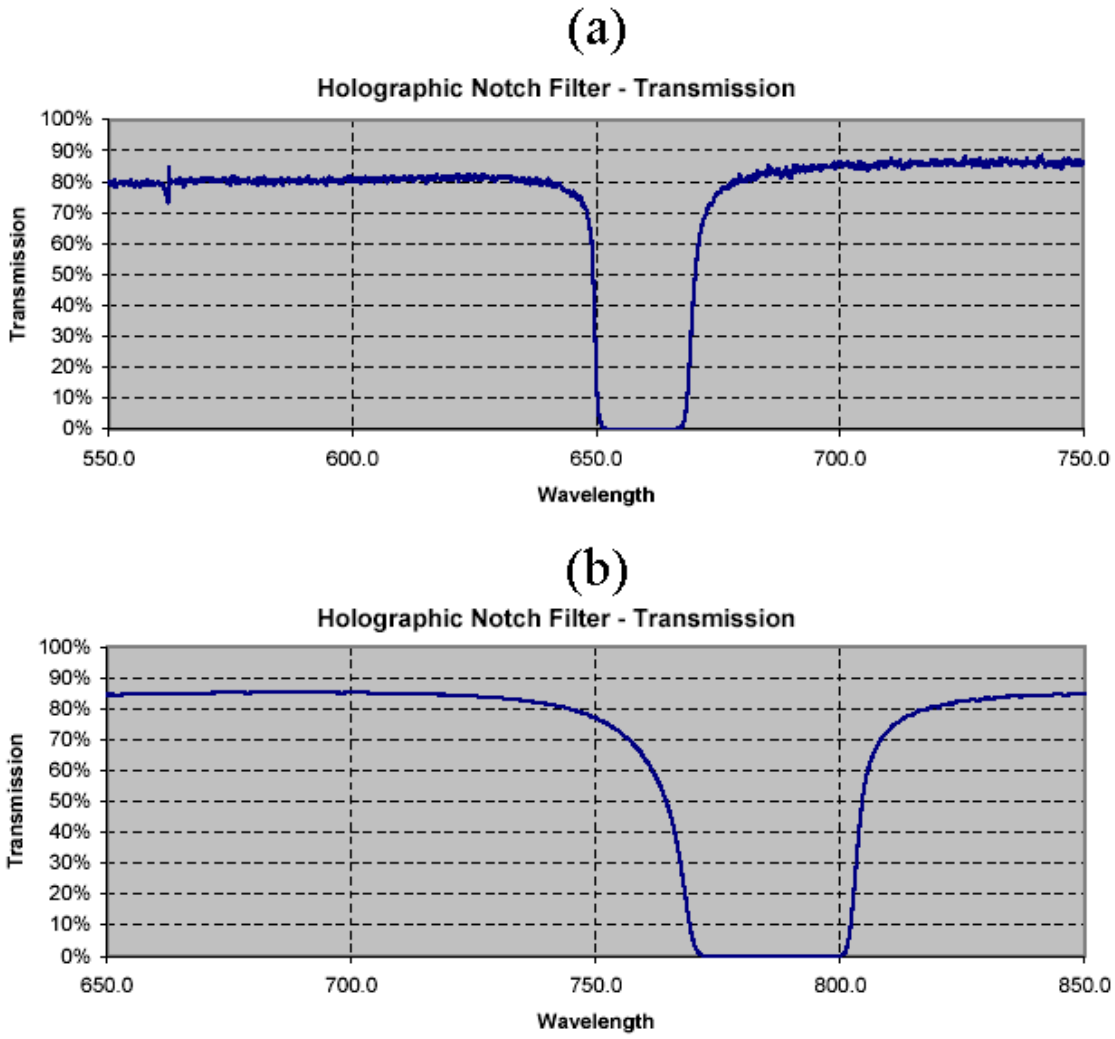

Figure 3.10. Transmission spectra of (a) 660-nm central wavelength and (b) 785-nm central wavelength holographic band rejection filters.[53,54]

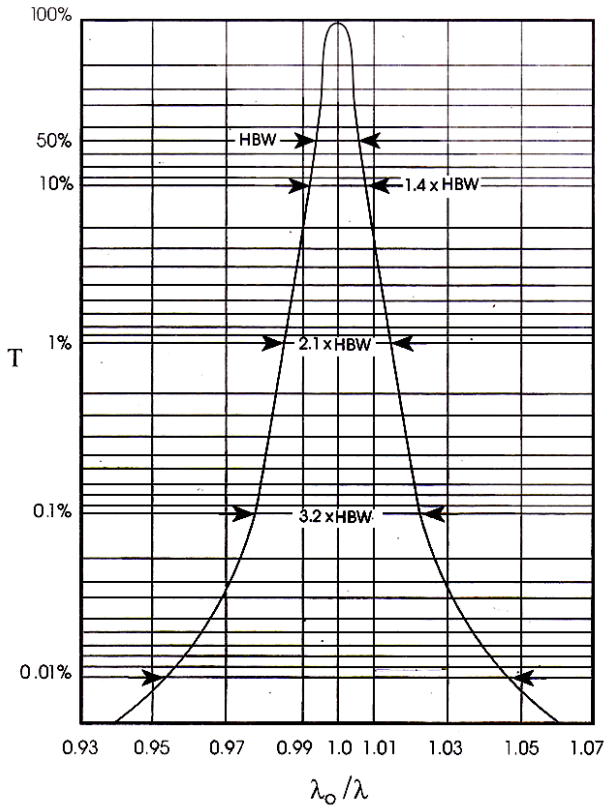

Figure 3.11. Typical transmission curve of the 710-nm center wavelength and 830-nm center wavelength bandpass filters, where the center wavelength is denoted by λ_o and HBW is the half band-width, or the bandwidth at 50% of the peak transmission.[55]

the image intensifier (provided by GBS Micro Power Supply, model PS20060500) at 100–MHz via a bias–T modulation circuit described in the following section. Finally, a Nikon 105 mm f/2.8D AF Micro-Nikkor camera lens transmits the amplified area light image onto the 1024 × 1024 CCD detector array of the 16-bit CCD camera (Photometrics, model CH350, Tucson, AZ). The CCD unit is thermoelectrically cooled to minimize the detection of any inherent dark current.

The synchronous control of all instrumentation and data acquisition is accomplished using via an IEEE–488 GPIB instrument control bus and V++ software (Digital Optics, New Zealand). Subsequent analysis of frequency-domain data is performed using Matlab software (The Mathworks, Inc., Natick, MA).

3.4 Homodyned ICCD Frequency-Domain Operation

To operate in the frequency-domain, both the excitation light source and the detector must be modulated at radio-frequencies, typically on the order of 100-MHz. When the light detector consists of an intensified charge-coupled device (ICCD) camera, the modulation typically occurs at the image tube intensifier,[56-60] although systems that utilize on-off modulation of the CCD itself are also available.[61] As described herein, superimposing an RF frequency onto the dc bias of the photocathode of the tube intensifier provides a convenient method to achieve frequency-domain operation of the detector.

Modulation of the image tube intensifier is accomplished via a bias-T modulation circuit, similar to the one depicted in Figure 3.12, that superimposes an RF signal, typically 100-MHz, on the dc bias of the photocathode. Two resistors, denoted R_1 and R_2, and two capacitors, denoted C_1 and C_2, make up the key components of the bias-T modulation circuit. The first resistor, R_1, provides the circuit load to ensure that there are no circuit-loading effects by the modulation circuit on the ac signal source.[62] For radiofrequencies a 50-Ω load is typical.[62] The second passive component, the capacitor

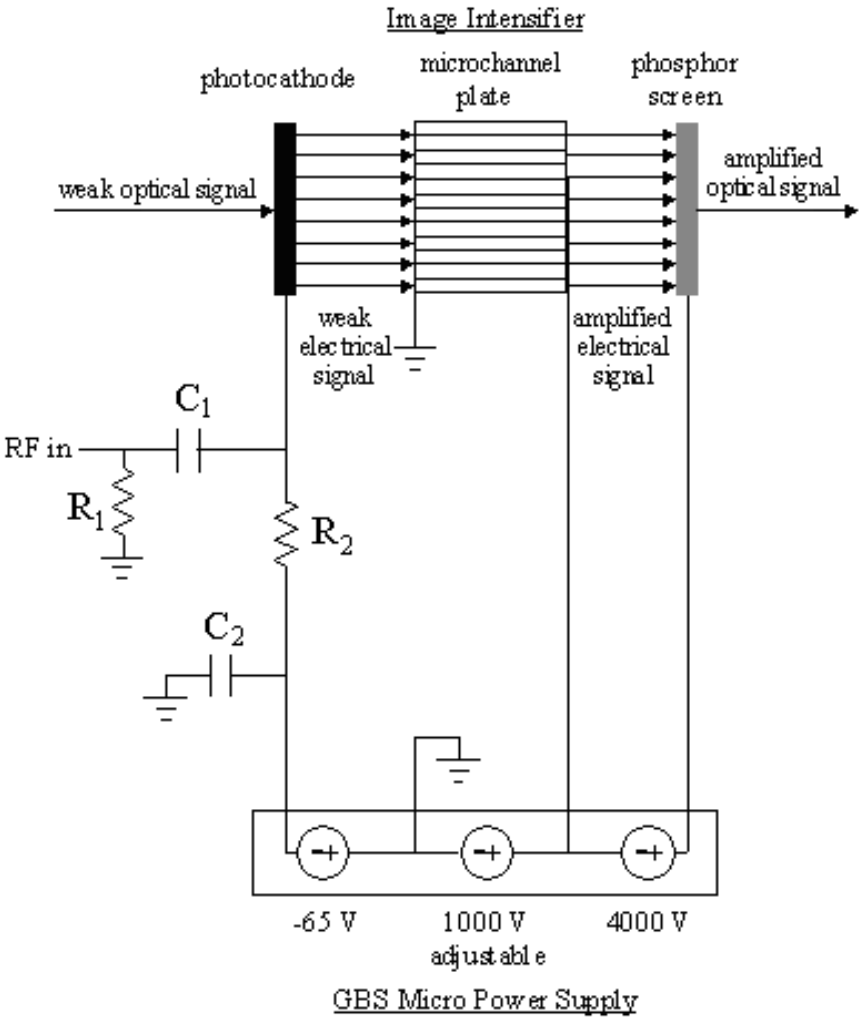

Figure 3.12. Schematic diagram of the bias-T modulation circuit used to provide RF modulation to the photocathode of the image tube intensifier. R_1 and R_2 denote resistors while C_1 and C_2 denote capacitors.

C_1, acts as a dc blocking capacitor to prevent superfluous dc signal from reaching the photocathode. For the modulation circuit designed and constructed for use in the ICCD imager employed for the studies described within this dissertation, C_1 has a value of 11.5-nF. The final two components R_2 and C_2 act together to form a low-pass filter and

prevent the ac signal from reaching the intensifier's power supply. The cutoff frequency or the 'breakpoint' of the filter is defined as:[62]

$$f_{\text{cutoff}} = \frac{1}{2\pi RC}, \tag{3.5}$$

where the frequency is expressed in units of Hz when the resistance R is expressed in Ohms and the capacitance C is expressed in Farads. The cutoff frequency is the frequency above which the output voltage falls below -3dB (70.8%) of the input voltage. Given values of $R_2 = 10\ \text{k}\Omega$ and $C_2 = 11.5\ \text{nF}$, representative of the bias-T modulation circuit employed in the instrumental design, the cutoff frequency is equivalent to $f_{\text{cutoff}} = 1.4\ \text{kHz}$. Thus, this low-pass filter effectively directs the 100-MHz ac signal towards the intensifier's photocathode by preventing it from reaching the power supply.

In the technique of homodyne frequency mixing, the intensity of the excitation light source is modulated at the same frequency as the photodetector. The excitation light source intensity, typically provided by a laser diode, is similarly modulated via a bias-T circuit. Mathematically, the process of homodyne frequency mixing may be explained as the product of two signals – the detected modulated signal received by the image intensifier and the signal modulating the image intensifier, denoted by L and G respectively. The signals L and G may be represented as:[59]

$$L = L_{DC} + L_{AC}\cos\left(\omega t + \theta\right), \tag{3.6}$$

$$G = G_{DC} + G_{AC}\cos\left(\omega t + \eta\right), \tag{3.7}$$

where the subscripts DC and AC denote the dc and ac components of the signals, respectively, t is time, ω is the angular modulation frequency, θ is the phase difference

between the incident excitation wave and the detected wave, and η represents the phase delay imposed by the instruments, that is, η represents the native difference in phase between the signals modulating the laser diode and the image intensifier. Thus, the frequency mixed signal, denoted *S*, is simply the product of*L* and *G*.[59]

$$\begin{aligned} S &= L \times G \\ &= L_{DC}G_{DC} + L_{DC}G_{AC}\cos(\omega t + \eta) + G_{DC}L_{AC}\cos(\omega t + \theta). \\ &\quad + \frac{L_{AC}G_{AC}}{2}\cos(\eta - \theta) + \frac{L_{AC}G_{AC}}{2}\cos(2\omega t + \eta + \theta) \end{aligned} \tag{3.8}$$

Because the phosphor decay time of the intensifier is on the order of msec and photodetection occurs on the order of μsec (100-Mhz modulation frequency), the image intensifier inherently acts as a low-pass filter.[59] As a result, the signal observed at the image intensifier is a steady state signal, denoted S_{obs}, and only contains the dc and low frequency components of the mixed signal,[59]

$$S_{obs} = L_{DC}G_{DC} + \frac{L_{DC}G_{AC}\cos(\eta - \theta)}{2}. \tag{3.9}$$

Determination of the frequency-domain properties characteristic of the propagation of the detected light wave, namely phase shift, θ, and the modulation amplitude, denoted I_{AC}, is accomplished at each pixel in the multi–pixel detection array. The process involves stepping the phase of the image intensifier relative to the laser diode, η, at regular intervals through a complete 2π cycle.[60,63,64] During each phase delay, η_d, the CCD camera acquires an image which is stored as an intensity array. Following completion of the 2π cycle, a Fast Fourier transform (FFT) of the phase-sensitive

intensity data yields the phase shift, θ_{ij} , and modulation amplitude, I_{ACij} at each pixel (denoted by *i* and *j*) using the following relationships:[63,64]

$$\theta_{ij} = \arctan\left(\frac{\mathrm{Im}\left[I\left(f_{\max}\right)_{ij}\right]}{\mathrm{Re}\left[I\left(f_{\max}\right)_{ij}\right]}\right), \tag{3.10}$$

$$I_{ACij} = \frac{\left[\left\{\mathrm{Im}\left[I\left(f_{\max}\right)_{ij}\right]\right\}^2 + \left\{\mathrm{Re}\left[I\left(f_{\max}\right)_{ij}\right]\right\}^2\right]^{1/2}}{N/2}, \tag{3.11}$$

where $\mathrm{Im}[I(f_{max})_{ij}]$ and $\mathrm{Re}[I(f_{max})_{ij}]$ represent the imaginary and real components of the digital frequency spectrum maximum, respectively, at each pixel, and *N* is the total number of phase delays.

3.5 Limitations to i*n Vivo* Fluorescence Imaging

Despite the efforts to isolate and detect only the re-emitted fluorescent light, the major limitation to the detection of ultra low concentrations of fluorophore, and hence, ultra-low levels of fluorescent light remains the inability to completely eliminate extraneous sources of light, primarily back-reflected excitation light. Although the holographic notch-plus band rejection filter and narrow-band interference filter combine to provide greater than six orders of magnitude rejection of excitation light, the intensity of the remaining transmitted back-reflected excitation light is on the same order as the fluorescence intensity from nanomolar concentrations of fluorophore located at a depth of 4-cm within a scattering media.[37] Thus, the current state of optics imposes the limit to deep-tissue fluorescence imaging to nanomolar concentrations of fluorophore.[37]

In addition to the noise imparted by back-reflected excitation light, there exists a number of discrete noise sources that may corrupt images by reducing the SNR , especially when operating in the frequency-domain. Because frequency-domain photon migration imaging utilizes RF-modulated electronics, FDPM imaging is susceptible to electronic or RF interference. RF interference can result from proximity to electrical wires and instruments, termed RF leakage. Because electronic noise sources abound, especially in experimental laboratories and clinics, RF interference may result in less than ideal performance. Great care must be taken to properly shield all sensitive components and electronics.

Finally, another obstacle in fluorescence-enhanced imaging is the inherent non-uniformity of excitation light field. The excitation light source, provided by a laser diode, is expanded via a plano-convex lens to provide a larger field of view for imaging. However, even with the most advanced lens optics available, a completely uniform expanded excitation source is unachievable. Furthermore, because the re-emitted fluorescence intensity is proportional to the product of the fluorophore concentration and the local excitation light fluence, a non-uniform excitation light field may lead to erroneous conclusions. For example, the underlying assumption in fluorescence imaging *in vivo* is that the highest fluorescence intensity signal arises from the area where the local concentration of fluorophore is the greatest. While this holds true when the excitation light fluence is uniformly distributed, as is often the case, the excitation light fluence distribution is far from ideal. Thus, the resulting fluorescence images, rather than reflecting the local fluorophore concentration, may instead echo the local excitation

light fluence. As a result, great effort must be made to provide an excitation light field that is as close to uniform as possible.

One such way to accomplish that task is via the use of holographic diffuser in combination with the plano-convex light expanding lens. The end result is a more diffuse and hence, more uniform, excitation light field. Figure 3.13 illustrates the effect of the holographic diffuser. Figures 3.13(a) and 3.13(b) are images obtained of the

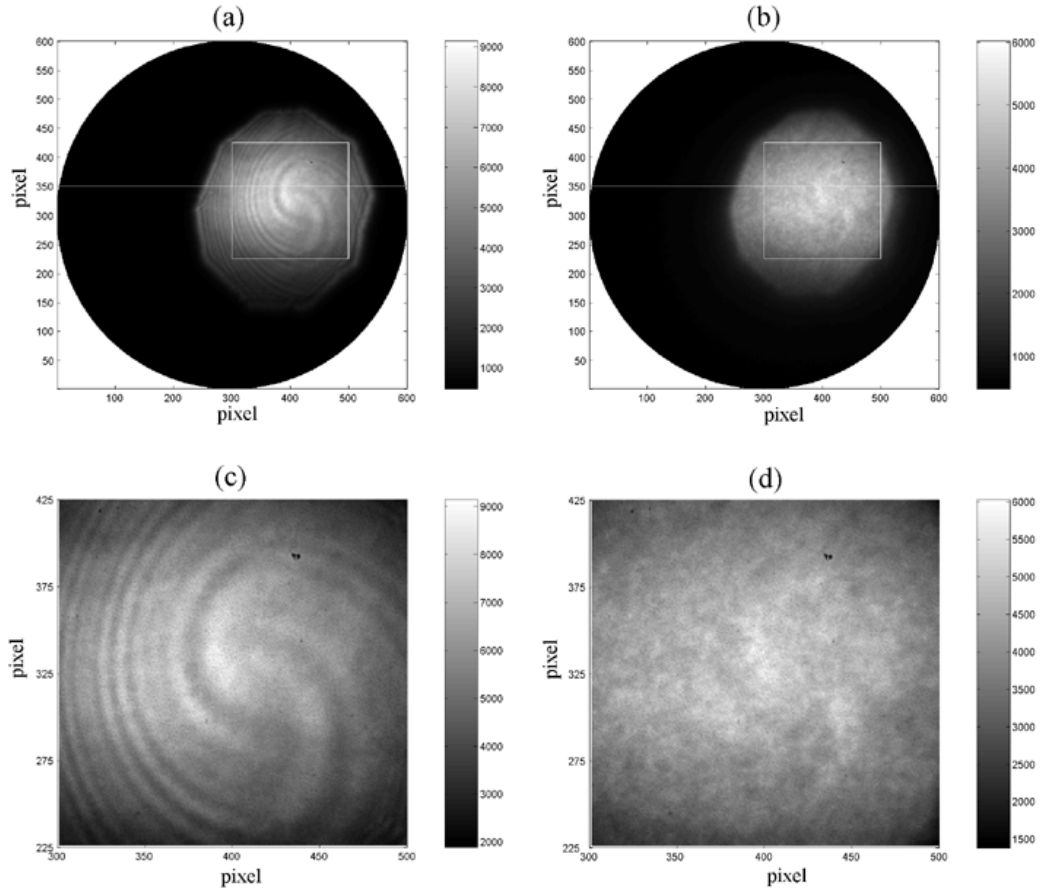

Figure 3.13. Images obtained of the expanded excitation light fluence (a) without and (b) with the use of a holographic diffuser. The images in panels (c) and (d) are the enlarged regions highlighted by the white boxes in panels (a) and (b), respectively.

expanded excitation light field using the instrumentation described in the previous section with and without the use of a holographic diffuser, respectively. Figures 3.13(c)and 3.13(d) are enlarged views of the regions outlined by the white boxes in Figures 3.13(a) and 3.13(b), respectively. From the figures, the effect of the diffuser is evident. With the presence of the holographic diffuser, the excitation light field is clearly more uniform.

Unfortunately, the added uniformity provided by the holographic diffuser comes at the expense of decreased excitation light intensity and, for frequency-domain studies, decreased modulation depth. Figure 3.14 shows the intensity profile along a horizontal

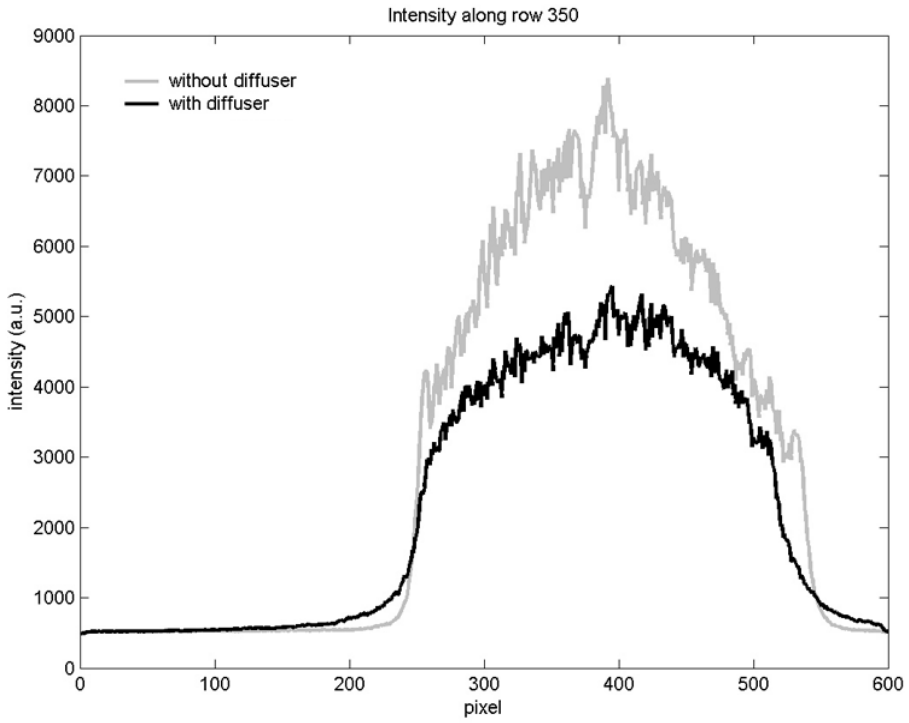

Figure 3.14. Intensity profile along a horizontal slice through the images in Figures 3.13(a) and 3.13(b). While the intensity is more uniform with the holographic diffuser present, the intensity is reduced by nearly 40%.

slice through the images in Figures 3.13(a) and 3.13(b) (denoted by the white horizontal line). From the intensity profile, although the improvement in uniformity is again quite noticeable; the signal intensity is reduced by approximately 40% by the addition of the holographic diffuser. Finally, the holographic diffuser decreases the modulation of the excitation light source such that the time-variant sinusoidal nature of the light wave is essentially eliminated. A frequency-domain study was conducted with and without the diffuser present. Four phase-sensitive images of the expanded excitation source were obtained at each of 16 equally spaced phase delays between the oscillators modulating the laser source and detector. An FFT of the phase-sensitive images yielded measurements of average light intensity (DC) and modulation amplitude (AC) over a region of interest overlying the expanded source light. The addition of the holographic diffuser resulted in a decrease of the modulation amplitude, defined as the dimensionless ratio of AC/DC, of approximately 83% (from 15.3 to 2.6). As a result, the use of a holographic diffuser to achieve a uniform excitation light source is inappropriate for frequency-domain studies. To obtain a near-uniform excitation light field and yet maintain adequate modulation depth, the area of the expanded light source must be decreased. While this may be adequate for the preliminary *in vivo* frequency-domain studies presented in Section 8, the limitation imposed by the non-uniformity of the excitation light is a topic which requires further inquiry before the imaging system operates optimally.

This section concludes the discussion on background and instrumentation. The necessary first step following the design and assembly of the ICCD instrumentation

described in detail within this section was to validate the accuracy of experimentally obtained measurements of frequency-domain photon migration. The following section describes experimental work designed to test and validate the instrumentation by using measurements of FDPM to characterize the optical properties of turbid, tissue-like media.

4. DETERMINATION OF OPTICAL PROPERTIES OF SEMI-INFINITE TURBID MEDIA USING AREA MEASUREMENTS OF FREQUENCY-DOMAIN PHOTON MIGRATION OBTAINED WITH AN ICCD DETECTION SYSTEM

The following section describes experimental work initially intended to test and validate frequency-domain measurements obtained by an intensified charge-coupled device (ICCD) homodyne detection system. The measurements, obtained from the surface of turbid, tissue-like media, were used in conjunction with a diffusion theory of light transport to obtain estimates of the optical properties characteristic of the media. The work, which represents the first time area measurements of frequency-domain photon migration have been utilized to characterize optical properties of scattering media, is pending publication in *Journal of Biomedical Optics*.

4.1 Introduction

With recent advances in optics and medicine it is becoming increasingly more important to acquire rapid and accurate measurements of light propagation from the tissue surface and, using those measurements, infer the physiology of the underlying tissue. Successful near-infrared (NIR) optical imaging necessitates the accurate collection of diffusely propagated light at the tissue surface as well as an optimization approach to recover or map the optical properties of the underlying tissue volume.

The study of light propagation through turbid media can broadly be divided into one of two classes: steady-state or continuous wave (CW) techniques, and time-resolved approaches, either in the time-domain (time-domain photon migration, TDPM) or in the

frequency-domain (frequency domain photon migration, FDPM). Steady-state techniques employ a light source whose intensity is constant in time. In these techniques, the spatially resolved diffuse reflectance may be used with the steady-state diffusion equation to obtain estimates of the optical properties.[65-68] On the other hand, time-resolved techniques, as the name implies, measure the optical response of a system to a light source whose intensity varies in time. Time-domain techniques employ ultra-fast light pulses (on the order of femto- to picosecond) to irradiate the medium under investigation and photon counting or gated detectors to capture the broadened and attenuated pulse some distance away from the source. The measured pulse shape may then be fitted to a theoretical expression to obtain the absorption and scattering coefficients.[68,69] In frequency-domain approaches, the light source intensity is modulated at high frequencies (on the order of MHz) and a phase-sensitive detector is used to measure the amplitude attenuated, phase-shifted light signal. The characteristics of the detected light wave may then be used to determine the absorption and scattering coefficients of the medium.[70 79]

In many cases, the measurements used to determine the optical properties of turbid media are obtained using an infinite media geometry in which the source light and detected light, delivered and captured via fiber optics, are located deep within the media.[70-75,79] Certainly the determination of optical properties has applications outside medical imaging for which the infinite geometry is well suited. However, for applications in medical imaging, the infinite media geometry is hardly applicable. Thus, the determination of optical properties requires a more relevant half-space or semi-

infinite geometry.[68,69,75-79] Furthermore, the measurements must be rapid to ensure that data collection concludes within a clinically acceptable time frame. To this end an intensified charge-coupled device (ICCD) imaging system has been developed, capable of operation in the frequency domain, and capable of acquiring rapid area measurements of photon migration.[57,59,60] Herein, the said system is used to obtain estimates of the optical properties of homogenous turbid media. The results, which compare favorably to estimates obtained via a well-characterized single-pixel FDPM technique, further validate the ICCD detection system and its capacity to obtain frequency-domain data. To the author's knowledge, this study presents the first time frequency-domain measurements obtained using an area detector of the form of an ICCD camera system have been employed to determine the absorption and reduced scattering coefficients of turbid media.

In the following sections, diffusion theory of light propagation in turbid media is first reviewed to establish the theoretical framework. Next, the experimental method including the instrumentation used for the acquisition of area frequency-domain data and the scattering media investigated is described and the data analysis procedure is detailed. Finally, the experimental results are presented and compared with the results obtained from a well-characterized single-pixel frequency-domain system to demonstrate the validity of the technique.

4.2 Theory

The propagation of near-infrared light through biological tissue and other scattering media can be described by the radiative transport equation (RTE). Given conditions of

high scattering and sufficient source-detector separation,[80] a diffusion approximation, described in detail in Appendix A, may be applied to the RTE to yield a mathematical formulation more conducive to the study of light transport in turbid media. Thus, diffusion theory is often used to describe the time-dependent photon passage through turbid or highly scattering media and often finds applicability in studies of time-domain photon migration, where source light is launched as ultra-short pulses and photon detection is achieved as a function of time and position. Additionally, for studies of frequency-domain photon migration, where the incident source light intensity is sinusoidally modulated, an adequate description of photon migration is provided by the diffusion equation:

$$\frac{i\omega}{c}\Phi(\mathbf{r},\omega) - D\nabla^2\Phi(\mathbf{r},\omega) + \mu_a\Phi(\mathbf{r},\omega) = S(\mathbf{r},\omega). \tag{4.1}$$

Here, i is the principal square root of -1, c is the speed of light in the medium, $\Phi(\mathbf{r},\omega)$ is the AC photon fluence rate at position $\mathbf{r}$ and angular modulation frequency ω, $S(\mathbf{r},\omega)$ is the isotropic photon source density, and D is the diffusion coefficient defined by:

$$D = \frac{1}{3[\mu_a + (1-g)\mu_s]} = \frac{1}{3(\mu_a + \mu_s')}, \tag{4.2}$$

where μ_s and μ_a are the inverses of the mean free paths for scattering and absorption and are known as the scattering and absorption coefficients, respectively, μ_s' is known as the isotropic scattering coefficient and g is the mean cosine of the scattering angle.

4.2.1 Analytical Solutions to the Diffusion Equation

For infinite and semi-infinite media geometries, the diffusion equation may be solved analytically to obtain an expression for the photon fluence rate. Herein, the method of Haskell *et al.* is followed and the extrapolated boundary condition is applied to solve for the AC photon fluence rate at the surface.[79] This boundary condition states that the photon fluence rate goes to zero at some fictitious boundary located a distance l_s above the physical surface, with l_s defined as:

$$l_s = \frac{1 + R_{eff}}{1 - R_{eff}} 2D, \tag{4.3}$$

where R_{eff} is the effective reflection coefficient and represents the fraction of photons that is internally reflected at the boundary. R_{eff} is a function of the refractive indices (n_i) of the turbid media and surroundings and has a value of 0.431 for a refractive index mismatch typical of that of a water-air interface ($n_{water}/n_{air} = 1.33$). The expression for the surface AC photon fluence rate may then be expressed as:

$$\Phi(\mathbf{r},\omega) = \frac{S}{4\pi D}\left\{\frac{\exp\left[-\mathrm{r}_1\left(\frac{c\mu_a - i\omega}{cD}\right)^{1/2}\right]}{\mathrm{r}_1} - \frac{\exp\left[-\mathrm{r}_2\left(\frac{c\mu_a - i\omega}{cD}\right)^{1/2}\right]}{\mathrm{r}_2}\right\}, \tag{4.4}$$

where S is a complex number representative of the source AC strength (S_{AC}) and phase (θ_s), such that,

$$S = S_{AC}\exp(i\theta_s), \tag{4.5}$$

and r_1 and r_2 are the distances from the point of interest to the true source located just beneath the surface and to the image source introduced to satisfy the boundary condition, respectively, and ρ is equivalent to the projection of r_1 and r_2 onto the surface, such that (see Fig. 4.1),

$$r_1 = \left[(3D)^2 + \rho^2\right]^{1/2}, \tag{4.6}$$

$$r_2 = \left[(3D + 2l_s)^2 + \rho^2\right]^{1/2}. \tag{4.7}$$

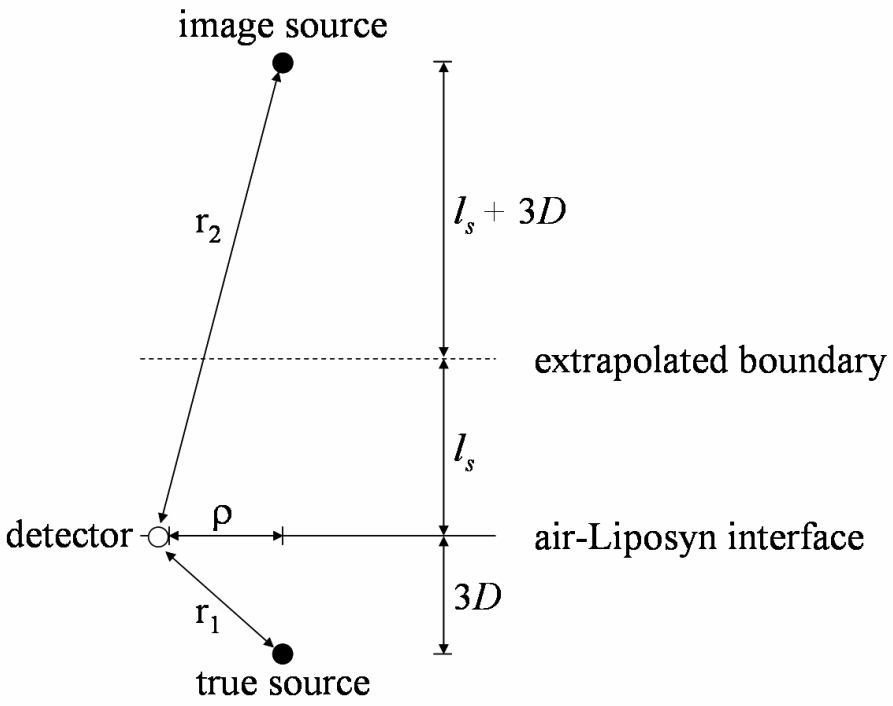

Figure 4.1. Schematic depicting the semi-infinite model. The true source is located a distance of one mean-free path length ($3D$) below the surface of the medium, while the image source is located a distance of $2l_s + 3D$ above the surface to create a net-zero fluence at the extrapolated boundary located a distance of l_s above the surface. The true source and image source are located a distance of r_1 and r_2, respectively, from the detector, and ρ is the projection of r_1 and r_2 onto the surface.

A case of particular importance and pertinent to this report involves a reflectance geometry detection scheme, where the source and detected light are located on the same surface. In this case, the detected signal or the diffuse reflectance, denoted by R, is that portion of the diffuse light that is transmitted through the surface and captured by the detector. It can be shown that the diffuse reflectance is proportional to the photon fluence rate at the surface:[79]

$$R(\rho,\omega) = A\Phi(\rho,\omega), \tag{4.8}$$

where A is a proportionality constant equivalent to:

$$A = \frac{1}{2}\int_0^{\alpha_o}[1 - R_{Fresnel}(\alpha)]\left[1 + \frac{3D}{l_s}\cos\alpha\right]\cos\alpha\sin\alpha\,\mathrm{d}\alpha\,. \tag{4.9}$$

Here, α_o is equal to one-half of the detector acceptance angle and $R_{Fresnel}$, the Fresnel reflection coefficient, is a function of the refractive indices of the turbid media and surroundings. For a system with a refractive index mismatch of 1.33, and a detector with a large acceptance angle (such as a camera), A has a value of 0.199. Thus, when Eq. (4.4) and Eq. (4.9) are applied to Eq. (4.8) one obtains an analytical expression for the diffuse reflectance at the medium surface:

$$R(\rho,\omega) = \frac{0.199S}{4\pi D}\left\{\frac{\exp\left[-\left[(3D)^2+\rho^2\right]^{1/2}\left(\frac{c\mu_a - i\omega}{cD}\right)^{1/2}\right]}{\left[(3D)^2+\rho^2\right]^{1/2}}\right. \tag{4.10}$$
$$\left. - \frac{\exp\left[-\left[(3D+2l_s)^2+\rho^2\right]^{1/2}\left(\frac{c\mu_a - i\omega}{cD}\right)^{1/2}\right]}{\left[(3D+2l_s)^2+\rho^2\right]^{1/2}}\right\}$$

Several approaches may be applied to determine the optical parameters of a semi-infinite media given frequency domain measurements. In one such approach, ρ is fixed and measurements are obtained as a function of ω. Alternatively, measurements may be obtained for a fixed ω as a function of ρ. Finally, a technique that utilizes both a fixed modulation frequency and a fixed separation distance sequentially may be applied. An algorithm based on the measurement approach applied and the analytical solution to the diffusion approximation may then be used to regress the unknown optical properties. The imaging system described herein is capable of obtaining data at a number of modulation frequencies. However, its capacity to obtain measurements simultaneously from an area of the medium surface makes it convenient to obtain frequency domain data for multiple values of ρ simultaneously at a fixed frequency. Thus, herein the attention is focused on a frequency-domain method that employs a fixed modulation frequency and measurements obtained at a number of distances from the source to determine unknown optical parameters of scattering media.

4.2.2 Absolute versus Relative Measurements

In the frequency domain, the measured quantities are the steady-state reflectance or DC amplitude, denoted by I_{DC}, the modulation or AC amplitude, denoted I_{AC}, and the phase angle between the source and detector, θ. These quantities are related to the diffuse reflectance by the following expression:

$$R(\rho,\omega) = I_{AC}(\rho,\omega)\exp[i\theta(\rho,\omega)], \tag{4.11}$$

where $I_{AC}(\rho,\omega)$, is the modulus of the diffuse reflectance, and $\theta(\rho,\omega)$, is the argument of the diffuse reflectance. Consequently, the steady-state reflectance, modulation amplitude, and the phase angle are found via the following relationships:

$$I_{DC}(\rho) = R(\rho, \omega = 0) \tag{4.12}$$

$$I_{AC}(\rho,\omega) = |R(\rho,\omega)| = \left\{IMAG[R(\rho,\omega)]^2 + REAL[R(\rho,\omega)]^2\right\}^{1/2} \tag{4.13}$$

$$\theta(\rho,\omega) = \arg[R(\rho,\omega)] = \arctan\left(\frac{IMAG[R(\rho,\omega)]}{REAL[R(\rho,\omega)]}\right), \tag{4.14}$$

where $IMAG[R(\rho,\omega)]$ and $REAL[R(\rho,\omega)]$ refer to the imaginary and real components of the diffuse reflectance, respectively, and $R(\rho,\omega)$ is the diffuse reflectance defined by Eq. (4.10). Thus, given the distance from the source, angular modulation frequency, and optical properties of the medium, Eqs. (4.12 – 4.14), when applied to the analytical expression for the diffuse reflectance, may be used to obtain theoretical or predicted values of steady-state reflectance, modulation amplitude, and phase angle.

Moreover, frequency-domain measurements may be absolute or relative. If absolute measurements are to be used, the proportionality constant A needs to be determined. An additional calibration experiment must also be performed in order to characterize the source AC strength and phase since the quantity S appears in the analytical solution for the photon fluence rate. On the other hand, since the diffuse reflectance is a linear function in both the quantities A and S, dividing the diffuse reflectance obtained at one position by a measurement obtained at a second reference position cancels both quantities and obviates the need to calculate the proportionality

constant and characterize the source. Hence, relative FDPM measurements may be calculated using the relationships:

$$I_{DC}^{rel}(\rho) = \frac{I_{DC}(\rho)}{I_{DC}(\rho_{ref})} = \frac{R(\rho, \omega = 0)}{R(\rho_{ref}, \omega = 0)} \tag{4.15}$$

$$I_{AC}^{rel}(\rho, \omega) = \frac{I_{AC}(\rho, \omega)}{I_{AC}(\rho_{ref}, \omega)} = \frac{\left\{IMAG\left[R(\rho, \omega)\right]^2 + REAL\left[R(\rho, \omega)\right]^2\right\}^{1/2}}{\left\{IMAG\left[R(\rho_{ref}, \omega)\right]^2 + REAL\left[R(\rho_{ref}, \omega)\right]^2\right\}^{1/2}} \tag{4.16}$$

$$\begin{aligned}\theta^{rel}(\rho, \omega) = \theta(\rho, \omega) - \theta(\rho_{ref}, \omega) = &\arctan\left(\frac{IMAG\left[R(\rho, \omega)\right]}{REAL\left[R(\rho, \omega)\right]}\right) \\ &- \arctan\left(\frac{IMAG\left[R(\rho_{ref}, \omega)\right]}{REAL\left[R(\rho_{ref}, \omega)\right]}\right),\end{aligned} \tag{4.17}$$

where the superscript *rel* denotes relative measurements, ρ_{ref} represents the distance from the source at some reference position, and $R(\rho, \omega)$ is the diffuse reflectance defined by Eq. (4.10).

A second, perhaps greater advantage to using relative data for the determination of optical properties involves the uniqueness of the derived optical parameters. Kienle and Patterson previously demonstrated that the determination of optical properties is not unique if absolute measurements of steady-state reflectance are used.[78] Figure 4.2(a) presents a contour plot of the steady-state diffuse reflectance typical of measurements obtained from an air-water interface using a detector with a large numerical aperture, (i.e. n_{water}/n_{air}=1.33, R_{eff}= 0.431, A = 0.199), obtained using Eq. (4.12), versus the absorption and reduced scattering coefficients for ρ = 0.5 cm. The value S, representative of the source was further assumed to equal unity. From the plot it is evident that for certain

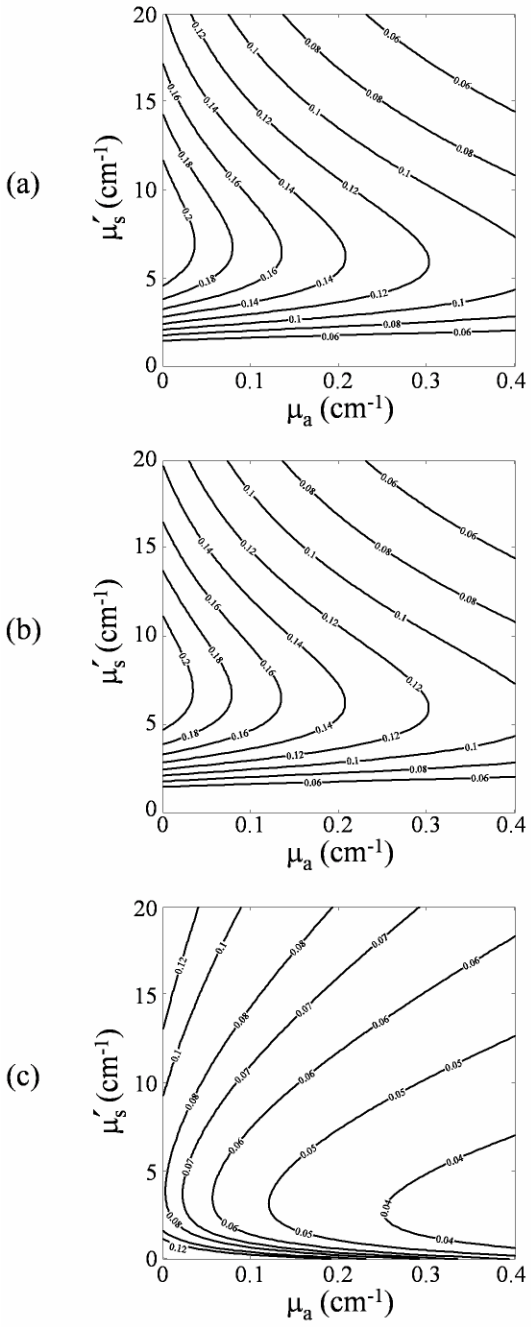

Figure 4.2. Contour plots of (a) steady-state diffuse reflectance (cm^{-2}), (b) AC amplitude (cm^{-2}), and (c) phase angle (radians). Values were obtained using Eqs. (4.12), (4.13), (4.14) and (4.10) with ρ = 0.5-cm and $\omega = 2\pi\times$(100-MHz). A source strength of unity was assumed (S = 1).

fixed values of the absorption coefficient, two separate values of the reduced scattering coefficient will yield the same steady-state diffuse reflectance.

Similarly, Figures 4.2(b) and 4.2(c) demonstrate that for certain values of the absorption coefficient, multiple values of the reduced scattering coefficient can produce the same value of the AC amplitude and phase angle [computed using Eqs. (4.13 – 4.14), with $\omega = 2\pi\times(100\text{-MHz})$]. As a result, the determined optical properties will be non-unique if absolute measurements of steady-state reflectance, AC amplitude, or phase angle are used alone or if a combination of absolute measurements are employed (i.e. superimposing Figures 4.2(a), 4.2(b), and 4.2(c) still results in multiple pairs of absorption and scattering coefficients that yield the same results).

On the other hand, the use of relative measurements leads to the determination of a unique set of optical parameters. Figures 4.3(a), 4.3(b), and 4.3(c) display contour plots of normalized steady-state reflectance, normalized AC amplitude, and referenced phase angle, respectively, versus the absorption and reduced scattering coefficients. The values were calculated using Eqs. (4.15 – 4.17) for $\rho = 1.0$ cm and normalized or referenced to those obtained at a distance of $\rho_{ref} = 0.5$ cm. As in Figure 4.2, the effective reflection coefficient was assigned a value of $R_{eff} = 0.431$ and the angular modulation frequency was set to $\omega = 2\pi\times(100\text{-MHz})$ but no assumption about the source was necessary and the proportionality constant A was not required in the calculation. The plots in Figure 4.3 demonstrate that for any fixed value of the absorption coefficient, there exists only one value of the reduced scattering coefficient that will yield a given value of normalized steady-state reflectance, normalized AC amplitude, or referenced

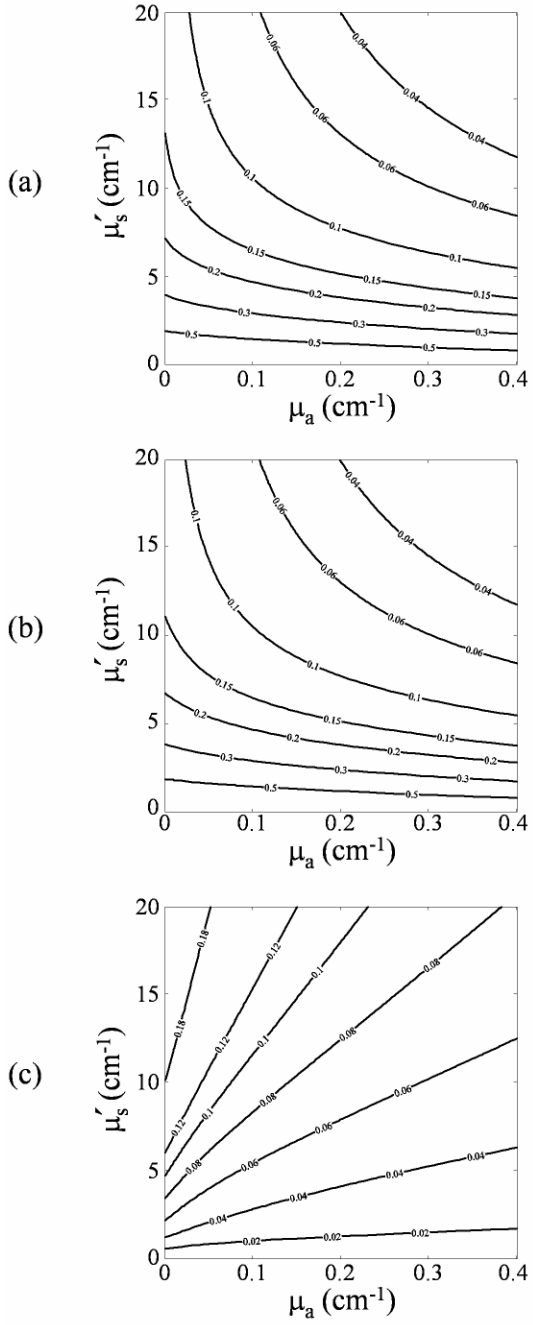

Figure 4.3. Contour plots of (a) normalized steady-state diffuse reflectance (a.u.), (b) normalized AC amplitude (a.u.), and (c) referenced phase angle (radians). Values were obtained using Eqs. (4.15), (4.16), (4.17) and (4.10) with ρ = 1.0-cm, ρ_{ref} = 0.5-cm., and $\omega = 2\pi\times$(100-MHz).

phase angle. As a result, relative measurements of steady-state reflectance, AC amplitude, or phase angle may be used alone or in combination to determine a unique pair of optical properties.

The following section describes the instrumentation, experimental setup, and experimental method employed for data acquisition as well as details the data analysis procedure used to obtain the final estimates of the optical properties of the turbid media investigated.

4.3 Materials and Methods

4.3.1 Instrumentation

The frequency domain imaging system is described in detail in Section 3. Hence, only the salient features are described. Modulated light of 785-nm provided by a laser diode (ThorLabs, Inc., model DL7140-201, Newton, NJ) was launched onto the surface of the medium under investigation via a 1000-μm optical fiber. The fiber was positioned perpendicularly such that the tip just touched the medium surface. A laser diode driver (ThorLabs, model LDC500, Newton, NJ) provided the diode with 50-mA of dc current while a temperature controller (ThorLabs, model TEC2000, Newton, NJ) helped maintain a constant lasing wavelength. A 100-MHz ac signal of +13-dBm RF power, provided by a frequency synthesizer (Marconi Instruments, model 2022D, United Kingdom), was superimposed onto the constant dc bias of the laser diode. Consequently, the diode delivered approximately 48-mW of optical power to the source fiber.

A 16-bit CCD camera (Photometrics, model CH350/L, Tucson, AZ) coupled to an image intensifier via a 105-mm lens functioned as an area detector of the re-emitted light. A circular image of the medium surface of approximately 3.4-cm diameter was focused onto the photocathode of the image intensifier with a 50-mm lens. A neutral density filter was positioned prior to the 50-mm lens to prevent saturation of the CCD. A second frequency synthesizer (Programmed Test Sources, model PTS-310, Littleton, MA) provided an ac signal of +13-dBm, further amplified to +40-dBm using an external amplifier (ENI, model 604L, Rochester, NY), that was used to modulate the photocathode of the intensifier at 100-MHz. The synthesizers were phase locked to maintain a constant programmable phase offset. Because both source and detector were modulated at the same frequency, a homodyne data acquisition technique was employed to facilitate the collection of frequency domain data. The phase offset between frequency generators was swept through a 2π cycle in order to obtain phase sensitive intensity images that were subsequently used in an FFT analysis to obtain the quantities of steady-state diffuse reflectance, amplitude modulation, and phase angle (for a detailed description the reader is referred to reference 60). Data acquisition and instrumentation control was performed on a personal computer equipped with V++ imaging software (Digital Optics, Auckland, New Zealand). A schematic of the instrumentation is provided in Figure 4.4.

4.3.2 Scattering Media

The scattering media was comprised of 20% Liposyn (Abott Laboratories, Chicago, IL) diluted with distilled, deionized water to a final volume percent of 0.5%, 1.0%, and 2.0%

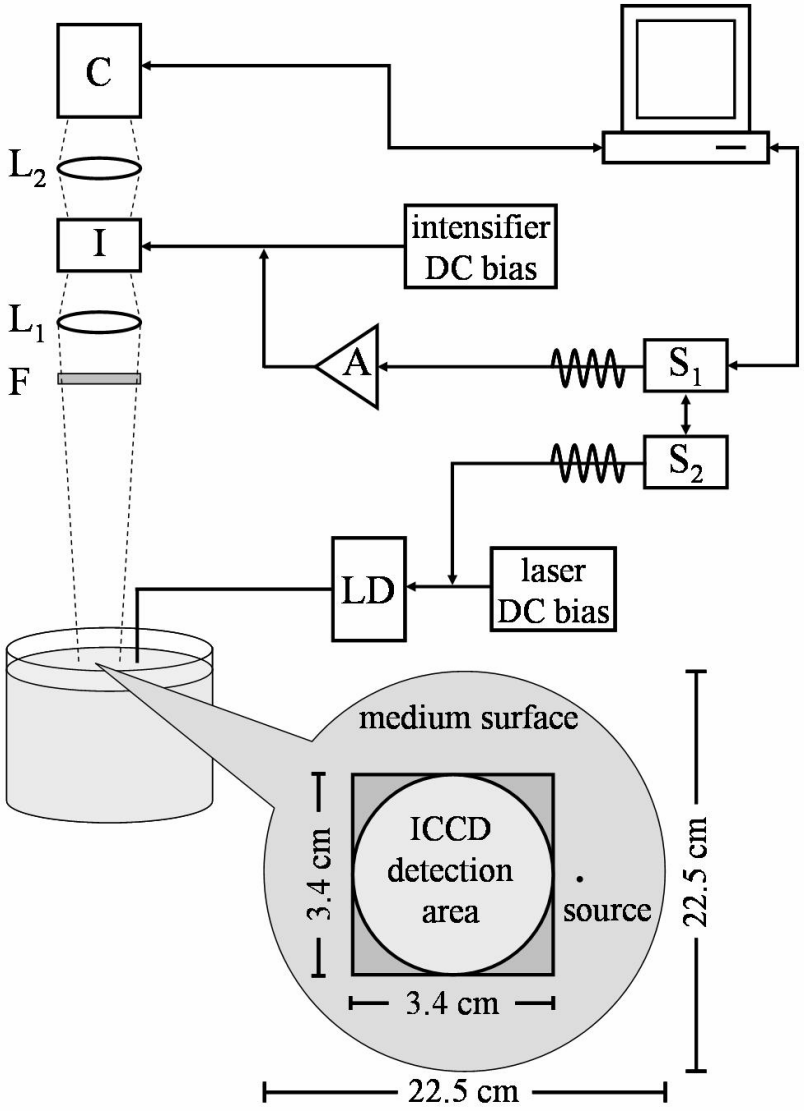

Figure 4.4. Frequency-domain intensified charge-coupled device (ICCD) imaging system. The source light provided by a laser diode (LD) is delivered through an optical fiber to the medium surface. The re-emitted light passes through a neutral density filter (F) before being focused onto the photocathode of the image intensifier (I) by a lens (L_1). The intensifier is optically coupled via a lens (L_2) to a CCD camera (C) which acquires and digitizes the images. A frequency synthesizer (S_1) provides an RF signal, further amplified by an external amplifier (A), that modulates the intensifier photocathode at 100-MHz. A second synthesizer (S_2) modulates the laser diode at the same 100-MHz frequency.

to vary the degree of scattering. The reduced scattering coefficients of the turbid media were measured by a colleague, Tianshu Pan, using a single-pixel frequency-domain technique described elsewhere[74] and agree well with previously published reports.[81,82] Additionally, India ink dye (Pro Art, Mt. Laurel, N.J.) was added in various concentrations to vary the extent of light absorption.[83] The extinction coefficient for the India ink was determined using dilute samples in a standard spectrophotometer (SPEX FluoroLog, Jobin Yvon, Inc., Edison, NJ) and Beer's Law calculations. It was found to have a value of $\varepsilon_{785nm}^{ink} = 1.12\ cm^{-1}(vol\%)^{-1}$. The absorption coefficient due to the ink at 785-nm may then be calculated as:

$$\mu_a^{ink} = 2.303 \times \varepsilon_{785nm}^{ink} \times \left[\text{conc. ink}\left(vol.\%\right)\right]. \tag{4.18}$$

Using Eq. (4.18) it is possible to calculate the increase in the absorption coefficient as a result of added India ink dye as $\mu_a = \mu_a^{ink} + \mu_a^o$, where μ_a^o represents the absorption prior to the addition of the dye. In order to vary the final absorption coefficient, the concentration of ink was adjusted between 0% and 0.07% by volume. Hence, a total of nine solutions were investigated. Table 4.1 summarizes the composition of the nine solutions investigated.

4.3.3 Experimental Method

A cylindrical container constructed from clear acrylic with a diameter of 22.5-cm housed the Liposyn-ink solutions during the experiment. The container was filled with the solution to a depth of approximately 10.5-cm yielding a final volume of approximately 4-L. With the source fiber located on the medium surface and the ICCD imager

Table 4.1. Summary of the different media investigated. The media were comprised of Liposyn and India ink in the concentrations indicated. The range of ρ examined for each medium is listed in column 4. Additionally, the optical parameters calculated via the single-pixel frequency-domain technique discussed in reference 74 are listed for each medium.

solution	Liposyn concentration (vol. %)	India ink concentration (vol. %)	ρ (cm)	optical parameters determined from single-pixel measurements (mean ± std. dev.)[74]	
				μ_a (cm^{-1})	μ_s' (cm^{-1})
1	0.5	0	2.04 – 3.35	0.019 ± 0.003	5.3 ± 0.2
2	0.5	0.03	2.04 – 3.35	0.104 ± 0.001	5.9 ± 0.1
3	0.5	0.07	2.04 – 3.35	0.21 ± 0.02	6.3 ± 0.1
4	1.0	0	1.17 – 2.38	0.015 ± 0.002	10.2 ± 0.3
5	1.0	0.03	1.17 – 2.38	0.088 ± 0.001	10.4 ± 0.1
6	1.0	0.07	1.17 – 2.38	0.18 ± 0.03	10.8 ± 0.2
7	2.0	0	0.67 – 1.38	0.018 ± 0.001	22.3 ± 0.3
8	2.0	0.03	0.67 – 1.38	0.091 ± 0.001	22.3 ± 0.2
9	2.0	0.07	0.67 – 1.38	0.31 ± 0.04	21.8 ± 0.8

positioned to acquire images from the clear cylindrical sides of the acrylic container, the validity of the semi-infinite medium was verified as any re-emitted light from the sides of the container was undetectable.

Just prior to the start of each experiment, an image was acquired of a grid to determine the field of view and the exact location of the fiber optic with respect to it. The acrylic container was then filled with a well mixed Liposyn-ink solution until the surface just touched the fiber tip. The frequency domain imaging procedure then commenced. A total of nine images were acquired at each of 32 equally spaced phase delays between the synthesizers modulating the light source and the detector. With a 400-msec exposure per image, data acquisition time totaled approximately 2 minutes ([exposure time / image] × [images / phase delay] × [number of phase delays]). Hence, there was little concern of the solution settling due to the duration of the data acquisition. The procedure was repeated for all the solutions investigated.

4.3.4 Data Analysis

Frequency domain data was extracted from the phase sensitive images of the medium surface via a fast Fourier transform (FFT) procedure described in detail elsewhere.[60] The nine images obtained per phase delay yielded nine independent area measurements of steady-state reflectance, modulation amplitude, and phase angle per investigational medium studied. The standard deviations of the nine measurements were computed for use in the non-linear least-squares algorithm discussed below. Having previously determined the position of the source with respect to the field of view, the data was then sorted into radial bins centered on the source (see Fig. 4.5). The width of each bin was

(a)

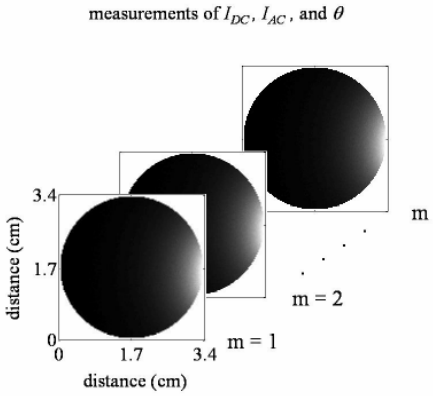

(b)

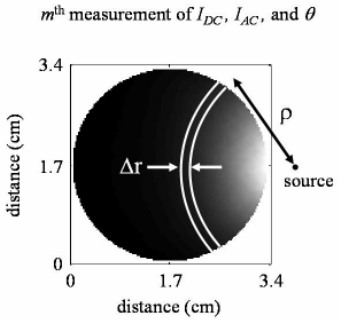

(c)

$$\rho = \begin{bmatrix} \rho_1 \\ \rho_2 \\ \cdot \\ \cdot \\ \cdot \\ \rho_n \end{bmatrix} \qquad I_{DC} = \begin{bmatrix} I_{DC\,1,1} & I_{DC\,1,2} & \cdots & I_{DC\,1,m} \\ I_{DC\,2,1} & & & \cdot \\ \cdot & & & \cdot \\ \cdot & & & \cdot \\ I_{DC\,n,1} & \cdots & & I_{DC\,n,m} \end{bmatrix}$$

$$\theta = \begin{bmatrix} \theta_{1,1} & \theta_{1,2} & \cdots & \theta_{1,m} \\ \theta_{2,1} & & & \cdot \\ \cdot & & & \cdot \\ \cdot & & & \cdot \\ \theta_{n,1} & \cdots & & \theta_{n,m} \end{bmatrix} \qquad I_{AC} = \begin{bmatrix} I_{AC\,1,1} & I_{AC\,1,2} & \cdots & I_{AC\,1,m} \\ I_{AC\,2,1} & & & \cdot \\ \cdot & & & \cdot \\ \cdot & & & \cdot \\ I_{AC\,n,1} & \cdots & & I_{AC\,n,m} \end{bmatrix}$$

Figure 4.5. Schematic of the radial binning procedure. (a) A total of *m* area measurements of I_{DC} , I_{AC}, and θ are (b) sorted into radial bins of width Δr = 1000-μm. (c) Data within each bin is averaged to yield a single measurement corresponding to projected distance from the source, ρ. The number of area measurements, *m*, is dictated by the number of images obtained per phase delay, and *n* represents the number of separation distances.

1000-μm, equivalent to the diameter of the source fiber. Data within each bin was averaged to yield one measurement corresponding to its surface-projected distance from the source, ρ. The first or shortest distance determined ρ_{ref}, the reference position, and subsequent measurements of steady-state reflectance, amplitude modulation, and phase angle were made relative to the measurements obtained at this position. In all cases this first position was ensured to be located at least 10 mean free path lengths from the source to preserve the validity of the diffusion approximation.[80]

Relative frequency domain measurements were obtained at source-detector separation distances ranging from 6.7-mm to 33.5-mm. A nonlinear least squares analysis was then performed to fit the derived analytical solution to the obtained experimental measurements of steady-state reflectance, modulation amplitude, and phase angle in order to recover the optical properties of the medium. Each FDPM measurement type could be utilized separately or in combination in the least squares analysis. Thus, the parameters were extracted from the frequency-domain data sets in one of the following ways: $I_{DC}^{rel}(\rho)$ data were fit to Eq. (4.15); $I_{AC}^{rel}(\rho,\omega)$ data were fit to Eq. (4.16); $\theta^{rel}(\rho,\omega)$ data were fit to Eq. (4.17); $I_{DC}^{rel}(\rho)$ and $I_{AC}^{rel}(\rho,\omega)$ were simultaneously fit to Eqs. (4.15) and (4.16), respectively; $I_{DC}^{rel}(\rho)$ and $\theta^{rel}(\rho,\omega)$ were simultaneously fit to Eqs. (4.15) and (4.17), respectively; $I_{AC}^{rel}(\rho,\omega)$ and $\theta^{rel}(\rho,\omega)$ were simultaneously fit to Eqs. (4.16) and (4.17), respectively; and finally, $I_{DC}^{rel}(\rho)$, $I_{AC}^{rel}(\rho,\omega)$, and $\theta^{rel}(\rho,\omega)$ were simultaneously fit to Eqs. (4.15), (4.16), and (4.17), respectively. As a result, a single FDPM data set yielded estimates of the optical parameters obtained

in seven different ways. Furthermore, because essentially nine independent FDPM area measurements were obtained per experiment, the least-squares analysis yield nine estimates of the optical parameters for each of the measurement combinations employed in the algorithm. The non-linear least squares fitting routine employed is part of the commercial package Matlab software (The MathWorks, Natick, MA). The objective function minimized was of the form:

$$F\left(\mu_a, \mu_s'\right) = \frac{1}{2}\sum_i \sum_j \left(\frac{\xi_j^{pred} - \xi_j^{obs}}{\sigma_j^{obs}} \right)^2 , \tag{4.19}$$

where the subscript *i* denotes the measurement type (I_{DC}^{rel} , I_{AC}^{rel} , and θ^{rel}) obtained at the j^{th} distance from the source, ξ^{pred} and ξ^{obs} represent the predicted and observed measurements, respectively, and σ^{obs} is the standard deviation of the observed measurements.

4.4 Results and Discussion

Table 4.2 summarizes the experimentally obtained estimates for the optical parameters of the different media investigated. The optical parameters are reported as the mean of the nine estimates obtained for each of the seven measurement combinations applied in the regression. To validate the results we compare them with the values obtained using the single-pixel frequency-domain technique. Although single-pixel FDPM is itself prone to some degree of experimental error, in general, it is regarded as a technique with high accuracy and measurement precision and as such, is widely used for the determination of optical properties of turbid media.[74] Therefore, the values obtained

Table 4.2. Summary of the results of the least-squares regression to determine the optical properties of the media investigated. The obtained optical properties are shown along with the frequency-domain measurement type(s) that was (were) used in the regression. The results shown represent the mean of nine separate trials. The standard deviation is typically less than 0.006 cm^{-1} and 0.05 cm^{-1} for the absorption and reduced scattering coefficients, respectively. The value *nc* denotes the cases where the regression algorithm did not converge on a set of optical parameters.

		0% India ink		0.03% India ink		0.07% India ink	
	measurement(s) employed in least squares analysis	μ_a (cm^{-1})	μ_s' (cm^{-1})	μ_a (cm^{-1})	μ_s' (cm^{-1})	μ_a (cm^{-1})	μ_s' (cm^{-1})
0.5 % Liposyn	steady-state reflectance	0.003	1.70	0.009	1.48	0.006	1.21
	AC amplitude	0.020	5.06	0.106	5.05	0.174	5.51
	phase	0.021	5.15	0.101	4.94	0.196	5.15
	steady-state reflectance and AC amplitude	0.017	5.42	0.104	5.11	0.166	5.76
	steady-state reflectance and phase	0.021	5.14	0.097	4.81	0.162	4.42
	AC amplitude and phase	0.021	5.15	0.101	4.96	0.193	5.09
	steady-state reflectance, AC amplitude, and phase	0.021	5.15	0.101	4.96	0.193	5.08
1.0 % Liposyn	steady-state reflectance	0.011	6.47	0.058	6.45	0.096	6.81
	AC amplitude	0.018	9.55	0.110	9.59	0.195	10.48
	phase	0.019	9.93	0.100	9.49	0.194	9.23
	steady-state reflectance and AC amplitude	0.018	9.64	0.106	9.82	0.148	13.39
	steady-state reflectance and phase	0.019	9.93	0.100	9.48	0.192	9.14
	AC amplitude and phase	0.019	9.93	0.100	9.49	0.195	9.26
	steady-state reflectance, AC amplitude, and phase	0.019	9.93	0.100	9.49	0.195	9.26
2.0 % Liposyn	steady-state reflectance	*nc*	*nc*	*nc*	*nc*	0.106	11.96
	AC amplitude	0.016	16.38	0.084	16.04	0.073	25.27
	phase	0.021	20.89	0.122	20.41	0.276	25.76
	steady-state reflectance and AC amplitude	0.016	16.33	0.083	15.98	0.081	22.75
	steady-state reflectance and phase	0.021	20.89	0.122	20.40	0.276	25.74
	AC amplitude and phase	0.021	20.89	0.122	20.41	0.276	25.75
	steady-state reflectance, AC amplitude, and phase	0.021	20.89	0.122	20.41	0.276	25.75

using the single-pixel FDPM method provide a practical metric by which to evaluate the accuracy of our experimental results.

The following formula is used to compute the percent relative error in the experimentally derived optical parameters:

$$\%\ relative\ error\ in\ \mu = \left| \frac{\mu^{calc} - \mu^{sp}}{\mu^{sp}} \right| \times 100\,, \tag{4.20}$$

where μ^{calc} represents the calculated optical coefficient and μ^{sp} is the value obtained from the single-pixel FDPM analysis. In general, when measurements of steady state diffuse reflectance were employed, either alone or in combination with another measurement type, the resulting optical parameters were most in error. That is, they possess the highest relative error indicating that they deviate most from the optical parameters computed via the single-pixel technique. This finding is in accord with the results of Sun *et al.* who also determined that simultaneous regression of I_{DC}^{rel} and I_{AC}^{rel} failed to accurately recover the optical properties.[74]

Table 4.3 summarizes the mean relative error in estimating the optical parameters for each of the measurement combinations used in the least squares analysis for all media investigated. The mean relative error in determining the absorption and reduced scattering coefficients using DC measurements alone, as computed via Eq. (4.20), was approximately 64% and 54% respectively. The addition of amplitude and phase measurements considerably improved this result.

Furthermore, it can be seen from Table 4.2 that measurements of steady-state reflectance underestimated the optical parameters. Perhaps this is a result of the

Table 4.3. Mean relative errors in determining the optical properties of all semi-infinite media investigated. The relative error is computed using Eq. (4.20) for each of the measurement combinations used in the least-squares analysis.

	% relative error	
measurement(s) employed in least-squares analysis	μ_a	μ_s'
steady-state reflectance	63.7	54.3
AC amplitude	19.2	13.2
phase	14.4	10.7
steady-state reflectance and AC amplitude	20.4	13.2
steady-state reflectance and phase	16.5	12.3
AC amplitude and phase	14.6	10.7
steady-state reflectance, AC amplitude, and phase	14.6	10.7

additional signal contained in DC measurements that arises from the detection of ambient light. The additional signal due to ambient light produces a greater DC signal collected from the medium, especially at distances further from the source. This increased DC signal is incorrectly interpreted as light that has propagated and exited the medium. As a result, the absorption and scattering coefficients are underestimated. Although precautions were made to negate extraneous light, sources of ambient light beyond experimental control created less than ideal dark-room conditions. Although not employed in the studies presented herein, in general, a background subtraction technique may be used to eliminate the dc intensity associated with ambient light.[57] Under experimental conditions similar to those described within this text and employing a background subtraction technique, Thompson and Sevick-Muraca demonstrated that the ICCD imager operated in the photon-noise limit, or in terms of signal-to-noise ratio (SNR), the optimum in detector performance.[57] Therefore, because the DC

measurements that were employed contained some degree of ambient light, a resulting decrease in SNR could explain the less precise DC measurements.

In addition, because the least-squares regression utilized an optimization function weighted by the standard deviations of obtained measurements, and the obtained measurements of I_{DC}^{rel} were generally less precise than measurements of I_{AC}^{rel} and θ^{rel} ($\sigma_{I_{DC}} > \sigma_{I_{AC}}, \sigma_{\theta}$), the analyses that employed a combination of measurements favored measurements of I_{AC}^{rel} and θ^{rel} over measurements of I_{DC}^{rel}. That is, like the conclusions made by Sun *et al.*,[74] the results indicate that simultaneous regression of I_{DC}^{rel}, I_{AC}^{rel}, and θ^{rel} data gives comparable recovered results as simultaneous regression of I_{AC}^{rel} and θ^{rel}. Consequently, the estimates of the optical parameters were minimally influenced by the addition of I_{DC}^{rel} measurements in the least-squares analysis.

On the other hand, because modulation amplitude and phase lag measurements are independent of ambient light conditions and were obtained with greater precision, the optical parameters determined from measurements of I_{AC}^{rel} and θ^{rel} either alone or in combination deviated least from the values obtained using the single-pixel FDPM technique. Typically, the use of phase measurements alone or in combination with measurements of modulation amplitude resulted in the determination of the optical parameters that most closely matched the values determined by the single-pixel frequency-domain analysis. The mean relative error, as computed by Eq. (4.20), was approximately 15% and 11% in the determination of the absorption and reduced scattering coefficients, respectively, for both cases. In addition, the calculated

absorption coefficients agreed quite well with those computed using the added absorber calculation provided by Eq. (4.18).

Figure 4.6 shows the experimentally acquired I_{DC}^{rel} measurements and the corresponding predicted values obtained from a least-squares analysis using

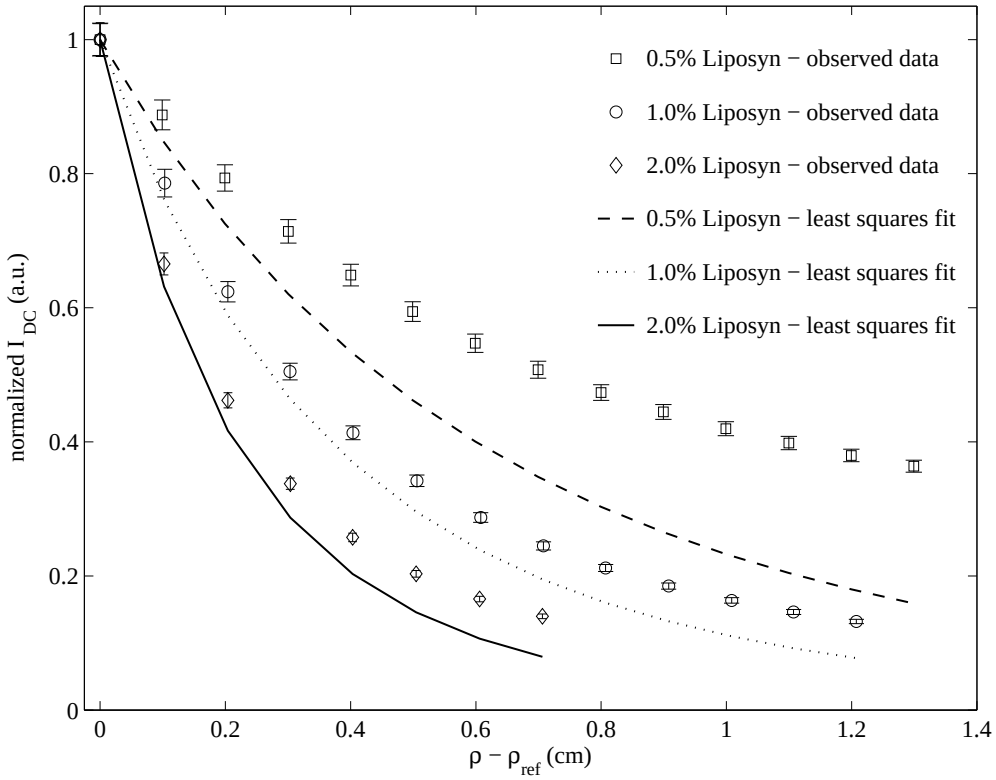

Figure 4.6. Experimentally obtained measurements of normalized I_{DC} intensity (a.u.) as a function of distance from the source (cm) for solutions containing various concentrations of Liposyn emulsion and no added ink absorber. The symbols and error bars denote the mean and standard deviations of the measurements, respectively, whereas the lines represent the results of a least-squares analysis that employed I_{AC} and θ measurements to determine the optical parameters.

measurements of I_{AC}^{rel} and θ^{rel} collectively for media comprised of various concentrations of Liposyn and no added ink absorber. The plot demonstrates the degree to which the obtained steady-state reflectance measurements deviate from diffusion theory over the distances investigated. Similarly, Figures 4.7 and 4.8 report the

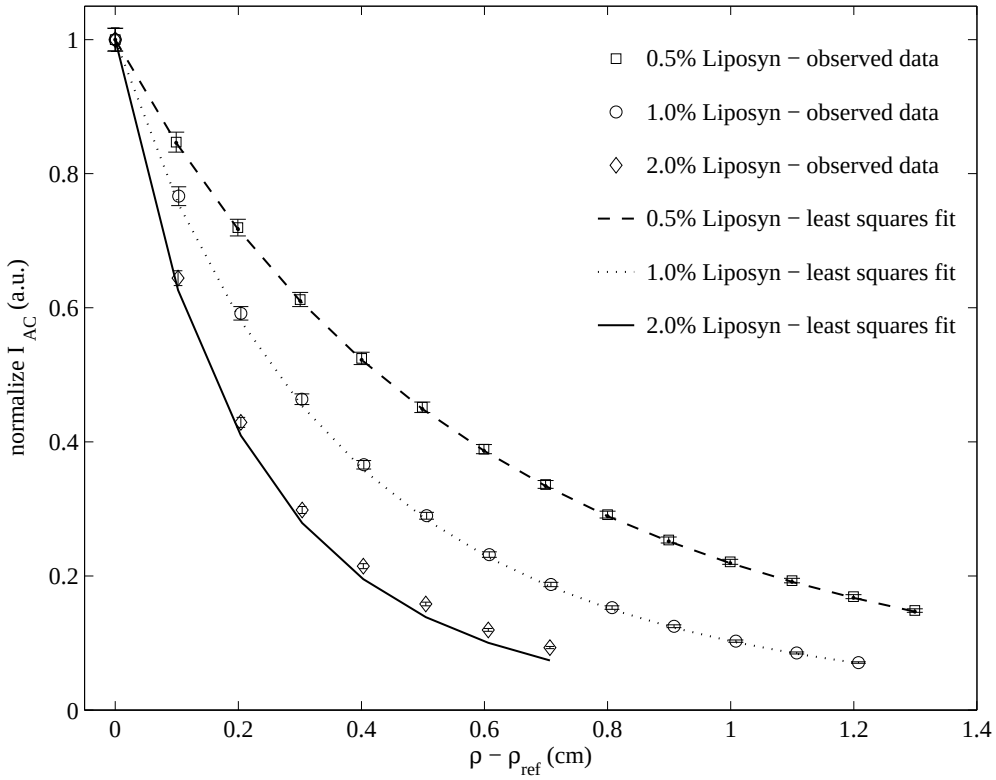

Figure 4.7. Experimentally obtained measurements of normalized I_{AC} intensity (a.u.) as a function of distance from the source (cm) for solutions containing various concentrations of Liposyn emulsion and no added ink absorber. The symbols and error bars denote the mean and standard deviations of the measurements, respectively, whereas the lines represent the results of a least-squares analysis that employed I_{AC} and θ measurements to determine the optical parameters.

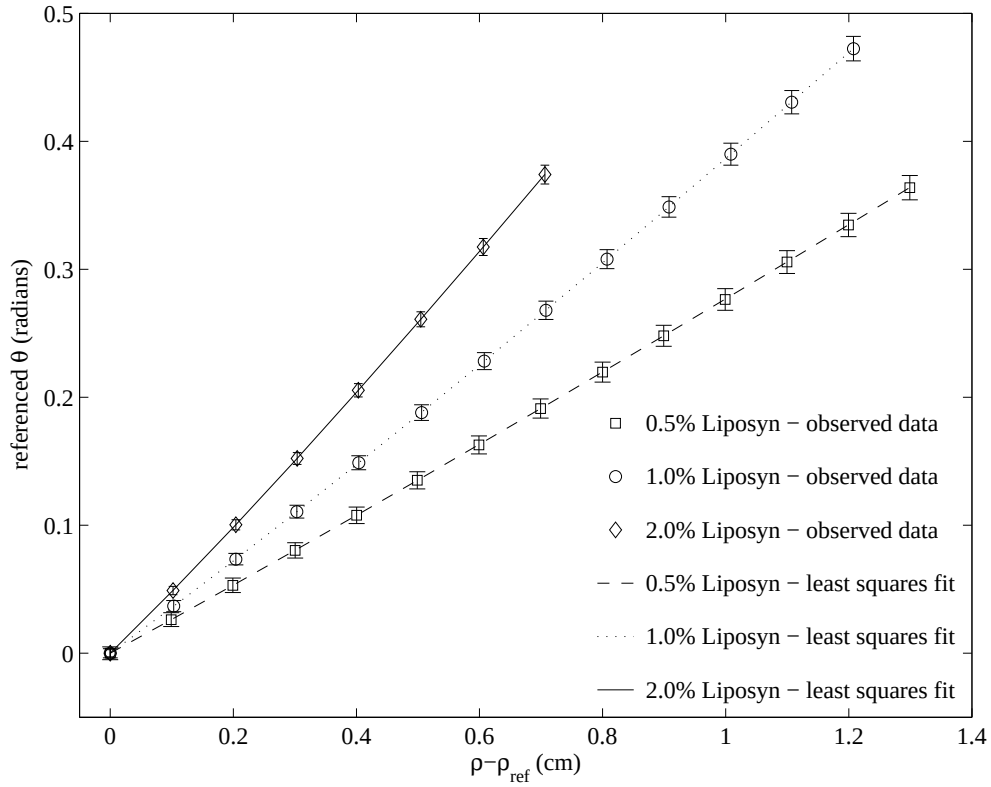

Figure 4.8. Experimentally obtained measurements of referenced phase lag (radians) as a function of distance from the source (cm) for solutions containing various concentrations of Liposyn emulsion and no added ink absorber. The symbols and error bars denote the mean and standard deviations of the measurements, respectively, whereas the lines represent the results of a least-squares analysis that employed I_{AC} and θ measurements to determine the optical parameters.

experimentally acquired measurements of I_{AC}^{rel} and θ^{rel}, respectively, as well as the corresponding predicted values obtained via a simultaneous least-squares analysis of I_{AC}^{rel} and θ^{rel} data for media comprised of various concentrations of Liposyn and no added ink absorber. Unlike Figure 4.6, these plots demonstrate that measurements of amplitude modulation and phase lag agree relatively well with theoretical predictions.

The results for the solutions containing added India ink absorber are akin to Figures 4.6, 4.7, and 4.8.

Finally, to investigate the effect of modulation frequency on the determination of the optical properties, measurements were performed at three additional distinct modulation frequencies (40-MHz, 60-MHz, and 80-MHz) for the solution comprised of 0.5% Liposyn. The gathered I_{AC}^{rel} and θ^{rel} data were then employed in the least squares analysis to obtain estimates for the optical parameters. Figure 4.9 presents the obtained absorption and reduced scattering coefficients as the mean of nine separate trials. The estimates at modulation frequencies of 40-MHz, 60-MHz, and 80-MHz are consistent with the results obtained at a modulation frequency of 100-MHz. Again, the obtained absorption coefficients were found to deviate from the value obtained via the single-pixel technique by on average approximately 17% over all the modulation frequencies investigated. Similarly, the reduced scattering coefficient was found on average to within 2% of the single-pixel value.

4.5 Conclusion

Herein the use of an ICCD detector for the collection of frequency-domain photon migration data and its subsequent use in determining the optical properties of semi-infinite turbid media has been demonstrated. Referenced measurements obtained at multiple source-detector positions and the diffusion approximation were employed to regress estimates for the absorption and reduced scattering coefficients. The results indicate that measurements of steady-state diffuse reflectance were least accurate in

modulation frequency (MHz)	μ_a (cm^{-1})	μ_s' (cm^{-1})
40	0.0196	5.27
60	0.0242	5.46
80	0.0249	5.25
100	0.0204	5.15

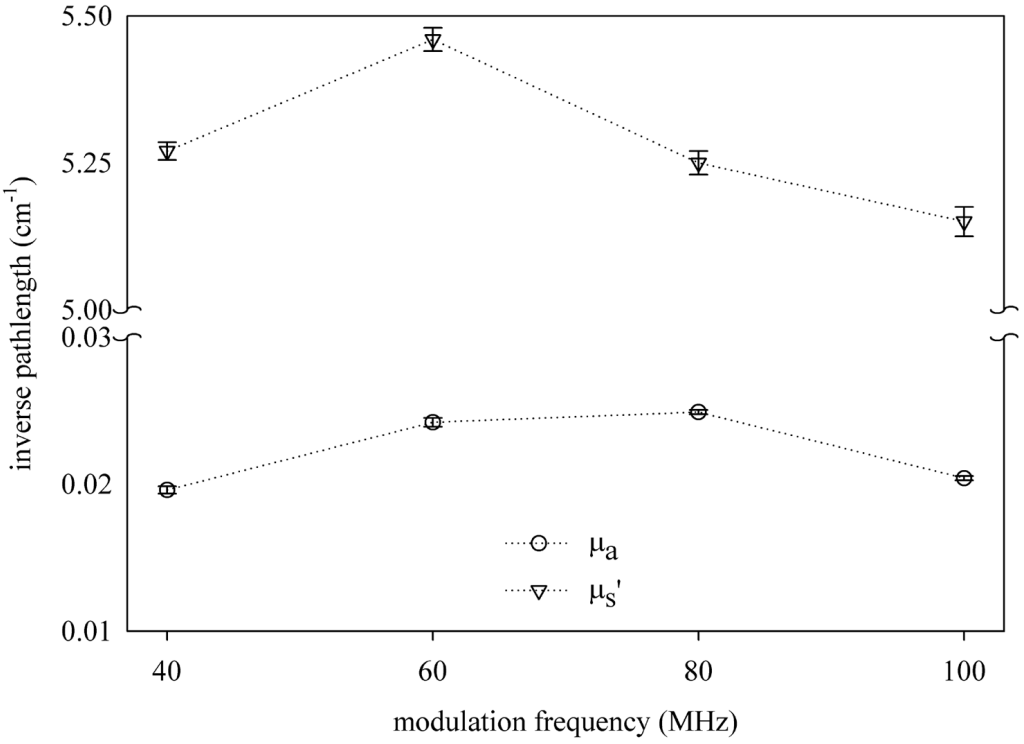

Figure 4.9. Estimates of the optical parameters of a solution comprised of 0.5% Liposyn and no added ink absorber. The optical parameters were acquired via a least-squares analysis using measurements of modulation amplitude and phase lag. The experiments employed the various modulation frequencies listed in the first column of the table. The symbols denote the mean of nine estimates while the error bars indicate the standard deviations.

determining both the absorption and reduced scattering coefficients, with estimates varying from values calculated by an independent single-pixel FDPM technique by on average approximately than 64% and 54%, respectively. Furthermore, the results suggest that measurements of phase lag provide the most accuracy in determining optical

parameters when a single type of measurement is employed; phase lag measurements yielded estimates for the absorption and reduced scattering coefficients that varied by on average approximately 14% and 11% , respectively.

The least-squares regression algorithm that was employed could exploit multiple measurement types simultaneously. The results deviated most from the estimates obtained via single-pixel FDPM technique when the combinations of measurements included steady-state reflectance. This is due in part to the detection of ambient light and it is believed that employing a background subtraction technique should improve the results. On the other hand, the most accurate estimates of the optical parameters were obtained when amplitude data were employed along with phase lag data. In this case, the estimates for the absorption and reduced scattering coefficients again varied from values computed by the single-pixel technique by on average approximately 15% and 11%, respectively. Finally, it was determined that the results were consistent at multiple modulation frequencies spanning 40 – 100-MHz. In summary, it is recommended that the optical properties of semi-infinite media be obtained from an analysis of phase shift data or the simultaneous regression of amplitude and phase shift data.

As a final note, the estimates obtained for the accuracy of the derived optical parameters were calculated using reference values, that themselves, were obtained from an independent experimental technique. As a result, because the true optical properties of the media investigated were unknown, the accuracy of the results that were obtained can in fact represent a conservative estimate. Nonetheless, this study demonstrates for the first time the use of an ICCD detection system to acquire simultaneous surface area

FDPM measurements for purposes of estimating the absorption and scattering coefficients of turbid media. Additionally, the results validate the use of an ICCD detection system for FDPM analysis on systems that exhibit tissue-like scattering.

With the validating studies completed, the ICCD imaging system was transported to M.D. Anderson Cancer Center in Houston, Texas and the research focus turned to the evaluation of fluorescent contrast agents for diagnostic imaging of cancer. Beginning with the following section, experimental work on *in vivo* fluorescence imaging of cancer in animal subjects is discussed.

5. PHARMACOKINETICS OF ICG AND HPPH-CAR FOR THE DISCRIMINATION OF TUMOR TISSUE IN A CANINE MODEL*

Although the work presented in this section chronologically preceded the development of the imaging system described in the previous sections, it represents the first clinical studies of fluorescence imaging on animals conducted by the Photon Migration Laboratories, and as such, appears as the first section of experimental fluorescence imaging *in vivo*. The studies were conducted as a collaborative effort at the Lovelace Respiratory Research Institute in the summer of 1998, several months prior to the author's joining the research group. Thus, experimental data collection, animal care, and preparation of fluorescent dyes was performed by colleagues and collaborators who are gratefully acknowledged and individually recognized in the Acknowledgments section located in the preamble to this dissertation. Although the data was obtained by colleagues, the pharmacokinetic analysis of the data was performed entirely by the author and represents the first time pharmacokinetics of fluorescent contrast agents have been used to discriminate diseased from normal tissue. The work presented in this section culminated in its publication in *Photochemistry and Photobiology*.

---

* Reprinted in part with permission from "Pharmacokinetics of ICG and HPPH-car for the detection of normal and tumor tissue using fluorescence, near-infrared reflectance imaging: a case study," by M. Gurfinkel, A. Thompson, W. Ralston, T. Troy, A. Moore, T. Moore, J. Gust, D. Tatman, J. Reynolds, B. Muggenburg, K. Nikula, R. Pandey, R. Mayer, D. Hawrysz, and E. Sevick-Muraca, 2000. *Photochemistry and Photobiology*, **72**, 94-102.

5.1 Introduction

Numerous investigators have proposed developing non-invasive diagnostic optical approaches to detect cancer and to monitor local photosensitizer concentrations for effective staging of photodynamic therapy (PDT).[58,84-86] Owing to a photosensitizer's near-infrared (NIR) absorption and emission in the therapeutic wavelength regime where light penetrates several centimeters of tissue, it is possible to sense and quantitate photosensitizer concentration in subsurface tissues from measurements of diffuse light propagation.[87-89] Still other investigators propose to use diffuse NIR light to detect and image diseased subsurface tissues based upon spatial variations in NIR absorbance, fluorescence, and fluorescence decay kinetics associated with photodynamic therapy (PDT) and other fluorescent agents (for review the reader is referred to reference [90]). Previous work has demonstrated the use of frequency-domain photon migration (FDPM) with image-intensified CCD detection in order to image *in-vivo* diseased tissues using fluorescent contrast agents.[91] FDPM techniques may offer added imaging advantages in that they enable additional image contrast based upon changing fluorescence decay kinetics of exogenous agents.[14,92] Cubeddu and coworkers have also demonstrated lifetime-based detection of surface lesions using time-domain approaches.[93] The work presented in this section demonstrates the use of image-intensified CCD continuous wave imaging as a function of time (on the order of minutes) to collect fluorescent emissions from photodynamic and fluorescent contrast agents, allowing the subsurface differentiation of normal from diseased tissue volumes based on the pharmacokinetics of the therapeutic or diagnostic agent in question. The results are presented to further

reinforce the potential use of photodynamic agents as optical imaging contrast agents for the detection of subsurface tissues.

In the following sections, the pharmacokinetic models used for modeling the uptake and wash-out of ICG and HPPH-car are presented. The method used to obtain the parameters underlying the pharmacokinetic models from measurements of fluorescent intensity at discrete points on the tissue surface is discussed. The fluorescent agents and animal model employed in the study are described and the image-intensified CCD camera system used to collect fluorescent images of canine mammary tissues is outlined. A statistical comparison of parameter estimates for presumed normal and diseased tissues is provided and compared to pathology. Finally, the maps of pharmacokinetic parameter estimates are provided to differentiate normal from diseased tissues based on the variation in pharmacokinetics.

5.2 Theory

5.2.1 Pharmacokinetics for ICG

Based on experimental measurements, ICG was observed to exhibit rapid wash-in and wash-out, thereby requiring a double-exponential, four-parameter model.

$$I(t) = A\exp(-\alpha t) + B\exp(-\beta t) \tag{5.1}$$

where parameters A, B, α, and β are the pharmacokinetic parameters describing the uptake and release of ICG. To underscore the physical significance of these model parameters, the pharmacokinetic model for the distribution of ICG between blood and tissue is illustrated in Figure 5.1.

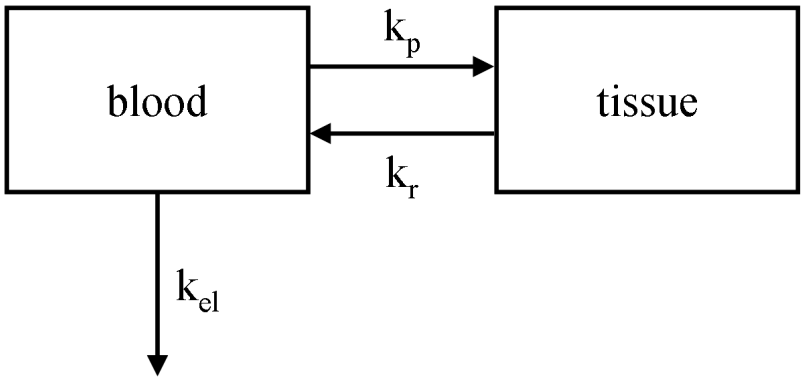

Figure 5.1. ICG pharmacokinetic model.

The concentrations of dye in the blood, C_B, and tissue, C_T, are functions of time, governed by the following system of differential equations:

$$\frac{dC_B}{dt} = -k_B C_B + k_r C_T \,, \tag{5.2}$$

$$\frac{dC_T}{dt} = k_p C_B - k_r C_T \,, \tag{5.3}$$

where $k_B = k_p + k_{el}$, k_p and k_r are first order rate constants that represent the tissue wash-in and wash-out rates, respectively, and k_{el} is the first order rate constant that represents the rate at which dye is removed from the circulation through all other routes. At $t = 0$ (injection time), $C_B = C_{B_o}$ and $C_T = 0$. The solution to this system of differential equations forms the basis of the model.

$$C_B = \frac{C_{Bo}(\alpha - k_r)}{\alpha - \beta}\exp(-\alpha\, t) - \frac{C_{Bo}(\beta - k_r)}{\alpha - \beta}\exp(-\beta\, t), \tag{5.4}$$

$$C_T = \frac{C_{Bo}k_p}{\alpha-\beta}\exp(-\beta t) - \frac{C_{Bo}k_p}{\alpha-\beta}\exp(-\alpha t), \tag{5.5}$$

where α and β are complex rate constants given by:

$$\alpha = \tfrac{1}{2}\left[k_r + k_B + \sqrt{(k_r + k_B)^2 - 4k_r k_{el}}\right] \tag{5.6}$$

$$\beta = \tfrac{1}{2}\left[k_r + k_B - \sqrt{(k_r + k_B)^2 - 4k_r k_{el}}\right]. \tag{5.7}$$

The observed fluorescence intensity, *I(t)*, is a weighted sum of the concentration of contrast agent in the blood and tissue compartments and is represented by:

$$I(t) \cong w_1 C_B + w_2 C_T \tag{5.8}$$

Combining Eqs. (5.4), (5.5), and (5.8) yields:

$$\begin{aligned} I(t) = {} & \frac{C_{Bo}}{\alpha-\beta}\left[w_1(\alpha - k_r) - k_p w_2\right]\exp(-\alpha t) + \\ & \frac{C_{Bo}}{\alpha-\beta}\left[-w_1(\beta - k_r) + k_p w_2\right]\exp(-\beta t) \end{aligned}. \tag{5.9}$$

Comparing Eqs. (5.1) and (5.9) the pharmacokinetic parameters for ICG may be expressed as:

$$A = \frac{C_{Bo}}{\alpha-\beta}\left[w_1(\alpha - k_r) - k_p w_2\right], \tag{5.10}$$

$$B = \frac{C_{Bo}}{\alpha-\beta}\left[-w_1(\beta - k_r) + k_p w_2\right], \tag{5.11}$$

and the complex rate constants α and β which were previously defined in Eqs. (5.6) and (5.7).

Since ICG is a blood pool or blood persistent agent without selective uptake into tumor or other diseased tissues, k_p and k_r should be equivalent for normal and diseased

tissues. Hence, the sum of α and β, or $k_p+k_r+k_{el}$, should also be equivalent for normal and diseased tissues, assuming k_{el}, or the combined liver and kidney ICG uptake rate, is also tissue independent. On the other hand, since vascular density is enhanced in tumor regions, greater ICG fluorescent intensity would be observed in these regions. Therefore, the differentiation of normal from diseased tissues by a blood pool or blood persistent agent results only from variations in microvessel density, not from differences in selective uptake or efflux mechanisms.

5.2.2 Pharmacokinetics for HPPH-car

Unlike ICG, net wash-out of HPPH-car was not observed over the 10-30 min. range of measurements. This observation enabled reduction of the pharmacokinetic model, illustrated in Figure 5.2, to a single exponential, three- parameter model.

$$I(t) = A\exp[-K_B\, t] + B \tag{5.12}$$

where the parameters A and B are given by:

$$A = \frac{C_{Bo}}{k_B}\left(w_1 k_B - w_2 k_p\right), \tag{5.13}$$

$$B = \frac{w_2 k_p C_{Bo}}{k_B}. \tag{5.14}$$

Fitting the HPPH-car fluorescence intensity to a double-exponential model yielded a zero or near-zero coefficient inside the second exponential function reported in Eq. (5.1), thereby supporting the hypothesis that a single-exponential model is applicable for the HPPH-car case. Equations (5.13) and (5.14) were obtained by setting k_r equal to zero in Eqs. (5.10) and (5.11), respectively. Since it is assumed that selective uptake of

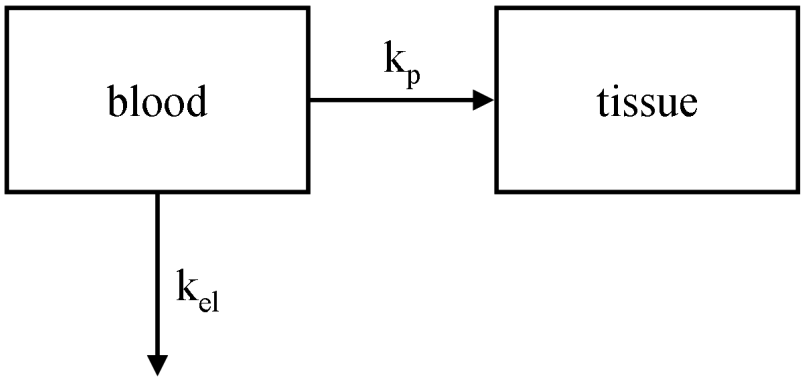

Figure 5.2. HPPH-car pharmacokinetic model.

HPPH-car into the tumor region occurs[94], k_p should be greater in tissue regions associated with disease. Since k_{el}, which describes the clearance of HPPH-car owing to kidney and liver function, is also assumed to be equivalent for normal and diseased tissues, we would expect that mapping k_B would discriminate the adenocarcinoma from normal tissue

Having derived the above models describing the pharmacokinetics of ICG and HPPH-car within tissues, we then fit these models to the temporal variation of fluorescent intensity acquired from the surface of mammary tissues. In addition to the pharmacokinetic parameters, the fitting routine also calculates the sum of the relative error at each pixel point (i, j) to assess the accuracy of the models presented.

$$total\ error\ (i,j) = \sum_t \left| \frac{I_{pred}(t) - I_{obs}(t)}{I_{pred}(t)} \right|_{i,j} . \tag{5.15}$$

5.3 Materials and Methods

5.3.1 Fluorescent Contrast Agents and Animal Model

The work in this section primarily focuses on a pharmacokinetic analysis of dynamic fluorescence data for evaluation of contrast agents and diagnostic imaging. However, for completeness, the salient features of the fluorescent dyes and animal model are discussed herein. For more information about the contrast agents and canine model of spontaneous breast cancer, the reader is referred elsewhere.[95,96] As alluded to earlier, the following work was performed at the Lovelace Respiratory Research Institute, an institute fully accredited by the Association for Assessment and Accreditation of Laboratory Animal Care International, and all studies were performed under the appropriate guidelines.

Two fluorescent dyes were used to detect spontaneous tumors within the canine mammary chain. The first, indocyanine green (ICG) (Cardio-Green, Becton-Dickenson Microbiology Systems, Cockeysville, MD) with excitation and emission peaks near 780-nm and 830-nm, respectively, was reconstituted with sterile water for injection and administered intravenously (i.v.) at 1 mg kg^{-1} body weight. Previously, the extinction coefficient of a micromolar solution of ICG in water at 780-nm was determined to be 130,000-$M^{-1}cm^{-1}$; at 830-nm its fluorescence quantum efficiency and lifetime were found to be 0.016 and 0.56-ns, respectively.[14]

The second fluorescent agent studied was HPPH-car. HPPH-car consists of the photosensitizer HPPH conjugated with a carotene moiety in order to reduce or eliminate phototoxicity for consideration of its potential use as a diagnostic-imaging agent (R.K.

Pandey and A.N. Kozyrev, unpublished). Without the carotene moiety, HPPH is an effective photosensitizer[97,98] and is currently in phase I/II clinical trials at Roswell Park Cancer Institute, Buffalo, NY. It has been previously examined for the fluorescence detection of tumors in hamsters and rats.[99] HPPH-car fluorescence was detected at 710-nm following 660-nm excitation. The extinction coefficient at 664-nm was determined to be 45,000-$M^{-1}cm^{-1}$; its fluorescence quantum efficiency and lifetime were found to be 0.15 and 3.2-ns, respectively.[95] For administration, HPPH-car was formulated in a 1% Tween-80 and 5% dextrose solution and injected i.v. at 0.3 mg kg^{-1}.

The pharmacokinetics of ICG and HPPH-car were studied simultaneously in an 11 year–old female beagle, weighing 4.55 kg and in apparent good health, that presented evidence of palpable mammary masses in the right fourth (R4) mammary gland. For injection of contrast agent and subsequent imaging, the animal was fasted for 18-hr. The animal was placed under general anesthesia, administered an i.v. injection of ICG, and subsequently imaged. The fully recovered animal was then again anesthetized 48-hr after ICG injection for HPPH-car injection and subsequent imaging. At a later date, surgical excision of the mammary tumors was performed for curative reasons and pathologic examination. As described below, the different excitation and emission spectra for the two contrast agents allowed identification of ICG separately from HPPH-car within the tissues.

5.3.2 ICCD Imaging Setup and Instrumentation

Figure 5.3 illustrates the experimental apparatus used to obtain area, fluorescent, DC measurements[59,91,100] from the surface of the canine subject. For front illumination

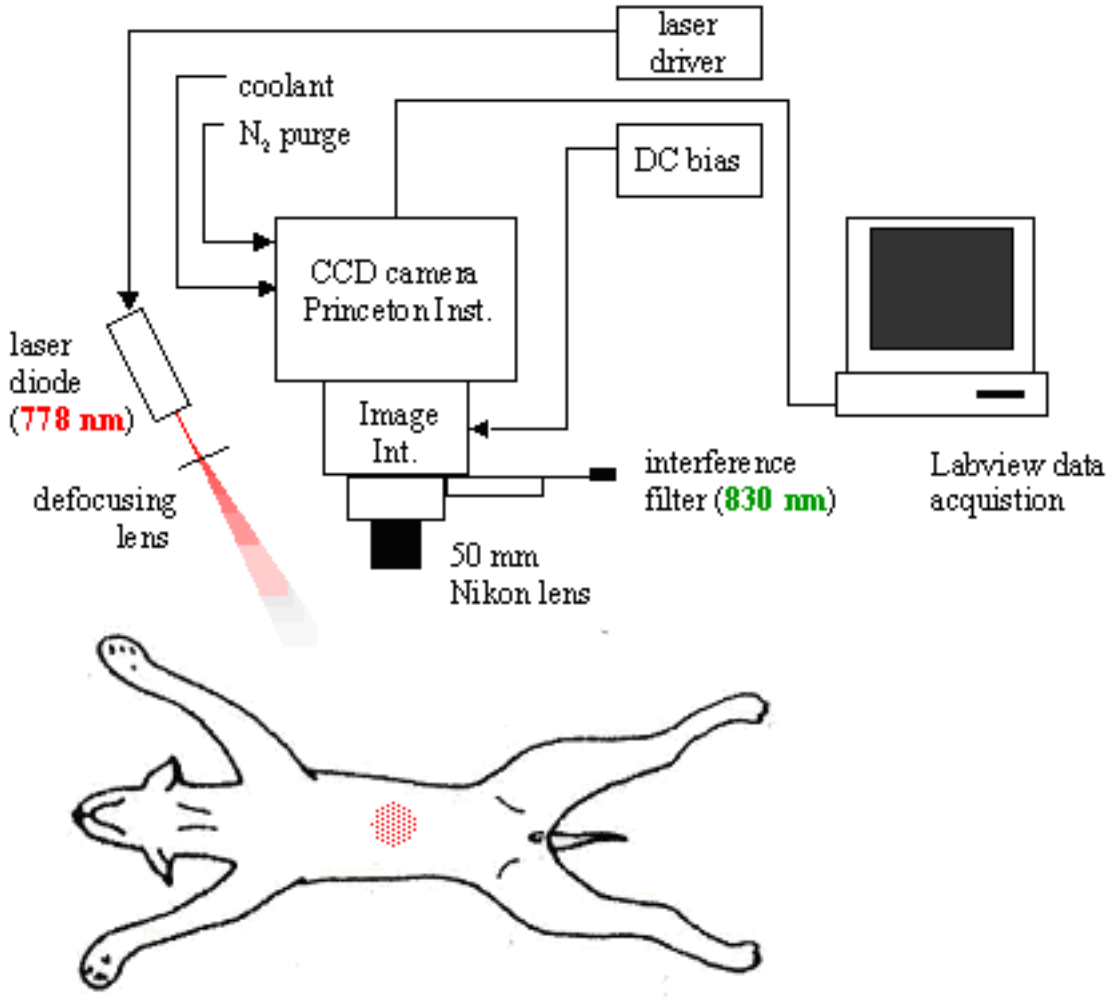

Figure 5.3. Instrumentation for the multipixel imaging device.

geometry, collimated light from a 25-mW, 778-nm laser diode (Melles Griot model 06DLS403, Boulder, CO) or a 100-mW, 660-nm laser diode (Philips Optoelectronics, Eindhoven, Netherlands) is expanded to illuminate a circular area approximately 4-cm in diameter on the surface of a plexiglass plate, which slightly compresses the subject's mammary tissue to minimize motion artifacts and to create a flat imaging surface. A laser diode driver (Melles Griot model 06DLD203, Boulder, CO) maintains the diode at

a constant DC bias and temperature. Located directly above the plexiglass plate, a 50-mm Nikon camera lens and an interference filter combine to focus only diffuse 830-nm (ICG) or 710-nm (HPPH-car) fluorescent light onto the photocathode of an image intensifier (Generation III FS9910C, Roanoke, VA). The 50-nm bandwidth between excitation and detected emission sufficiently prevents leakage of excitation light through the interference filter. A refractive index matching gel couples the image intensifier's phosphor screen to a fiberoptic bundle, which transmits the intensified, diffuse fluorescent image to a 512 × 512 CCD detector array (Princeton Instruments model TE/CCD-512-EFT, Trenton, NJ). To minimize the detection of any inherent dark current, the CCD unit is cooled to −30°C. The multi-pixel imaging device is affixed to a sliding rack assembly that permits three-dimensional movement of the camera over the subject's mammary tissue.

5.3.3 Data Acquisition and Analysis

Directed by a Labview data acquisition program (National Instruments Corp., Austin, TX), the CCD camera acquires ten fluorescent, DC images using an exposure time of 0.2-sec for each image. Subsequently, the program averages these images and stores a binned 128 × 128 intensity array into a data file. Following a 10-sec delay, the program repeats the same data acquisition procedure. Data acquisition continues until the intensity arrays from several successive averaged images are relatively unchanged, indicating the approach of steady state. Following the completion of data acquisition from the canine model, Matlab (The Mathworks, Inc., Natick, MA) further bins the images down to 64 × 64 intensity arrays to expedite the pharmacokinetic analysis. The

images are stored in 64 × 64 × n arrays, where the n^{th} dimension corresponds to the time at which the averaged image was stored.

A Matlab curve fitting routine is then employed to fit the intensity data at each pixel within the three-dimensional array to a kinetic model describing the uptake and release of contrast agent. While the fluorescent intensity at each pixel is proportional to the presence of contrast agent, the intensity is also mediated by tissue optical properties of scattering and absorption. Separate, ongoing research seeks to map the concentration and fluorophore decay kinetics in three-dimensional tissue volumes.[101,102] However, in this study the tissue optical properties are assumed to be relatively constant, so that the temporal fluorescence intensity may be monitored to obtain information regarding dye pharmacokinetics.

5.4 Results and Discussion

The animal model used in this study is the naturally occurring canine mammary tumor. These tumors occur in dogs as they age. The tumors have many characteristics similar to mammary tumors in women. The occurrence of such tumors in bitches in the source colony for this study have been described elsewhere.[96]

Figure 5.4(a) and 5.4(b) illustrate example results from fitting the ICG and HPPH-car pharmacokinetic models, respectively, to time-dependent fluorescent intensity acquired from specific pixels located within the binned 64 x 64 CCD detector array. Figures 5.5 and 5.6 present pharmacokinetic parameter maps for ICG and HPPH-car, respectively, for the entire detector domain, while Figure 5.5 additionally displays a map of $\alpha + \beta$. Both figures also report the sum of the relative error as defined by Eq. (5.15).

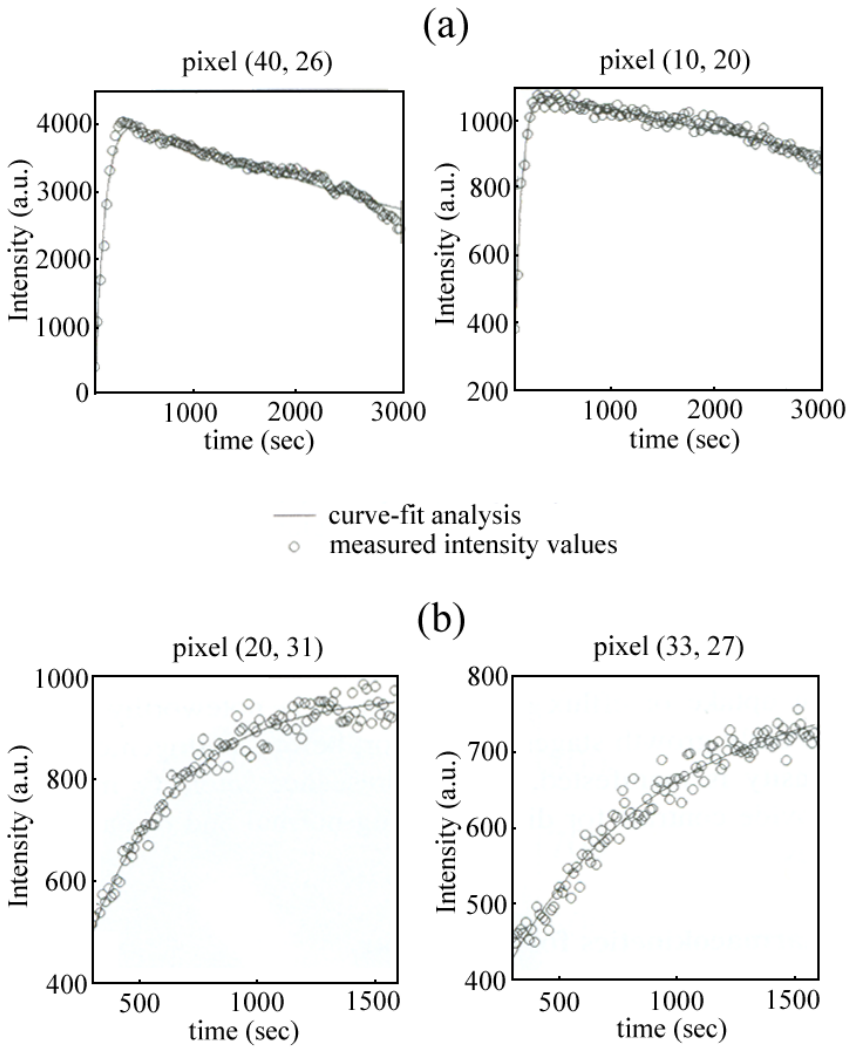

Figure 5.4. Fluorescence intensity as a function of time illustrating typical curve fits using the (a) ICG pharmacokinetics model and (b) HPPH-car pharmacokinetics model.

For ICG pharmacokinetics, the tumor region corresponds to the maximum of the B and β maps, Figures 5.5(b) and 5.5(d), respectively, and the minimum of the A map, Figure 5.9(a). Upon inspection of Eq. (5.1), one observes that it is difficult to relate these parameter estimates to important physiological parameters such as the fraction of

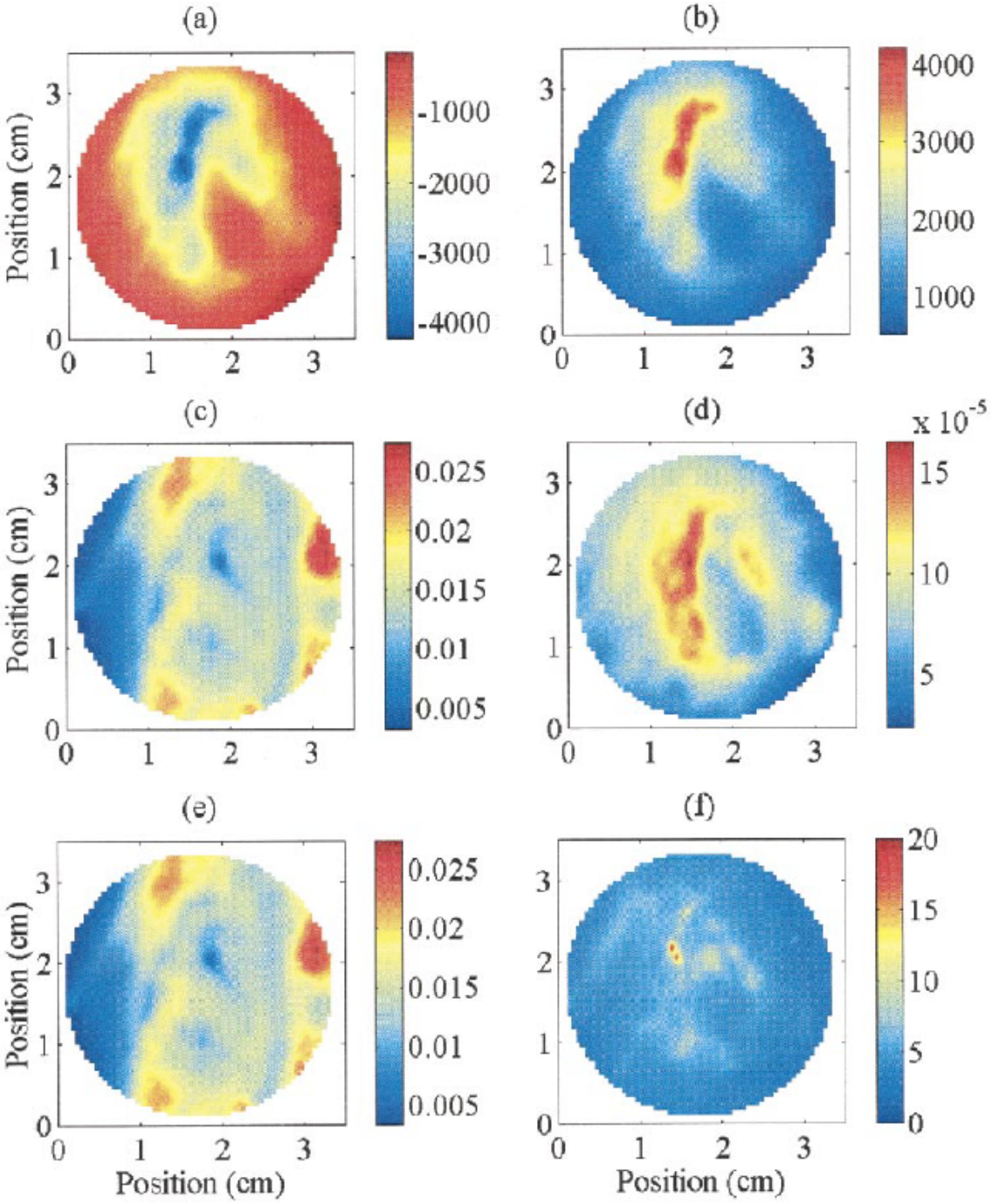

Figure 5.5. ICG pharmacokinetic parameter maps of (a) *A* (a.u.), (b) *B* (a.u.), (c) α (sec^{-1}), (d) β (sec^{-1}), (e) $\alpha + \beta$ (sec^{-1}), and (f) sum of the relative error.

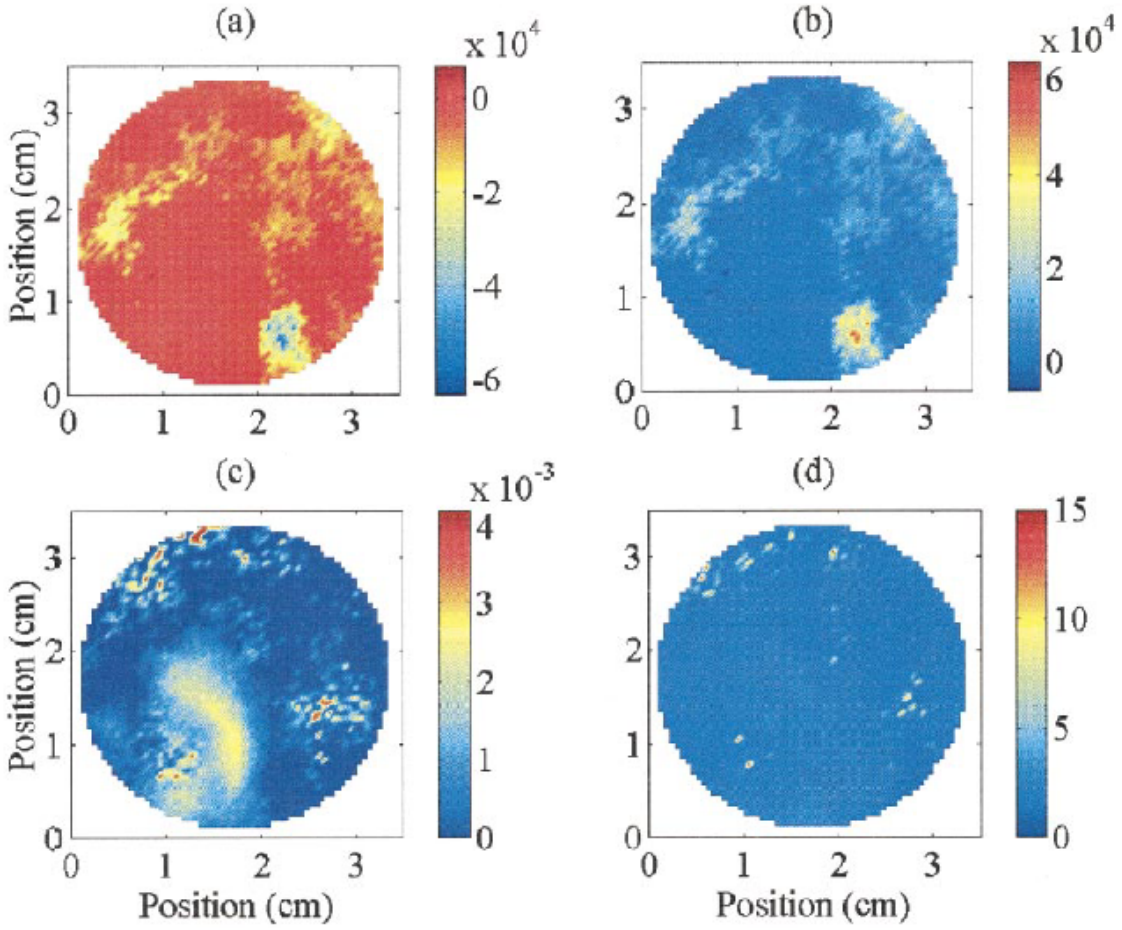

Figure 5.6. HPPH-car pharmacokinetic parameter maps of (a) A (a.u.), (b) B (a.u.), (c) k_B (sec^{-1}), and (d) sum of the relative error.

vascular and extravascular space (w_1 and w_2, respectively) or net uptake of ICG (i.e., k_p and k_r). Nonetheless, these parameter maps could correspond to high vascular volumes associated with disease. As depicted in Figure 5.5(e), the addition of α and β does not seem to differentiate normal tissues from the diseased ones. Since $\alpha + \beta$ relates to the sum of tissue uptake parameters, it is probable that the non-selective, *net* uptake of ICG occurs through equivalent mechanisms in normal and diseased tissues.

Figures 5.6(a) and 5.6(b) do not illustrate any demarcation of the adenocarcinoma from the maps of parameter A and the pre-exponential factor B found in the HPPH-car model. However, Figure 5.6(c) confirms the assumption that the rate constant describing the net uptake of HPPH-car, k_B, does indeed discriminate diseased from normal tissues. The region of increased k_B corresponds to the tissue region containing the adenocarcinoma.

Twenty pixel points, equally distributed between regions that pathology reported to be normal and diseased tissues, were arbitrarily chosen in order to statistically compare the pharmacokinetic parameters for ICG and HPPH-car associated with these tissues. Figures 5.7(a) and 5.7(b) depict the exact location of the pixel points used in these analyses; Tables 5.1 and 5.2 list their pharmacokinetic model parameter estimates.

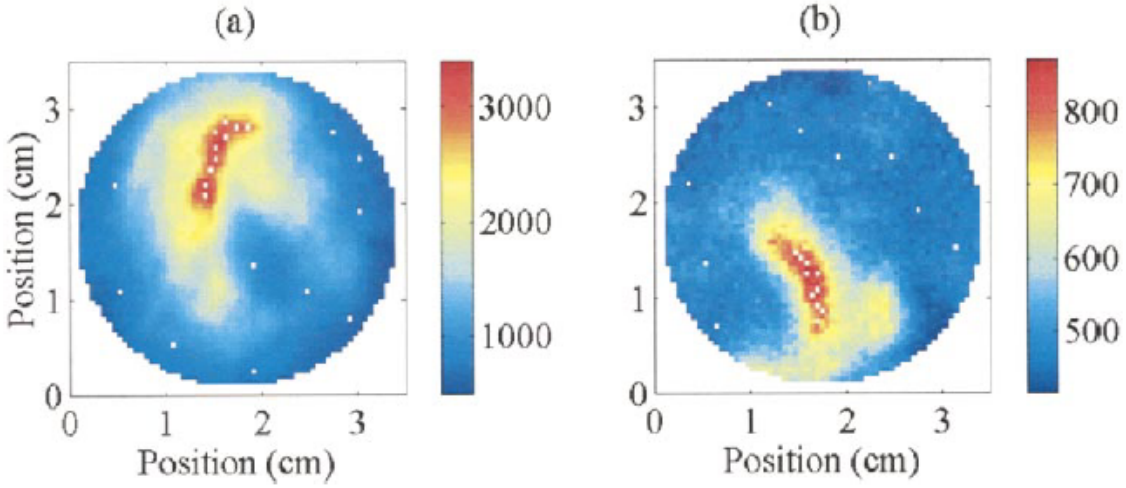

Figure 5.7. Pseudocolor plot of fluorescent DC intensity, midpoint of the data acquisition, denoting the location of pixels used in the statistical analysis for (a) ICG and (b) HPPH-car.

Table 5.1. ICG pharmacokinetic parameter values at designated pixel locations.

pixel	A (a.u.)	B (a.u.)	$\alpha\times10^{2}$ ($\sec^{-1}$)	$\beta\times10^{4}$ ($\sec^{-1}$)	$\alpha+\beta$ ($\sec^{-1}$)
Adenocarcinoma region					
(40,26)	-4226	4214	1.28	1.50	0.0130
(43,27)	-3536	3637	1.41	1.42	0.0142
(47,28)	-3842	3958	1.39	1.33	0.0140
(49,30)	-3582	3699	1.32	1.25	0.0133
(51,32)	-3233	3395	1.32	1.17	0.0133
(45,28)	-3848	3950	1.34	1.42	0.0135
(38,26)	-3812	3913	1.30	1.42	0.0131
(50,28)	-3371	3535	1.67	1.17	0.0168
(51,34)	-3233	3453	1.24	1.17	0.0125
(52,30)	-3347	3501	1.61	1.17	0.0162
mean	-3603	3726	1.39	1.30	0.0140
Presumably normal tissue region					
(10,20)	-771	1098	1.87	0.544	0.0188
(20,45)	-806	1105	1.55	0.744	0.0156
(25,35)	-798	1114	1.47	0.754	0.0148
(40,9)	-826	1158	0.68	0.776	0.0069
(45,55)	-456	830	1.99	0.502	0.0200
(5,35)	-489	862	1.74	0.570	0.0174
(35,55)	-549	910	2.08	0.489	0.0208
(20,10)	-487	874	0.51	0.598	0.0052
(15,53)	-346	736	2.05	0.387	0.0205
(50,50)	-556	938	1.33	0.547	0.0134
mean	-608	962	1.53	0.591	0.0153

Table 5.2 HPPH-car pharmacokinetic parameter values at designated pixel locations.

pixel	A (a.u.)	B (a.u.)	$k_B \times 10^5$ (sec^{-1})
Adenocarcinoma region			
(16,32)	-396	870	268
(20,31)	-467	963	267
(23,31)	-447	912	257
(25,29)	-476	948	248
(27,27)	-431	890	252
(19,30)	-441	931	231
(17,31)	-413	901	229
(26,28)	-450	923	266
(23,29)	-473	955	228
(14,31)	-392	870	228
mean	-439	916	247
Presumably normal tissue region			
(25,10)	-336	772	34.2
(35,50)	-709	1154	3.99
(45,35)	-79	534	47.5
(55,22)	-1993	2440	1.60
(45,45)	-8431	8890	0.389
(40,7)	-9663	10105	0.424
(50,28)	-11352	11795	0.389
(28,57)	-4977	5443	0.389
(13,12)	-1392	1814	5.12
(59,41)	-3856	4327	0.507
mean	-4279	4727	9.45

A Student's t test was performed to determine if $\alpha+\beta$, the sum of parameters found in the ICG pharmacokinetic model, varied significantly between tumor and presumably normal tissue. The 95% confidence limits of $\alpha+\beta$ for these tissues overlapped, indicating no significant difference in net uptake kinetics between the two

tissues. Thus, it may be concluded that it is not possible to discriminate different types of tissue based on the parameter α+β, or the net uptake kinetics of ICG. Similarly, a student's t test was performed on k_B to determine if the pharmacokinetics of HPPH-car can be employed to differentiate normal from diseased tissues. Unlike ICG, the analysis reported at a 95% confidence limit that the values for k_B associated with tumor and presumably normal tissues did not overlap. Thus, it is reasonably assumed that the net uptake kinetics of HPPH-car may indeed be used to demarcate diseased tissues.

The mechanisms that mediate the preferential accumulation of fluorescent dye in neoplastic tissue relative to normal tissue is still not completely understood but may depend on a number of factors including, but not limited to, the nature of the dye itself, the normal tissue being considered, and in the laboratory setting, the animal tumor model being investigated.[94] It is hypothesized that ICG accumulates in regions of tissue possessing leaky vasculature. Although leaky vasculature often accompanies tumor proliferation, accumulation of ICG may not be limited to neoplastic tissue. ICG would also be expected to amass in bruised or injured regions of the tissue volume. On the other hand, HPPH-car is presumed to accumulate in tumor tissue by a different mechanism. HPPH belongs to a group of compounds known as photosensitizers, which are believed to selectively accumulate in tumor tissues. The specificity may be mediated by the dye's association with low-density lipoproteins (LDL) and the upregulation of LDL receptors in tumor cells, which presumably results from an increased rate of cell proliferation or an increased rate of membrane turnover without proliferation.[94] Therefore, it is plausible that, as opposed to ICG, the uptake mechanism of HPPH-car

suggests a more specific interaction; that is, strong HPPH fluorescence should be detected only in regions of the tissue volume where an abundance of cells (presumably malignant cells) overexpressing LDL receptors are present.

5.5 Summary

The work presented in this section demonstrates the use of red-fluorescing dyes to differentiate normal from diseased tissues using simple CW fluorescence intensity imaging and pharmacokinetic analysis. While the excitation and emission spectra of HPPH-car overlap with melanin, perhaps limiting the ability to deliver excitation light and successfully detect propagated fluorescence light at the tissue surface, the dye nonetheless possesses net uptake rates that over the time course of the measurements can be used to differentiate normal from diseased tissues. While ICG has more favorable excitation and emission spectra than HPPH-car, its non-selective net uptake may not be feasible for the detection of disease. Ongoing work seeks to adapt tissue surface fluorescence measurements made with the modulated image-intensified CCD camera described in part herein and elsewhere[91] with mathematical models for determining local dye concentration and fluorescence decay kinetics.[101,102] With the ability to provide time-dependent, three-dimensional mapping of dye concentration, the ability to individually tailor photodynamic therapy for maximal efficiency is promised by this work as well as the work of several other investigators. Upon using PDT agents modified to reduce therapeutic action, diagnostic imaging may be possible. Finally, the ability to determine the *in-vivo* dye fluorescence decay kinetics could aid in the detection

of disease, by providing biochemical specificity as pointed out by Cubeddu and coworkers[93], as well as in determining the potential toxicity of photodynamic agents.

The work presented in this section demonstrates that pharmacokinetic analysis can be a powerful tool for the evaluation of contrast agents, specifically those designed to target molecular markers of disease. Building on the results presented in this section, the following section describes a three-compartmental pharmacokinetic analysis of *in vivo* fluorescence conducted on a murine model of carcinoma to evaluate a novel integrin-targeted fluorescent contrast agent.

6. IMAGING PHARMACOKINETICS OF MOLECULARLYTARGETED DIAGNOSTICS AND THERAPEUTICS: *IN VIVO* PHARMACOKINETICS OF $\alpha_V\beta_3$ INTEGRIN– TARGETED OPTICAL CONTRAST AGENT

Building upon the results of the previous section, the experimental studies described in this section are intended to evaluate the molecular specificity of a molecularly targeted fluorescent dye. As in the previous section, the focus of the work herein is not on the development of the contrast agent itself, but rather on the use of dynamic fluorescence imaging and pharmacokinetic analysis to evaluate the specificity of the integrin-targeted fluorescent contrast agent in an animal model of carcinoma. Again, the work was performed as a collaborative effort, with the experimental studies conducted at the University of Texas M.D. Anderson Cancer Center (MDACC) in Houston. Collaborators at MDACC, recognized in the Acknowledgements section in the preface of this dissertation, were responsible for the synthesis of the contrast agents and the preparation of the animal models of carcinoma. Therefore, the experimental aspects related to the contrast agents and animal models are discussed only briefly for completeness.

6.1 Introduction

The targeted delivery of therapeutic agents represents a novel approach in the treatment of cancer. Unlike conventional treatment strategies such as chemotherapy and radiation therapy, targeted therapies are designed to treat and kill only the affected cancerous cells, thereby reducing toxicity to normal, non-cancerous cells.

In the past several years, a number of targeted cancer drugs have shown tremendous promise and a select few have been approved by the Food and Drug Administration (FDA). These cancer drugs generally target and inhibit signal transduction that would otherwise lead to the proliferation, differentiation, or anti-apoptosis of the cancer cells. The drug is often targeted to an extracellular membrane bound receptor or to an intracellular protein critical to the signaling pathway, resulting in the interruption of the downstream signaling cascade.[103] Herceptin®, developed by Genentech, Inc. and approved by the FDA in 1998, exerts its therapeutic effects on metastatic breast cancer cells that overexpress the HER-2 receptor.[103-105] Similarly, Erbitux®, developed by ImClone Systems Inc., targets the extracellular membrane-bound epidermal growth factor receptor, commonly overexpressed in many types of cancer.[104,105] More recently, the protein-tyrosine kinase Bcr-Abl, whose elevated activity is strongly implicated in the mechanism of development of chronic myeloid leukemia, has been the molecular target of a therapeutic drug.[106] The drug, Gleevec®, marketed by Novartis Pharmaceutical Corporation in 2001, competitively binds the ATP binding site on the enzyme, and suppresses the proliferation of Bcr-Abl-expressing cells.[103-106]

Integrins, a group of transmembrane glycoproteins that bind cells to the extracellular matrix, constitute another family of cell surface receptors that represent a possible target for site-specific drug delivery. Given that many of the extracellular proteins recognized and bound by integrins share the amino acid sequence arginine-glycine-aspartic acid (RGD) and integrins are often overexpressed on actively

proliferating endothelium as compared to quiescent endothelium cells, RGD tags could serve to deliver therapeutic agents to highly angiogenic sites. Schiffelers *et al.* recently demonstrated the use of an RGD-peptide conjugated to a liposome encapsulating the drug doxorubicin to target the $\alpha_v\beta_3$ integrin and inhibit tumor growth in a murine colon carcinoma model.[107] Although it is unlikely that the targeted treatment of cancer will find the widespread applications of conventional approaches in the all too near-future, targeted therapy marks a significant advance in the drive towards patient-specific cancer treatment regimens.

In addition to targeting therapeutic agents, researchers have exploited tumor-specific molecular targets for purposes of imaging. Both nuclear[108,109] and optical imaging[21,22,24,30,110] techniques have exploited receptor overexpression to visualize tumors. Furthermore, Weissleder and colleagues demonstrated the use of optical imaging to visualize tumors following the enzyme specific activation of a near-infrared fluorescent probe.[33] Relative to nuclear imaging, optical imaging requires the administration of ultra-low concentrations of diagnostic agent. This fact, combined with the ability to acquire rapid dynamic optical images, enables optical imaging to serve as a diagnostic tool for the evaluation of pharmacokinetic properties of agents targeted towards molecular markers of disease.

Because targeted therapies are beneficial to select patient populations, the need for a diagnostic tool capable of assessing expression levels of target receptors and providing exclusion criteria precedes the successful implementation of this paradigm. To this end, the use of *in vivo* pharmacokinetic analyses to evaluate the specificity of a

targeted diagnostic agent is demonstrated, from which one may infer receptor-ligand affinity, receptor expression levels, and receptor turnover rate. The diagnostic agent, a conjugate of RGD peptide and a fluorescing cyanine dye, RGD-Cy5.5, is targeted to the $\alpha_v\beta_3$ integrin overexpressed on xenografted tumors in a murine model of human Kaposi's sarcoma, KS1767.

6.2 Theory

In this section a pharmacokinetic model is developed in order to describe the time-dependent distribution of the fluorescing dye-peptide conjugate throughout the animal. The model, depicted schematically in Figure 6.1, is comprised of three compartments: the blood plasma compartment, the extravascular, extracellular compartment, and the cellular compartment.

The dye is administered rapidly into the blood plasma compartment via an intravenous bolus injection. From this central blood compartment, the dye diffuses across the vascular endothelium and partitions into the extravascular, extracellular space

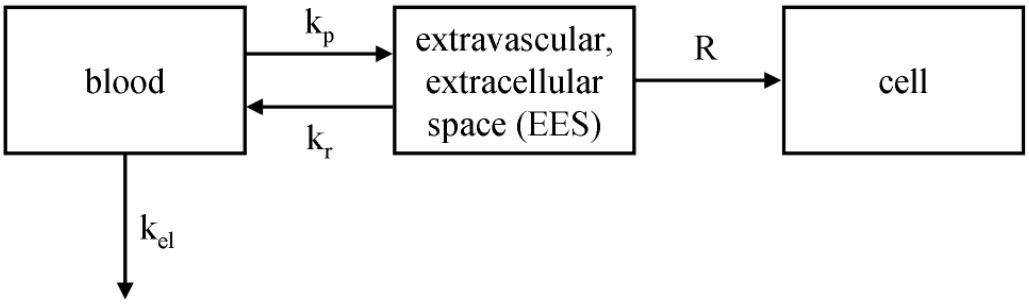

Figure 6.1. Schematic depicting the three-compartment pharmacokinetic model.

(EES) represented by the second compartment. The endothelial transfer coefficient or the rate constant for the distribution of dye from the blood to the EES is given by k_p while k_r is the rate constant describing the reflux from the EES to the blood. A measure of vascular permeability can be obtained from an analysis conducted on first pass circulation data, or data obtained immediately following the bolus injection of the agent. Cuccia *et al.* employed a pharmacokinetic analysis to quantify physiologic parameters related to capillary permeability following the administration of the non-specific dye indocyanine green.[111]

In addition to extravasation into the EES, the dye is eliminated from the blood compartment via other routes such as kidney filtration and liver metabolism, described collectively by the rate constant k_{el}. For non-specific dyes, that is, dyes that do not exhibit cellular specificity, the blood and EES compartments may be sufficient to describe their distribution.[95] However, for dyes that exhibit molecular specificity, a third compartment is included. This third compartment represents the association of the dye at a molecular level, whether it is through surface receptor binding or cellular uptake. The rate at which the dye accumulates in the cellular compartment, whether through association with cellular membrane receptors or internalization, is denoted by R.

If the rate of accumulation of dye in the cellular compartment, R, is constant, determining the time-dependent dye concentration in each of the compartments is relatively straightforward. However, in general, the association between the dye and the cell is a saturable process. Therefore, the rate of dye uptake by the cell may be expressed as:

$$R = \frac{V_m C_{EES}}{K_m + C_{EES}}, \tag{6.1}$$

where, C_{EES} is the concentration of the dye in the EES, V_m is the maximum rate of dye internalization or receptor association at the cellular compartment and K_m is known as the Michaelis constant and is equivalent to the dye concentration at which the rate of uptake is equivalent to one-half the maximum rate.[112] Eq. (6.1) is a form of the Michaelis-Menten expression for a saturable reaction based on a single substrate mechanism.[112] Using Eq. (6.1) to express the rate of distribution of the dye to the cellular compartment leads to nonlinear pharmacokinetics and considerably complicates the mathematics of the model. Fortunately, at low dye concentrations, where C_{EES} is much smaller than K_m, Eq. (6.1) reduces to:

$$R = \frac{V_m}{K_m} C_{EES} = k_c C_{EES}, \tag{6.2}$$

where V_m/K_m can be expressed as an apparent first-order rate constant, k_c, that describes the distribution of dye between the EES and cellular compartments. Furthermore, the distribution of dye from the EES to the cellular compartment is assumed to be a one-way process. That is, cellular uptake is considered irreversible and dissociation of the receptor-dye complex is assumed to occur at a rate much slower than the rate of association. Therefore, the rate constant for the reflux from the cell to the EES compartment is assumed to be negligible. Applying this approximation, the diminution and accumulation of dye in each of the three compartments can be expressed as:

$$\frac{dC_B}{dt} = -\left(k_p + k_{el}\right) C_B + k_r C_{EES} = -k_B C_B + k_r C_{EES}, \tag{6.3}$$

$$\frac{dC_{EES}}{dt} = k_p C_B - (k_r + k_c) C_{EES} = k_p C_B - k_{EES} C_{EES}, \tag{6.4}$$

$$\frac{dC_c}{dt} = k_c C_{EES}, \tag{6.5}$$

where $k_B = k_p + k_{el}$, $k_{EES} = k_r + k_c$, t is time, and C_B, and C_C represent the concentration of dye in the blood and the cell, respectively.

The detected fluorescence intensity at the tissue surface is mediated by a number of factors including the tissue optical properties of scattering and absorption and the depth and concentration of the embedded fluorophore within the tissue. For purposes of monitoring the temporal fluorescence intensity the optical properties of the tissue are assumed to be constant so that the detected fluorescence intensity may be expressed as a weighted sum of the concentration of the dye in each compartment:

$$I(t) \cong w_1 C_B + w_2 C_{EES} + w_3 C_C, \tag{6.6}$$

where $I(t)$ is the time-dependent fluorescence intensity and w_1 , w_2 , and w_3 are weighting functions that represent the volume fraction of the blood, EES, and the cellular compartments, respectively. Additionally, the weighting functions account for the attenuation that occurs as the fluorescent light traverses each compartment.

To obtain the time-dependent dye concentration in each of the compartments, the system of differential equations given by Eqs. (6.3), (6.4) and (6.5) may be solved simultaneously subject to the initial condition that at the time of i.v. bolus injection of the dye, $t = 0$, $C_B = C_{Bo}$, $C_{EES} = 0$, and $C_c = 0$ (see Appendix B). The results may

then be applied to Eq. (6.6) to obtain the following expression for the time-dependent observed fluorescence intensity:

$$I(t) = I_o + A[1 - \exp(-\alpha t)] + B[1 - \exp(-\beta t)] \tag{6.7}$$

where

$$I_o = w_1 C_{Bo}, \tag{6.8}$$

$$A = \frac{C_{Bo}}{\alpha - \beta}\left[k_p w_2 - (\alpha - k_{EES}) w_1 - \frac{k_c k_p w_3}{\alpha}\right], \tag{6.9}$$

$$B = \frac{C_{Bo}}{\alpha - \beta}\left[(\beta - k_{EES}) w_1 - k_p w_2 + \frac{k_c k_p w_3}{\beta}\right], \tag{610}$$

and α and β are complex rate constants given by

$$\alpha = \tfrac{1}{2}\left[k_{EES} + k_B + \sqrt{(k_{EES} - k_B)^2 + 4k_r k_p}\right], \tag{6.11}$$

$$\beta = \tfrac{1}{2}\left[k_{EES} + k_B - \sqrt{(k_{EES} - k_B)^2 + 4k_r k_p}\right]. \tag{6.12}$$

The pre-exponential factors *A* and *B* are concentration terms that mathematically reflect the magnitude of the detected signal. Upon inspection of Eqs. (6.9) and (6.10) one observes that it is difficult to relate these parameters to physiologically relevant indications of disease such as the volume fractions of vascular and extravascular space or the rate constants governing dye uptake. Nonetheless, these parameters may reflect high vascular volumes associated with diseases.[95]

An examination of Eq. (6.11) and (6.12) reveals that the complex rate constant α must be greater than β. As a result, at early time points the expression for the observed fluorescence intensity is more strongly influenced by the term containing α. However,

the exponential term containing α approaches zero more rapidly than does the term containing β. Consequently, at later time points the expression for the observed fluorescence intensity becomes a function of β alone. Therefore, the early time portion of the fluorescence intensity profile is referred to as the α phase whereas the later portion is known as the β phase.

Furthermore, it is evident that the values of α and β are intimately related to the values of all other rate constants. It is particularly interesting to examine how α and β vary with the magnitude of the elimination rate constant, k_{el}. For example, if the value of k_{el} is varied while all other rate constants remained fixed, the root function that appears in the expression for both α and β would asymptotically approach $k_B - k_{EES}$ for large values of k_{el} and $k_{EES} - k_B$ for small values. As a result, α approaches k_B while β approaches k_{EES} when the intrinsic elimination is very rapid. The trend is reversed when elimination is slow; α approaches k_{EES} while β approaches k_B. Finally, because α and β differ by only the sign in front of the root function, the sum of α and β yields the sum of all rate constants between the various compartments of the model, $\alpha + \beta = k_{el} + k_p + k_r + k_c$. One may exploit this result to determine the magnitude of the rate constant for specific uptake of contrast agent within the cellular compartment, k_c as follows: for a given specific contrast agent administered in an animal bearing a tumor model in which the specific cellular uptake mechanism has been compromised while the remaining mechanisms of dye uptake remain unchanged, the net decrease in $\alpha + \beta$

reflects the magnitude of the rate constant for specific cellular uptake of the contrast agent.

As a final note, from Eq. (6.7) it is evident that I_o represents the fluorescence intensity at the time of contrast agent administration or background fluorescence intensity level. Thus, when one applies a background subtraction technique, the mathematical equivalent of setting I_o equal to zero, the number of parameters to be fit is reduced such that the time-dependent observed fluorescence intensity may be expressed as:

$$I(t) = A\left[1 - \exp(-\alpha t)\right] + B\left[1 - \exp(-\beta t)\right], \tag{6.13}$$

where the pharmacokinetic parameters A, B, α, and β were previously defined in Eqs. (6.9), (6.10), (6.11), and (6.12). Given time-dependent observations of fluorescence intensity, Eq. (6.13) may be employed in a regression algorithm to obtain estimates of the pharmacokinetic parameters A, B, α, and β.

6.3 Materials and Methods

6.3.1 Fluorescent Dyes and Animal Model

The monofunctional hydroxysuccinimide ester of Cy5.5 dye (Cy5.5-NHS, MW 1kD) was purchased from Amersham Biosciences (Piscataway, NJ) and conjugated to RGD peptide in-house at the M.D. Anderson Cancer Center by Dr. Wei Wang. The free Cy5.5 dye was used as is after dilution in saline.

For the preparation of the animal models, four to six week-old female athymic nude mice (nu/nu; 18 –22 g) were purchased from Harlan Sprague Dawley, Inc.

(Indianapolis, IN). Animals were maintained in a specific pathogen-free mouse colony in the Department of Veterinary Medicine (The University of Texas M. D. Anderson Cancer Center, Houston, TX). The facility is accredited by the American Association for Laboratory Animal Care and all experiments were performed in accordance with the guidelines of the Institutional Animal Care and Use Committee.

Human Kaposi's sarcoma KS1767 tumor cells were implanted subcutaneously into the thigh region of mice. All the tumor cell work, including preparation of the animal models, was performed by collaborators, primarily Dr. Shi Ke and Dr. QingPing Wu. Mice were imaged when the tumor size reached approximately 2-mm in diameter.

Animals were subdivided into four test groups based on the contrast agent administered. Animals in the first group received the free Cy5.5 dye, while animals in the remaining three groups were administered the RGD-Cy5.5 conjugate. Of those animals receiving the conjugate dye, one-third received the conjugate dye alone; one-third received the conjugate one hour after the intravenous injection of RGD peptide; and the remaining third received the conjugate 24-hrs after the intravenous injection of the RGD peptide.

6.3.2 Instrumentation

Excitation light provided by a laser diode (660-nm, 35-mW; Sanyo, model, Allendale, NJ) was expanded via a plano-convex lens (ThorLabs, model , Newton, NJ) and a holographic diffuser (Edmund Industrial Optics, model NT54-494, Barrington, NJ) to provide a uniform excitation field of approximately 12-cm in diameter over the surface of the animal. A laser diode driver (ThorLabs, model LDC500, Newton, NJ) provided

the diode with 60-mA of dc current while a temperature controller (ThorLabs, model TEC2000, Newton, NJ) helped maintain a constant lasing wavelength.

An intensified charge-coupled device (ICCD), comprised of a 16-bit CCD camera (Photometrics, model CH350/L, Tucson, AZ) coupled to an image intensifier (model FS9910C, ITT Night Vision, Roanoke, VA) via a 105-mm lens, functioned as an area detector of re-emitted fluorescence light. A whole-body fluorescence image of the animal, approximately 12-cm in diameter, was focused onto the photocathode of the image intensifier with a 50-mm lens. A holographic notch-plus band rejection filter (660-nm center wavelength; Kaiser Optical Systems, Inc., Ann Arbor, MI) and a bandpass filter (710-nm center wavelength; CVI Laser, Albuquerque, NM) were positioned prior to the 50-mm lens to reject backscattered and reflected excitation light and isolate only re-emitted fluorescence light. For the acquisition of white-light images, a low-power lamp provided a white-light source and the filters were removed. Image acquisition was controlled by a personal computer equipped with V++ imaging software (Digital Optics, Auckland, New Zealand). A schematic of the instrumentation is provided in Figure 6.2.

6.3.3 Experimental Method

Prior to the onset of the fluorescence imaging procedure, mice were anesthetized by intraperitoneal injection of 50-mg (kg bw)$^{-1}$ Nembutal (Sigma, St. Louis, MO) and a catheter was positioned into the tail vein to facilitate the subsequent delivery of the fluorescent dye. The anesthetized mouse was then positioned beneath the imaging system and image acquisition commenced. Fluorescence images were obtained every

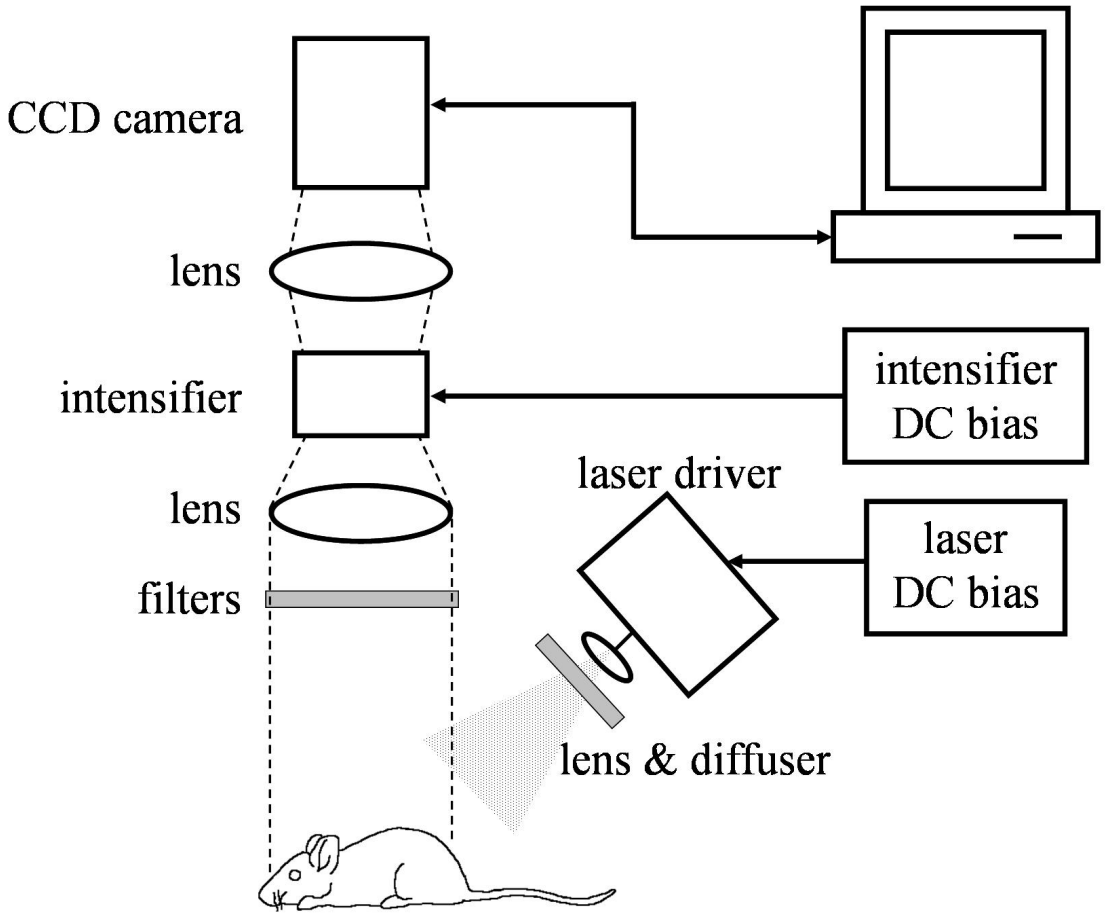

Figure 6.2. Instrumentation for the intensified charge-coupled device (ICCD) small animal imaging system.

seven seconds for a period of approximately 18-minutes following the injection of contrast agent. The first five images were acquired prior to the bolus administration of the fluorescent probe, and thus, served as baseline or background images. The injected dose of RGD-Cy5.5 and the image exposure time were equivalent to 3-nmol (in 0.3-ml volume) and 800-msec, respectively, and were constant for all the imaging studies conducted. Fluorescence images were obtained at 24-hrs post initial injection and again

every 24-hrs thereafter until little or no fluorescence signal was detectable from the tumor region of interest, as determined qualitatively, for up to 168-hrs.

6.3.4 Data Analysis

Upon completion of the imaging routine, a background image was subtracted from each of the acquired fluorescence images. The white light image was then used to define two regions of interest (ROI); one was located entirely within the circumference of the tumor and the other, approximately equivalent in size, defined a region of normal tissue located symmetrically opposite the tumor site. Utilizing Matlab software (The MathWorks, Inc., Natick, MA) the mean of the fluorescence intensity within each ROI was computed for every fluorescence image acquired. Using this data, curves of mean fluorescence intensity versus time were then generated for each of the imaging studies performed. The analytical expression for time -dependent fluorescence intensity, Eq. (6.13), was then fitted to the observed mean fluorescence intensity versus time data via a nonlinear Levenberg-Marquardt regression algorithm available in the SigmaPlot software package (SPSS Inc., Chicago, IL). Estimates of the pharmacokinetic parameters A, B, α, and β were obtained from the analysis for each curve.

6.4 Results and Discussion

The pharmacokinetic parameters A, B, α, and β were obtained from the nonlinear least squares analysis of the time-dependent fluorescence intensity data. Figure 6.3 displays the results of the regression in a plot of the fluorescence intensity profile and the corresponding least-squares fit obtained from one representative animal of each of the

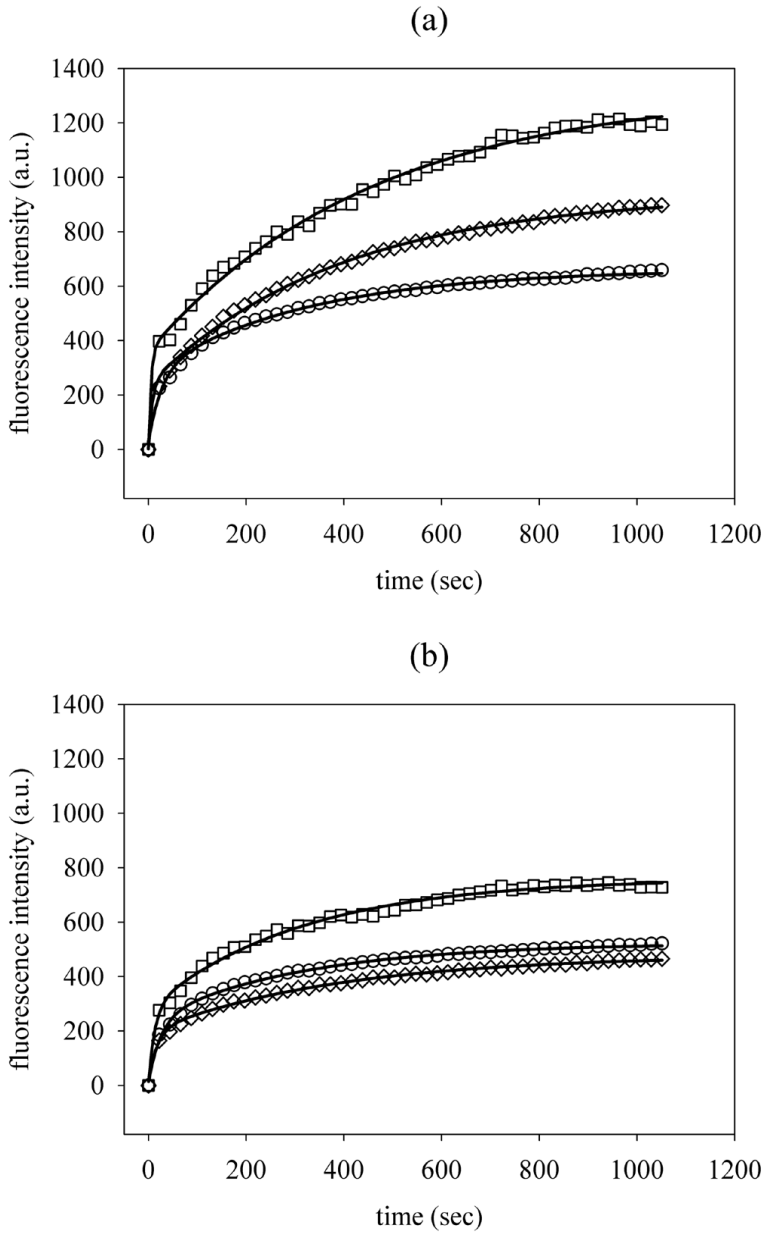

Figure 6.3. Fluorescence intensity versus time profiles obtained from one representative animal of each of the groups that received an injection of the RDG-Cy5.5 conjugate, acquired from the (a) tumor ROI and (b) normal ROI. The symbols denote experimental measurements while the solid line denotes the corresponding least-squares fit. The squares (□) denote data from an animal receiving the RGD-Cy5.5 conjugate alone, while the circles (○) and diamonds (◊) represent data obtained from an animal receiving the conjugate one hour and 24-hours, respectively, after the injection of RGD peptide.

groups that received an injection of the RDG-Cy5.5 conjugate. Table 6.1 summarizes the results of such an analysis preformed on all experimental data obtained: two regions of interest (normal and tumor) investigated per each animal in one of four test groups as outlined in Section 6.3.2. Table 6.1 reports estimates for the pharmacokinetic parameters A, B, α, and β and the value of $\alpha + \beta$ with a 95% confidence interval on the estimate. The coefficient of determination R^2 for the regression was 0.99 or greater in all cases.

Furthermore, the mean value of the pre-exponential parameters A and B obtained from each of the test groups of animals investigated is presented in Figure 6.4. An examination of Figure 6.4 reveals that for the same type of ROI under investigation, the pre-exponential pharmacokinetic parameters A and B agree considerably well among animals that were injected with the RDG-Cy5.5 conjugate, while they are significantly lower for animals receiving the free Cy5.5 dye. As discussed in Section 6.2 the pre-exponential factors A and B reflect the magnitude of the detected signal and thus, are not only subject to the concentration of injected fluorophore but also will vary with experimental conditions such as detector sensitivity and excitation light fluence. Thus, the fact that A and B are significantly different for animals that received the free Cy5.5 dye reflects the differences in signal intensities arising from the use of a different contrast agent, and may not truly reflect differences in pharmacokinetics. On the other hand, because the exponential factors α and β are dictated by the shape of the fluorescence intensity profile rather than the magnitude of detected signal, they may be directly comparable between different experimental trials utilizing the same or different

Table 6.1. Results of the nonlinear regression of observed fluorescence intensity versus time data. The pharmacokinetic parameters, as defined by Eq. (6.13), are reported with a 95% confidence interval on the estimate. The table lists the results of data obtained from the distinct ROIs containing normal and tumor tissue for each of the four test groups investigated, as outlined in Section 6.3.1.

ROI	contrast agent	animal	A (a.u.)	B (a.u.)	$\alpha \times 10^{1}$ (s^{-1})	$\beta \times 10^{3}$ (sec^{-1})	$\alpha + \beta$ (sec^{-1})
normal	Cy5.5	097	14 ± 3	27 ± 4	0.35 ± 0.08	2.2 ± 0.4	0.037 ± 0.008
		099	13 ± 2	26 ± 2	0.58 ± 0.09	1.9 ± 0.4	0.060 ± 0.009
	RGD-Cy5.5	355	245 ± 18	496 ± 7	0.63 ± 0.09	2.7 ± 0.2	0.066 ± 0.009
		357	266 ± 26	479 ± 11	0.75 ± 0.09	3.2 ± 0.2	0.078 ± 0.009
		358	227 ± 13	320 ± 9	0.59 ± 0.07	1.7 ± 0.2	0.061 ± 0.007
	RGD-Cy5.5 1-hr after RGD	356	228 ± 16	408 ± 6	0.66 ± 0.09	2.5 ± 0.2	0.069 ± 0.009
		359	225 ± 12	284 ± 7	0.40 ± 0.04	3.2 ± 0.2	0.043 ± 0.009
		360	258 ± 19	346 ± 8	0.97 ± 0.09	3.3 ± 0.2	0.100 ± 0.009
	RGD-Cy5.5 24-hr after RGD	093	182 ± 11	282 ± 4	0.58 ± 0.07	2.6 ± 0.2	0.061 ± 0.007
		094	135 ± 7	411 ± 3	1.0 ± 0.1	2.2 ± 0.1	0.10 ± 0.01
tumor	Cy5.5	097	13 ± 3	27 ± 2	0.58 ± 0.04	1.9 ± 0.4	0.060 ± 0.004
		099	15 ± 2	31 ± 2	0.57 ± 0.08	1.7 ± 0.2	0.059 ± 0.008
	RGD-Cy5.5	355	355 ± 32	669 ± 11	2.5 ± 0.7	3.9 ± 0.2	0.25 ± 0.07
		357	356 ± 40	961 ± 15	2.1 ± 0.7	2.2 ± 0.2	0.21 ± 0.07
		358	374 ± 45	651 ± 15	1.6 ± 0.4	2.7 ± 0.2	0.16 ± 0.04
	RGD-Cy5.5 1-hr after RGD	356	277 ± 48	475 ± 33	0.16 ± 0.04	2.3 ± 0.4	0.018 ± 0.004
		359	254 ± 16	379 ± 10	0.38 ± 0.05	3.1 ± 0.2	0.041 ± 0.005
		360	241 ± 22	442 ± 9	0.75 ± 0.08	3.3 ± 0.2	0.078 ± 0.008
	RGD-Cy5.5 24-hr after RGD	093	231 ± 20	699 ± 7	1.5 ± 0.3	2.6 ± 0.1	0.15 ± 0.03
		094	169 ± 14	823 ± 22	1.9 ± 0.4	1.2 ± 0.1	0.19 ± 0.04

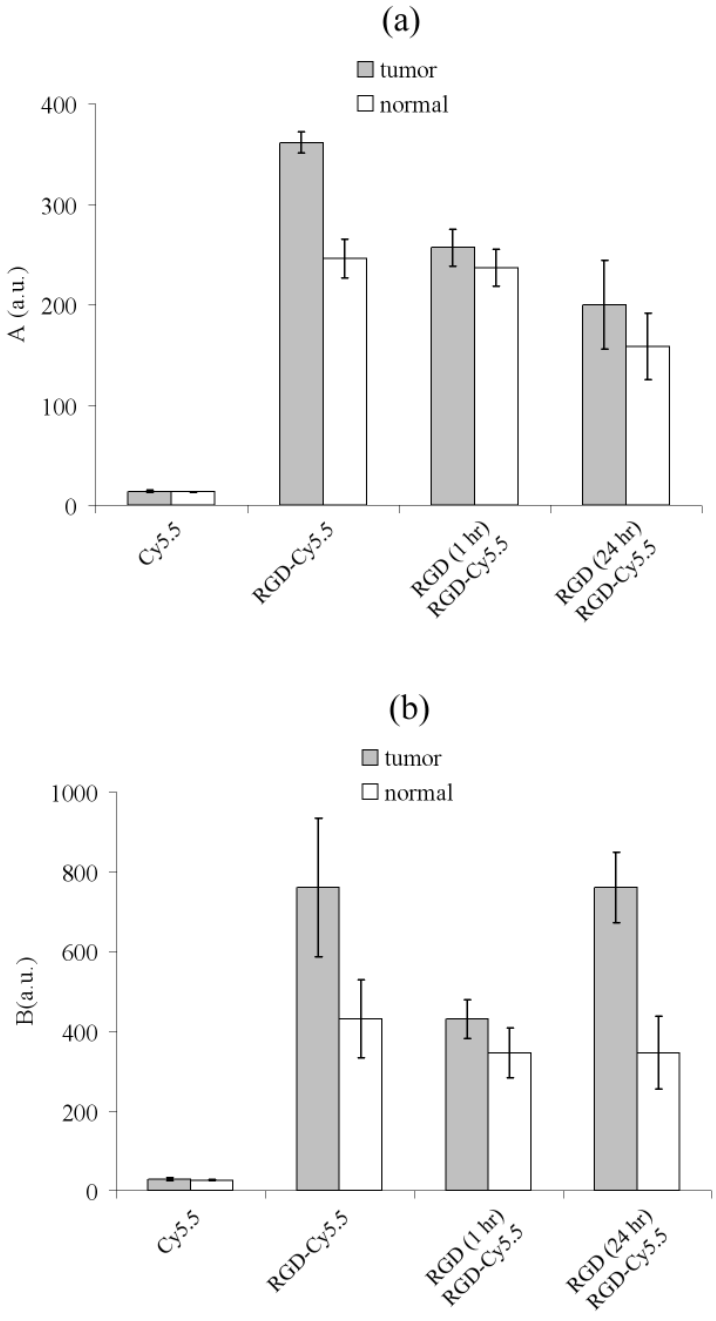

Figure 6.4. Results of the non-linear least squares regression in determining the pharmacokinetic pre-exponential factors (a) *A* and (b) *B*. The column height represents the mean value of the test group listed along the abscissa while the error bars represent the standard deviation. The time in parenthesis represents the time between injection of the RGD peptide and the RGD-Cy5.5 conjugate.

contrast agents. For this reason, the remainder of the discussion shall focus on the differences among the intensity-independent parameters α and β.

As is evidenced from Figures 6.5 and 6.6, the pharmacokinetic parameters α and β and the sum $\alpha + \beta$ do not appear to differ between the normal ROIs of all animal groups studied; a series of homoscedastic pooled *t*-tests confirmed that the mean estimates of α, β, and $\alpha + \beta$ are not significantly different, at a 95% significance level, among the various groups of animals investigate. Furthermore, statistical analysis confirms no variance in the parameter β, with a 95% level of significance, among data obtained from the tumor ROIs of the various groups of animals studied. However, the parameter α and the deviates among data obtained from the tumor ROIs of the various animal groups studied. For animals injected with free Cy5.5 and animals pretreated with RGD peptide one hour prior to the injection of the RGD-Cy5.5 conjugate the value of α averaged 0.058-sec^{-1} and 0.043-sec^{-1}, respectively; values that are statistically similar at 95% level of significance to each other and to the mean values of α determined from the normal ROIs. Similar trends are observed for the sum $\alpha + \beta$. These results suggest that the free Cy5.5 dye exhibits similar pharmacokinetics in Kaposi's sarcoma tumor tissue and in normal tissue. Likewise, the conjugate RGD-Cy5.5 dye exhibits similar pharmacokinetics in tumor and normal tissue when the administration of the dye is preceded by the injection of RGD peptide by one hour.

On the other hand, the parameter α averages 0.21-sec^{-1} and 0.17-sec^{-1} for data obtained from the tumor ROIs in animals that received the RGD-Cy5.5 conjugate alone

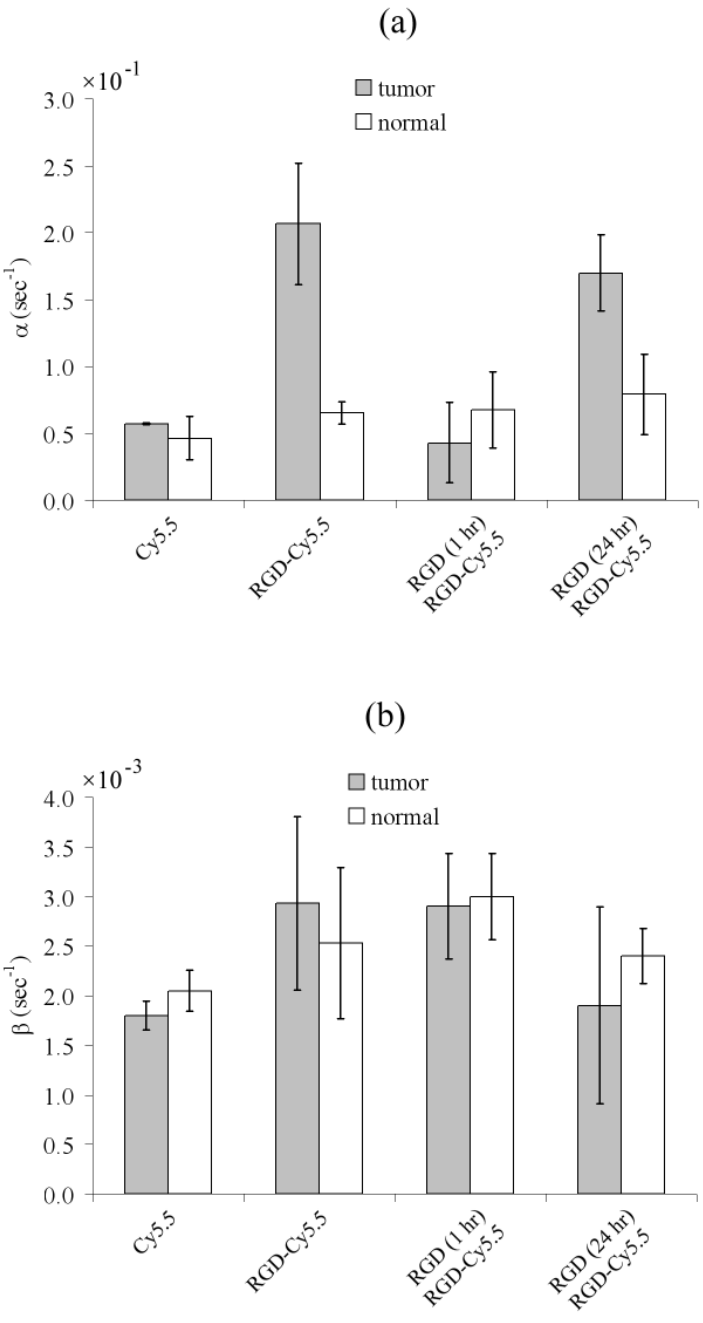

Figure 6.5. Results of the non-linear least squares regression in determining the pharmacokinetic complex rate constants (a) α and (b) β. The column height represents the mean value of the test group listed along the abscissa while the error bars represent the standard deviation. The time in parenthesis represents the time between injection of the RGD peptide and the RGD-Cy5.5 conjugate.

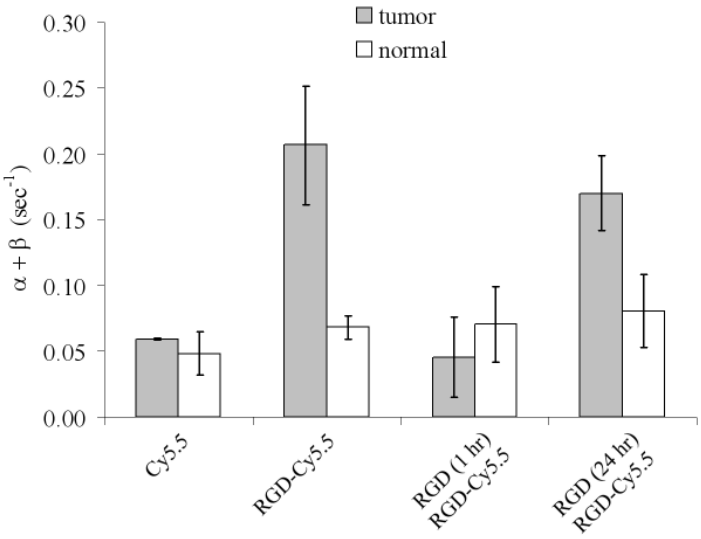

Figure 6.6. Results of the non-linear least squares regression in determining the sum of the pharmacokinetic complex rate constants $\alpha + \beta$. The column height represents the mean value of the test group listed along the abscissa while the error bars represent the standard deviation. The time in parenthesis represents the time between injection of the RGD peptide and the RGD-Cy5.5 conjugate.

or the conjugate preceded by the injection of the RGD-peptide 24-hours earlier, respectively. Statistical analysis revealed that while these values are statistically similar to each other at a 95% significance level they are in fact different from the values of the remaining test groups. Thus, the value of α is on average an order of magnitude greater from within the tumor ROI of these two test groups of animals as it is from the tumor ROIs of animals in the remaining groups or the normal ROIs of animals in all groups. The sum $\alpha + \beta$ exhibits the same trend. These results suggest that pharmacokinetic differences between Kaposi's sarcoma and normal tissue are reflected in the value of the parameter α and the sum $\alpha + \beta$ when the conjugate RGD-Cy5.5 dye is employed alone

or 24-hours following the injection of the RGD peptide. The impact of injection of the RGD peptide prior to the injection of the conjugate dye and the corresponding change in the parameter α is seen graphically in Figure 6.3 in the α–phase or the early part of the fluorescence intensity profiles.

From the studies involving the administration of the RGD peptide prior to the administration of the RGD-Cy5.5 conjugate one may draw the following conclusions. First, because the net effect of administering the RGD peptide one hour prior to the RGD-Cy5.5 conjugate is the reduction of the tumor uptake of the dye, as evidenced by the reduction of the parameter α from a mean value of 0.21-sec^{-1} (for animals injected with the RGD-Cy5.5 conjugate alone) to 0.043-sec^{-1} (for animals pretreated with the RGD peptide one hour prior to the administration of the RGD-Cy5.5 conjugate), and since the $\alpha_v\beta_3$ integrin receptor overexpressed on Kaposi's sarcoma is known to bind the RGD peptide, the pharmacokinetic analyses verify the specific binding of the RGD-Cy5.5 conjugate to the Kaposi's sarcoma tumor model. Second, because the value of α obtained from the tumor ROIs of animals injected with the conjugate dye alone or the conjugate dye 24-hours following the pretreatment with the RGD peptide are statistically similar, one may speculate that the turnover of the $\alpha_v\beta_3$ integrin receptor expressed on the cell surface of Kaposi's sarcoma occurs within 24-hrs. Given experimental dynamic *in vivo* fluorescence data obtained subsequent to the injection of the RGD-Cy5.5 conjugate at various intervals following the administration of the RGD peptide, one may be able to experimentally determine receptor turnover time using a pharmacokinetic analysis. Finally, since $\alpha + \beta$ is equivalent to the sum of all the rate

constants of the compartmental pharmacokinetic model, and since the $\alpha_v\beta_3$ integrin receptors bind the RGD peptide such that the rate constant for cellular uptake of the dye conjugate becomes essentially zero, $k_c = 0$, the difference in the value of $\alpha + \beta$ between animals injected with the conjugate dye alone and animals injected with the conjugate one hour after the pretreatment with the RGD peptide reflects the value of the rate constant for specific cellular uptake of the conjugate k_c. Thus, the value of rate constant for the specific cellular uptake of the RDG-Cy5.5 conjugate was found to have a mean value of $k_c = 0.16\,\text{sec}^{-1}$.

Fluorescence images of all animals studied were also obtained at 24-hour intervals following the administration of the contrast agent. Figure 6.7 displays the images of raw fluorescence (i.e. no background subtraction) obtained 24-hours and 48-hours following the initial injection of the contrast agent for a representative animal of each of the four test groups studied. The fluorescence images overlay white light images to allow for visualization of the entire animal and are plotted on the same linear scale to allow for a direct quantitative comparison of the images. From the images of Figure 6.7(a) it is clear that the Kaposi's sarcoma tumor was not visible from the fluorescence images at any time following the injection of the free Cy5.5 dye. In this case and the other cases as well, the visible fluorescence intensity originating from the animal gut is due to animal diet. The Kaposi's sarcoma tumor was clearly visible 24-hours and 48-hours after the administration of the RGD-Cy5.5 peptide, as evidenced in Figures 6.7(b-d), and returned to baseline after about 168-hours. At any given time, the fluorescence intensity originating from the tumor was highest for the animal that was

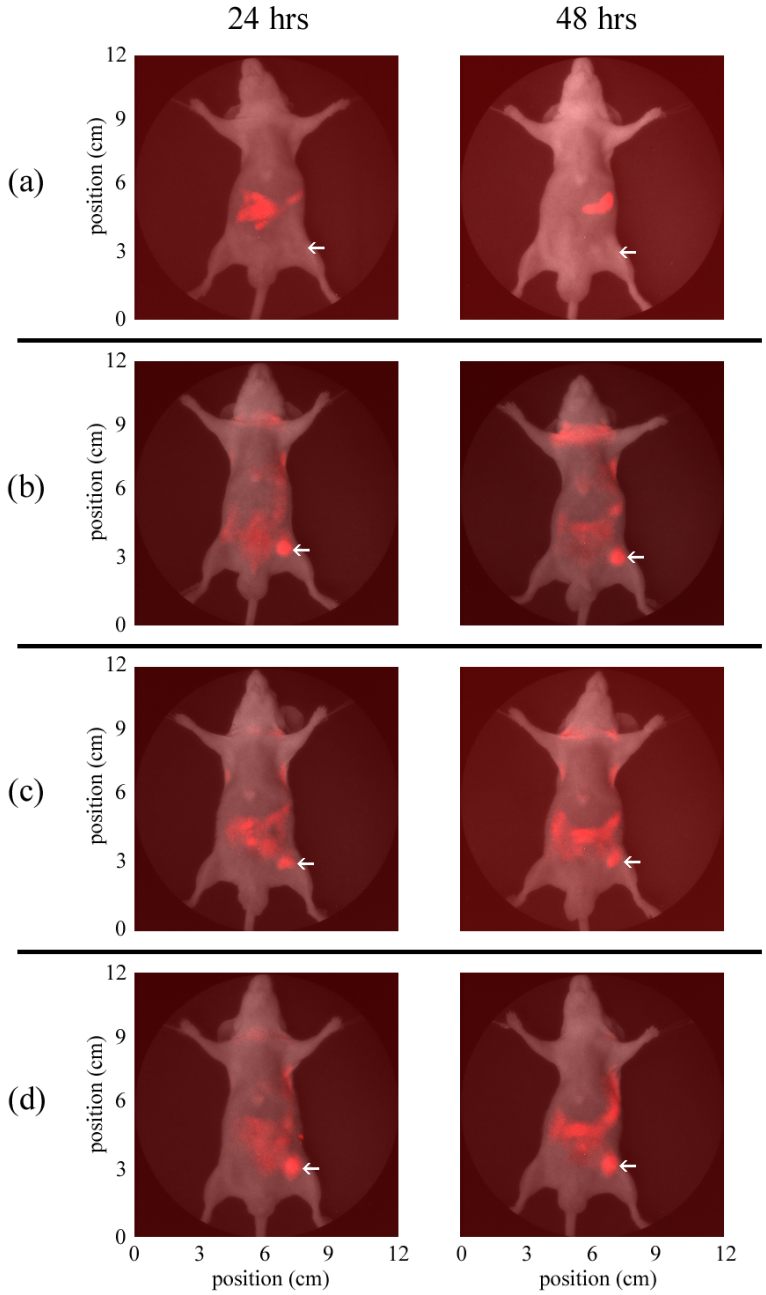

Figure 6.7. Raw fluorescence images (no background subtraction) obtained 24-hours (1st column) and 48-hours (2nd column) after the administration of (a) Cy5.5, (b) RGD-Cy5.5 conjugate alone, (c) RGD-Cy5.5 conjugate 1-hour after the injection of RGD peptide, and (d) RGD-Cy5.5 conjugate 24-hours after injection of the RGD peptide. The fluorescence images overlay white light images to clearly outline the animal. The white arrows indicate the location of the xenografted Kaposi's sarcoma tumor.

administered the RGD-Cy5.5 conjugate alone, Figure 6.7(b); slightly diminished for the animal injected with the RGD peptide 24-hours prior to the administration of the conjugate dye, Figure 6.7(d); and lower still for the animal that received the RGD peptide one hour prior to the administration of the RGD-Cy5.5 conjugate, Figure 6.7(c). These results further substantiate the specific cellular binding of the RGD-Cy5.5 conjugate to Kaposi's sarcoma.

6.5 Conclusion

Herein the use of a pharmacokinetic analysis on *in vivo* fluorescence data to test for the specificity of a targeted diagnostic fluorescence contrast agent in a murine Kaposi's sarcoma model has been demonstrated. The contrast agent, a peptide-cyanine dye conjugate termed RGD-Cy5.5, is targeted to $\alpha_v\beta_3$ integrin receptors commonly overexpressed on angiogenic epithelium. Dynamic fluorescence images obtained immediately subsequent to the intravenous injection of the conjugate dye and a three-compartment pharmacokinetic model were employed to estimate the rate constant for the cellular uptake of the dye in Kaposi's sarcoma tumor tissue. The rate constant was found to have a value of 0.16-sec^{-1}. Finally, based on the experiments employing the RGD peptide to block or internalize the target $\alpha_v\beta_3$ integrin receptors, one may speculate that the integrin receptor turnover occurs approximately within 24-hrs.

With targeted therapeutics becoming more common alternatives for the treatment of cancer, there exists a need for a reliable technique capable of assessing the efficacy of selected targeting schema. While current methodologies employ *in vitro* assays, an *in vivo* technique may be extremely valuable to help establish specific membrane receptors

as bona fide targets for diagnostics and therapeutics. The pharmacokinetic analysis developed in this report may provide one such *in vivo* technique. Finally, the results demonstrate that utilizing a relatively simple mathematical model it may be possible to estimate receptor-ligand specificity, receptor expression level, and receptor turnover rate, all of which are important indicators of a targeting scheme's utility.

7. IMAGING OF EPIDERMAL GROWTH FACTOR RECEPTOR[†]

In addition to using pharmacokinetic analysis to evaluate novel targeting fluorescent contrast agents, simple continuous wave fluorescence imaging may be used to evaluate novel contrast agents. In this section, CW fluorescence imaging is used to image human breast cancer xenografts following intravenous administration of an epidermal growth factor receptor-targeted fluorescent contrast agent. As in the previous section, the work herein represents the collaborative effort with researchers at M.D. Anderson Cancer Center who developed the contrast agents and animal models.

7.1 Introduction

Non-invasive optical imaging may soon play a critical role in the early diagnosis of disease, the monitoring of early therapeutic response to treatment regimens, and the design of individually tailored therapy for enhanced efficacy. With near-infrared (NIR) optical imaging comes the promise of an inexpensive, highly sensitive, and non-ionizing imaging modality capable of dynamic, real-time *in vivo* images. Additionally, with the versatility of fluorescent probe design that is only now starting to become realized, optically based molecular imaging techniques are becoming more attractive.

Prior work in the design of specific fluorescent probes has established the use of antibody-directed targeting of NIR fluorescent probes[21,23-25] as well as fluorophores

---

[†] Reprinted in part with permission from "In vivo fluorescence imaging of cyanine derivative modified with epidermal growth factor EGF-Cy5.5 in a murine model of carcinogenesis" by M. Gurfinkel, S. Ke, C. Li, and E.M. Sevick-Muraca, 2003. *Proceeding of the SPIE: Genetically Engineered and Optical Probes for Biomedical Applications* **4967**, 108-116. Copyright 2003 by the International Society for Optical Engineering.

conjugated with polymers for fluorescent activation by metalloproteases[35] and intracellular enzymes[33,34] present in cancer. However, adverse immunogenic reactions were often observed with antibody-directed targeting[26] and, for the detection of solid tumors, the penetration of large antibodies and polymeric complexes may be impeded by pressure gradients within the tumor.[29] Alternatively, small peptide conjugation to fluorophores has been demonstrated *in vivo* to target somatostatin,[27,28,30] bombesin,[27,28,30] and transferrin[31] receptor-rich tumors, as well as hydroxyapatite for the monitoring of osteoblastic activity.[32]

In this section, the use of a novel receptor-targeted NIR fluorescent probe is described and its specific targeting of human breast cancer xenografts is demonstrated in a small animal model. An ICCD detection system is employed to acquire whole-body fluorescence images immediately following the intravenous administration of the fluorescence probe, as well as fluorescence data at later time points, both of which are used to validate the specificity of the probe for the cancer target.

7.2 Materials and Methods

7.2.1 Fluorescent Dyes and Animal Model

For this study, the fluorescent contrast agents and animal models were developed at the M.D. Anderson Cancer Center by Dr. Xiaxia Wen, and Dr. Shi Ke and Dr. QingPing Wu, respectively. For the synthesis of the epidermal growth factor receptor (EGFr)-targeted fluorescent dye, a quantity of 0.2-mg of human recombinant epidermal growth factor (EGF) (MW 6kD; Sigma, St. Louis, MO) was labeled by incubation with four

equivalents of the monofunctional hydroxysuccinimide ester of Cy5.5 dye (MW 1kD; Amersham Pharmacia Biotech Inc., Piscataway, NJ). The resulting fluorescent probe, termed EGF-Cy5.5, was composed of one molecule of EGF for every two Cy5.5 molecules (molar ratio 1:2) as determined by MALDI-MS. Indocyanine green (ICG) (Sigma) and C225 antibody (ImClone Systems Inc., New York, NY) were used as received from the manufacturer.

Four to six week-old female athymic nude mice (nu/nu, 18-22-g) (Harlan Sprague Dawley, Inc., Indianapolis, IN) were housed five per cage and fed a diet of sterilized chow and water ad libitum. Animals were kept in a pathogen-free mouse colony in the Department of Veterinary Medicine (The University of Texas M.D. Anderson Cancer Center). The facility is accredited by the American Association for Laboratory Animal Care and all experiments were performed in accordance with the guidelines of the Institutional Animal Care and Use Committee.

Human breast adenocarcinoma cell lines MDA-MB-435 and MDA-MB-468 (American Type Culture Collection, Rockville, MD) were maintained in Dulbecco's Modified Eagle's Medium / Nutrient Mixture F-12 Ham (DMEM/F12) and 10% fetal bovine serum (FBS) (Gibco, Grand Island, NY) in a humidified atmosphere of 5% CO_2 at 37°C. Cells were pelleted by centrifugation and resuspended in sterile PBS. Each nude mouse was injected with the adenocarcinoma cells (2-3 $\times$ 10^6 cells) subcutaneously into the chest region. Fluorescence imaging of the mice took place once the tumors reached approximately 6-mm in size.

7.2.2 Imaging System

The small animal imaging system was comprised of (i) a laser diode source of excitation photons; (ii) an intensified charge-coupled device camera (ICCD) detection system; and (iii) a personal computer for data acquisition and storage. The laser diode source (785-nm, 80-mW for ICG; 660-nm, 35-mW for Cy5.5) was expanded to approximately 8-cm diameter using a plano-convex lens to provide an excitation source over nearly the entire animal. The detection system consisted of an image intensifier (model FS9910C, ITT Night Vision, Roanoke, VA) lens-coupled to a 16-bit CCD camera (model CH350, Photometrics, Tucson, AZ). The system was designed such that the field of view could be varied from 3 × 3-cm to over 12 × 12-cm by varying the image distance of the 50-mm lens used to focus the image onto the photocathode of the intensifier. Such a design permits zoom capabilities without resorting to moving either the camera above the animal or the anesthetized animal itself. The lens was fitted with a holographic notch-plus band-rejection filter (785-nm center wavelength for ICG, 660-nm center wavelength for Cy5.5; Kaiser Optical Systems, Inc., Ann Arbor, MI) and a bandpass filter (830-nm center wavelength for ICG, 710-nm center wavelength for Cy5.5; CVI Laser Corporation, Albuquerque, NM) to reject back-scattered and reflected excitation photons and isolate fluorescent photons. For the acquisition of white-light images, a low-power lamp provided a white-light source and the filters were removed. Image acquisition was directed by V++ software (Digital Optics, Auckland, New Zealand) while data processing and analysis were accomplished using Matlab software (The MathWorks, Inc., Natick, MA).

7.2.3 Fluorescence Imaging

Mice were anaesthetized (Nembutal, Sigma; 50-mg/kg administered i.p.) and positioned beneath the imaging system. The image acquisition time was held constant at 800-ms while intensifier gain was varied from 40% of the maximum gain (for white light images) to 95% of the maximum gain (for fluorescence images). The mice were then injected via tail vein with either ICG (0.3-mL, 890-picomoles), Cy5.5 dye alone (0.3-mL, 17-nanomoles), or EGF-Cy5.5 conjugate (0.3-mL, 17-nanomoles equivalent Cy5.5). Fluorescence images were obtained every six seconds for a period of approximately 20-minutes following initial injection of contrast agent, and again every 24-hours thereafter until very little or no fluorescent signal was detectable from the tumor region of interest (as determined qualitatively) for up to 192-hours.

7.3 Results and Discussion

Images of endogenous fluorescence at 830-nm and 710-nm (emission wavelengths of ICG and Cy5.5, respectively) revealed no endogenous fluorophores at 830-nm while some extent of endogenous fluorescence was observed to originate from the intestines at 710-nm. Experiments later confirmed that the endogenous signal at this wavelength was primarily a result of the animals' diet. Nonetheless, the location of the tumor in the chest region of the animal enabled the discrimination of fluorescent signal emanating from tumor from that emanating from endogenous abdominal sources.

The use of an intensified CCD detection system not only allows for the detection of small quantities of fluorescent dye, but it enables the use of sub-second exposure times which, in turn, permits the rapid acquisition of fluorescence data. As a result,

starting at the time of injection, the circulation of fluorophore may be followed throughout the body in real time and thus, biodistribution and pharmacokinetic studies may be performed for early time points. Figure 7.1 illustrates the mean fluorescence intensity as a function of time (the initial twenty minutes following injection of agent) from the ROIs defining tumor and normal tissues for all tumor models and contrast agents studied. Regardless of tumor type, there is little difference in the pharmacokinetics when a non-specific agent is employed [Figs. 7.1(a), 7.1(c) , 7.1(d)] or when the EGFr specific EGF-Cy5.5 dye is employed in an EGFr-negative tumor model [Fig. 7.1(b)]. Furthermore, the greatest disparity in pharmacokinetics between normal and tumor ROIs occurs for EGF-Cy5.5 in an EGFr-positive, tumor-bearing mouse [Fig. 7.1(f)]. Pretreatment of an EGFr-positive, tumor-bearing mouse with C225 antibody dramatically reduces this difference in pharmacokinetics [Fig. 7.1(e)]. Taken together, these results suggest that the difference in pharmacokinetics is a result of the specific binding of EGF-Cy5.5 to EGFr in MDA-MB-468 tumor cells.

Figure 7.2 presents fluorescence images in pseudocolor obtained 24- and 48-hours after the injection of EGF-Cy5.5 into an EGFr-negative, MDA-MB-435 tumor-bearing mouse. The figure illustrates that there is little accumulation of EGF-Cy5.5 in the MDA-MB-435 tumor 24-hours post injection (tumor fluorescence is approximately 20 percent of the maximum signal). At 48-hours post injection, tumor fluorescence is still weaker, with the signal slightly above background fluorescence. On the other hand, Figure 7.3 depicts the fluorescence images obtained after the injection of EGF-Cy5.5 into an EGFr-positive, MDA-MB-468 tumor-bearing mouse. Unlike the previous case,

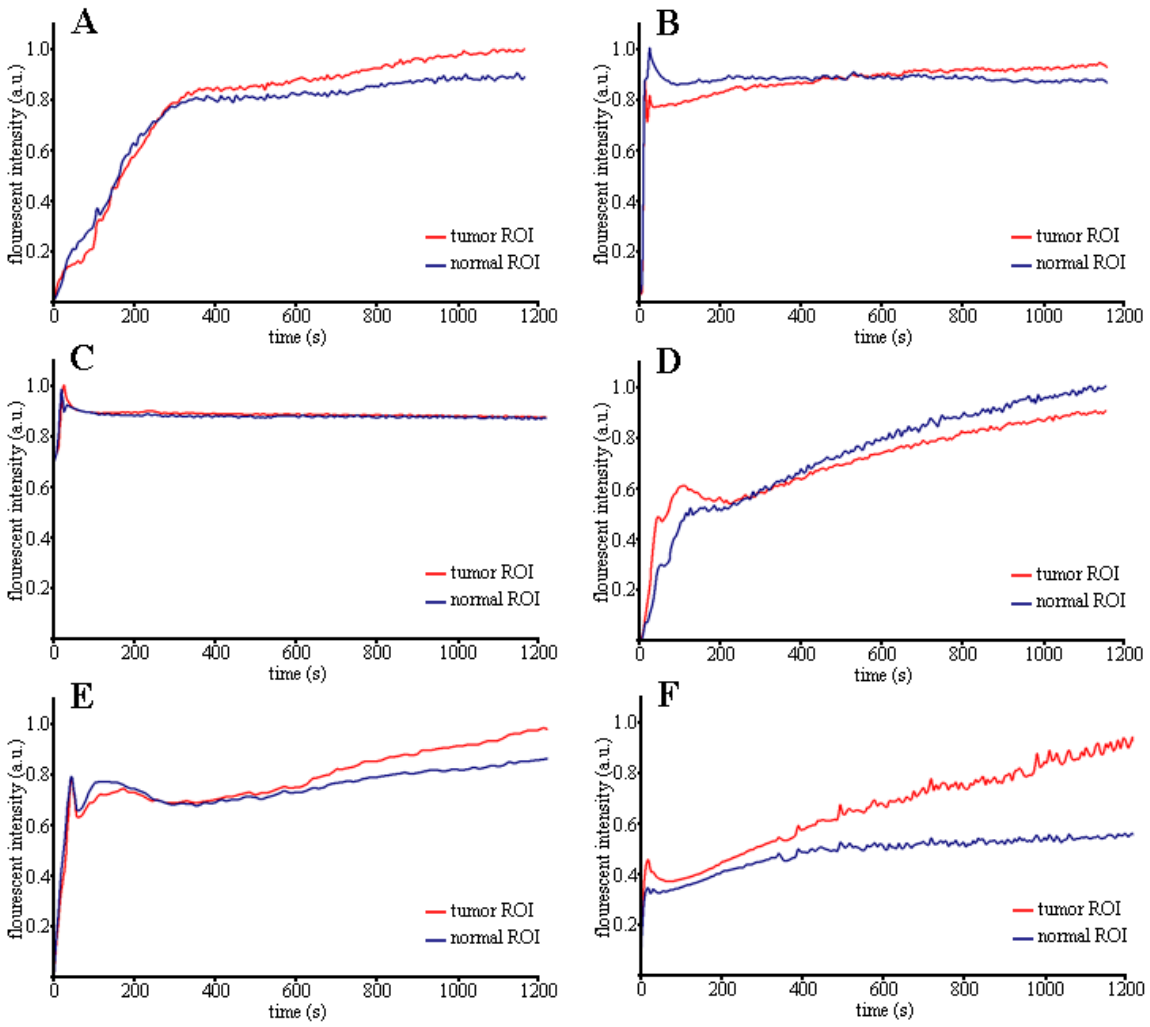

Figure 7.1. Fluorescent intensity as a function of time after injection of (a) Cy5.5 in an MDA-MB-435 tumor-bearing mouse, (b) EGF-Cy5.5 in an MDA-MB-435 tumor-bearing mouse, (c) ICG in an MDA MB-468 tumor-bearing mouse, (d) Cy5.5 in an MDA-MB-468 tumor-bearing mouse, (e) EGF-Cy5.5 in an MDA-MB-468 tumor-bearing mouse pretreated with C225 antibody 24 hours earlier, and (f) EGF-Cy5.5 in an MDA-MB-468 tumor-bearing mouse.

the tumor fluorescence signal is appreciable after 24-hours and is greatest after 96-hours, at which time it is approximately seventy percent of the maximum signal. It is not until 192-hours post-injection when the tumor fluorescence signal drops below twenty percent

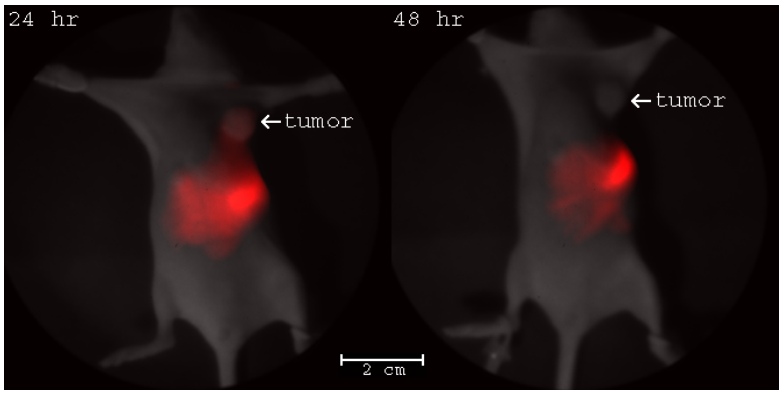

Figure 7.2. Pseudocolor fluorescence images of a tumor-bearing (MDA-MB-435) mouse collected 24 and 48-hrs following injection of EGF-Cy5.5. Regions of high fluorescence intensity appear dark red. The obtained fluorescence images overlay a white light image to permit registration of the fluorescence signal and visualization of the entire animal.

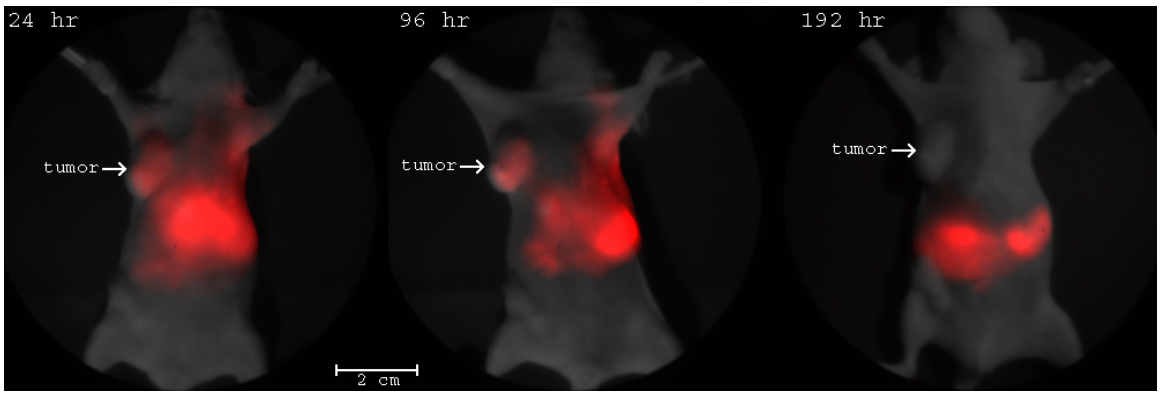

Figure 7.3. Pseudocolor fluorescence images of a tumor-bearing (MDA-MB-468) mouse collected 24, 96 and 192-hrs following injection of EGF-Cy5.5. Regions of high fluorescence intensity appear dark red. The obtained fluorescence images overlay a white light image to permit registration of the fluorescence signal and visualization of the entire animal.

of the maximum detected signal. Figure 7.4 illustrates the fluorescence images obtained from an EGFr positive, MDA-MB-468 tumor-bearing mouse pretreated with C225 antibody 24-hours prior to injection of EGF-Cy5.5. No significant tumor fluorescence is observed at 24-hours post-injection and tumor fluorescence is indistinguishable from background signal at 48-hours. The images suggest that pretreatment with C225 antibody prevents EGF-Cy5.5 accumulation in the tumor, further substantiating the claim that EGF-Cy5.5 binds EGFr *in vivo* in MDA-MB-468 tumor.

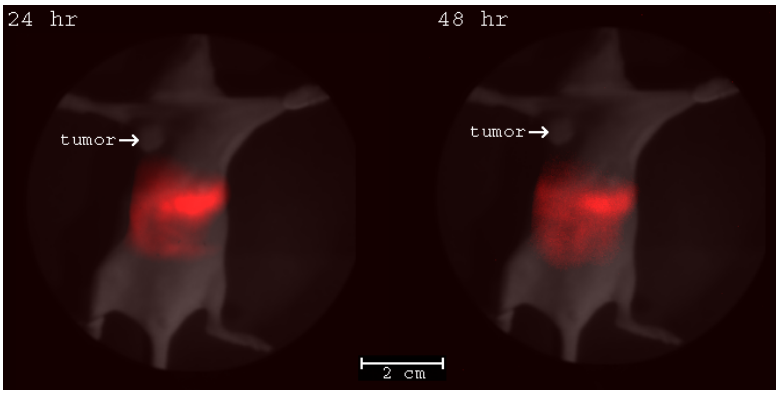

Figure 7.4. Pseudocolor fluorescence images of a tumor-bearing (MDA-MB-468) mouse collected 24 and 48 hours following injection of EGF-Cy5.5. The EGF-Cy5.5 injection was preceded by the administration of C225 antibody 24-hours earlier. Regions of high fluorescence intensity appear dark red. The obtained fluorescence images overlay a white light image to permit registration of the fluorescence signal and visualization of the entire animal.

7.4 Conclusion

The results of the work in this section demonstrate that simple fluorescence imaging may be used to visualize the fluorescence resulting from tumor laden fluorophores. Furthermore, the results demonstrate that the specific fluorescent contrast agent, EGF-Cy5.5, can be used to discriminate EGFr-expressing tumor from non-tumor tissue based on preferential accumulation of the agent in the tumor. Furthermore, the results indicate that the non-specific contrast agents ICG and Cy5.5 show no preferential accumulation in either the EGFr-negative MDA-MB-435 or EGFr-positive MDA-MB-468 tumor-bearing mice. Negligible tumor fluorescence was detected 24-hours after dye administration in each case. Furthermore, the EGF-Cy5.5 conjugate displayed specificity only for MDA-MB-468 tumors but not for MDA-MB-435 tumors. Tumor fluorescence reached a maximum after 96-hours in the MDA-MB-468 tumor and only dropped to insignificant levels after 192-hours.

Additionally, the initial pharmacokinetics following dye administration may be used to reflect the differences in specificity of the dye. Both ICG and Cy5.5 show no difference between tumor and non-tumor pharmacokinetics regardless of tumor EGFr expression level. EGF-Cy5.5 demonstrates no differential pharmacokinetics between tumor and non-tumor tissue for the EGFr-negative MDA-MB-435 tumor-bearing mouse whereas, the greatest observed difference in pharmacokinetics between tumor and non-tumor tissue occurs for EGF-Cy5.5 in the EGFr-positive MDA-MB-468 tumor-bearing mouse. These findings suggest that specific or targeted contrast agents may be used more effectively for the diagnosis of solid tumors.

8. PRELIMINARY STUDIES

In additional to the complete animal imaging studies presented in Sections 5–7, the developed optical imaging instrumentation has been utilized to investigate a number of additional novel contrast agents, developed by researchers at M.D. Anderson Cancer Center (MDACC) under the direction of Dr. Chun Li, for the detection of carcinogenesis *in vivo*. This section describes preliminary results from a number of ongoing clinical investigations.

8.1 Imaging Carcinogenesis in Small Animals

In addition to the fluorescent contrast agents developed to target low-density lipoprotein (LDL) receptors (Section 5), $\alpha_v\beta_3$ integrin receptors (Section 6), and epidermal growth factor receptors (EGFr) (Section 7), a number of novel chemical constructs have been developed for consideration as delivery vehicles for optical contrast agents. Among them is a conjugate of the cyanine dye, Cy5.5, synthesized at MDACC by Dr. Wei Wang to specifically target matrix-metalloprotease (MMP), an enzyme whose presence and strong upregulation in many cancers, including human prostate cancer, has been noted and shown to promote metastatis.[113-115]

An additional contrast agent under investigation, synthesized at MDACC by Dr. Xianyi Cao, is a conjugate comprised of the fluorophore indocyanine green (ICG) bound to a poly-L-glutamic acid polymer. Although its molecular targeting mechanism remains uncertain at this time, the conjugate has shown specificity towards bone and the skeletal system. Furthermore, the poly-L-glutamic polymer construct allows the

additional conjugation of a nuclear radiolabel, ^{111}In, and thus permits dual imaging capabilities and initial comparisons of optical imaging and nuclear imaging technology using the same contrast agent.

Finally, consider the following comparison of the commonly-used nuclear radiolabel ^{111}In and optical probe ICG. ^{111}In has a typical specific activity of 1.55×10^{16} emissions/sec/g .[116] The fluorophore ICG exhibits a mean lifetime of 0.56 nsec and has a molecular weight of $775\,\mathrm{g/mol}$.[14] Because each molecule can repeatedly re-emit fluorescent photons, the mean lifetime and molecular weight combine to yield an 'optical' specific activity for ICG of 1.39×10^{30} emissions/sec/g. Thus, it requires approximately 9×10^{13} times more mass of ^{111}In to yield the same number of radiative emissions per unit time as ICG. This analysis represents a theoretical upper limit to the number of radiative events potentially available for detection. While it does not consider radioactive decay, fluorescence quenching, detector collection efficiencies, quantum efficiency of fluorophore, and the availability of excitation source, it still makes a clear argument that optical imaging with fluorescent contrast agents may be superior to nuclear imaging when it comes to the required concentration of contrast agent. Certainly the other factors may mitigate this large difference in required contrast agent dose. But given this argument, it is clear why optical imaging using fluorescent contrast agents is the topic of so many scientific inquiries.

An additional distinct advantage near-infrared fluorescence imaging possesses over conventional nuclear imaging is the ability to simultaneously image multiple contrast agents. Because nuclear scintillation counters cannot distinguish the source of

the gamma emitter, they are incapable of discriminating between multiple radiolabels. However, because fluorescent contrast agents may exhibit different excitation and emission spectra, an optical detector capable of differentiating different wavelengths has the capacity to measure fluorescent emissions from multiple fluorescent probes. As discussed below, this feature of fluorescence imaging can further be exploited if time-resolved measurements are made to capture information pertaining to the fluorescence decay kinetics of the fluorophore.

Simultaneous imaging of two probes was demonstrated in a preliminary study of a murine model of prostate cancer; a study conducted at MDACC in collaboration with Dr. Chun Li and colleagues. Prior to imaging, human prostate cancer was xenografted into the nude mouse via an intra-tibial injection and the resulting tumor mass was allowed to grow to approximately 5-mm in size. The nude mouse was then tail-vein injected with 10-nmol of the ICG-poly-L-glutamic acid polymer conjugate and 15-nmol of the Cy5.5 probe conjugated to target MMP, and imaged 24-hrs later using the small animal ICCD detection system described in Section 3. The sufficient separation of the fluorescence spectra between ICG and Cy5.5 (peak fluorescent emission occurs at ~810-nm and ~710-nm, respectively) permits the simultaneous fluorescence imaging and coregistration of the two fluorescent probes. Figure 8.1 presents the fluorescence images of both fluorescent probes obtained after the mouse was sacrificed and the skin removed to improve visualization of underlying structures. Figure 8.1(a) is a pseudocolor fluorescence image of the ICG conjugate dye. The individual vertebrate of the tail and the bones of the legs are clearly visible. Figure 8.1(b) is a pseudocolor fluorescence

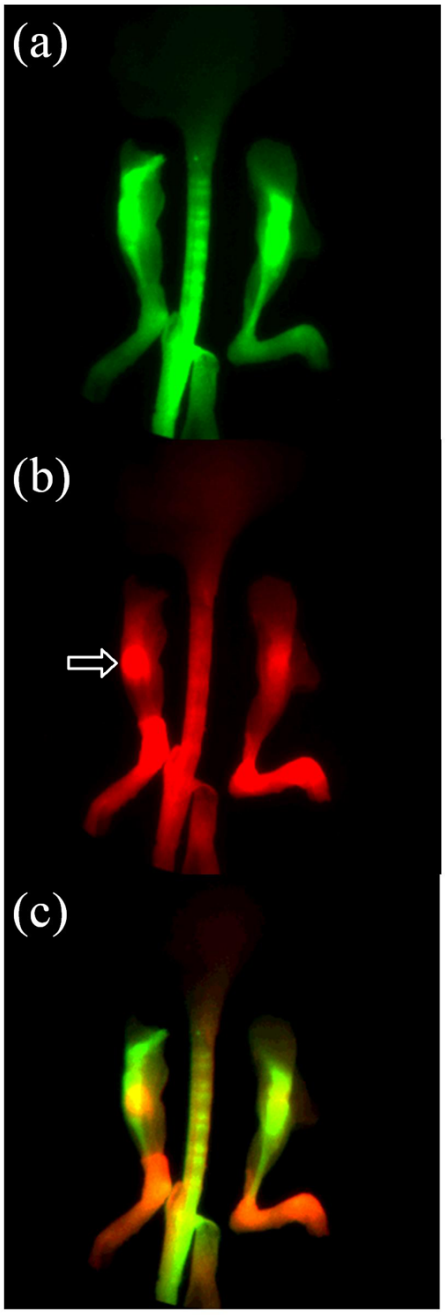

Figure 8.1. Pseudocolor fluorescence images of (a) ICG-poly-L-glutamic acid polymer conjugate, and (b) Cy5.5 conjugate targeted to MMP obtained 24-hrs following the intravenous administration of the said fluorescent probes in a prostate cancer bearing nude mouse. The white arrow indicates the location of the prostate cancer tumor. Panel (c) is a composite image of the images in panels (a) and (b) where the ICG conjugate fluorescence is pseudocolored green while the Cy5.5 conjugate fluorescence is pseudocolored red.

image of the Cy5.5 conjugate dye. The white arrow indicates the location of the prostate cancer tumor which is clearly visible due to Cy5.5 fluorescence. Figure 8.1(c) is a composite pseudocolor fluorescence image of both conjugate dyes (ICG conjugate is pseudocolored green; Cy5.5 conjugate dye is pseudocolored red). In the composite image, the location of the prostate cancer tumor is clearly observed to coincide with the initial intra-tibial implantation.

8.2 Small Animal Frequency-Domain Photon Migration Imaging

Initial attempts to acquire frequency-domain photon migration images of tumor fluorescence *in vivo* were also conducted. Although FDPM is unnecessary to visualize fluorescence from very shallow tissue depths and small volumes such as the small animals utilized in the experiments, it is necessary for the tomographic three-dimensional recovery of tumor size and location in larger volumes more relevant to clinical imaging of larger subjects including humans.[39-41,117] Previous tests havevalidated the instrumentation for the acquisition of frequency-domain data from tissue-simulating phantoms (Section 4). To validate the instrument for the acquisition of FDPM data from fluorescence-laden tumors in small animal models, a number of preliminary experiments were conducted.

In addition to the continuous-wave imaging studies described in the previous section, a small animal model of breast carcinoma was imaged using FDPM techniques. The ICCD imaging system used to obtain the FDPM data is described in detail in Section 3. Four phase-sensitive fluorescence intensity images were acquired at sixteen equally spaced phase-delays between the frequency synthesizers modulating the

excitation source and the intensifier detector. Unless otherwise noted, all FDPM studies were conducted at an RF-modulation frequency of 100-MHz. The phase and RF-amplitude of the emitted fluorescence photon density wave was then computed at each pixel of the CCD array via a fast Fourier transform (FFT) of the mean of the phase-sensitive intensity data.[60]

Figure 8.2 shows the results of the frequency-domain imaging experiment performed on an MDA-MB-468 tumor-bearing mouse 96-hours following injection of EGF-Cy5.5. In order to achieve desirable modulation depth, the intensifier cathode voltage was reduced by 70% and the diameter of the expanded excitation source was decreased to approximately 6-cm. These experimental changes could explain why the DC image shows reduced tumor contrast compared to the CW images of the same animal (compare to Figure 7.3). Nonetheless, the tumor is clearly evident in the image of AC amplitude. Furthermore, comparing the normalized DC and AC intensities along the same horizontal slice through the image reveals that the normalized AC intensity is consistently greater than the DC intensity. This is due in part to the inherent ability of the frequency-domain technique to filter out non-modulated ambient light which may contribute to noise in CW imaging.

Although the FDPM images of phase-lag have been omitted from this initial experiment, they can be used to impart additional contrast, especially when a fluorophore designed to exhibit lifetime-sensitivity to its local biochemical environment is employed.

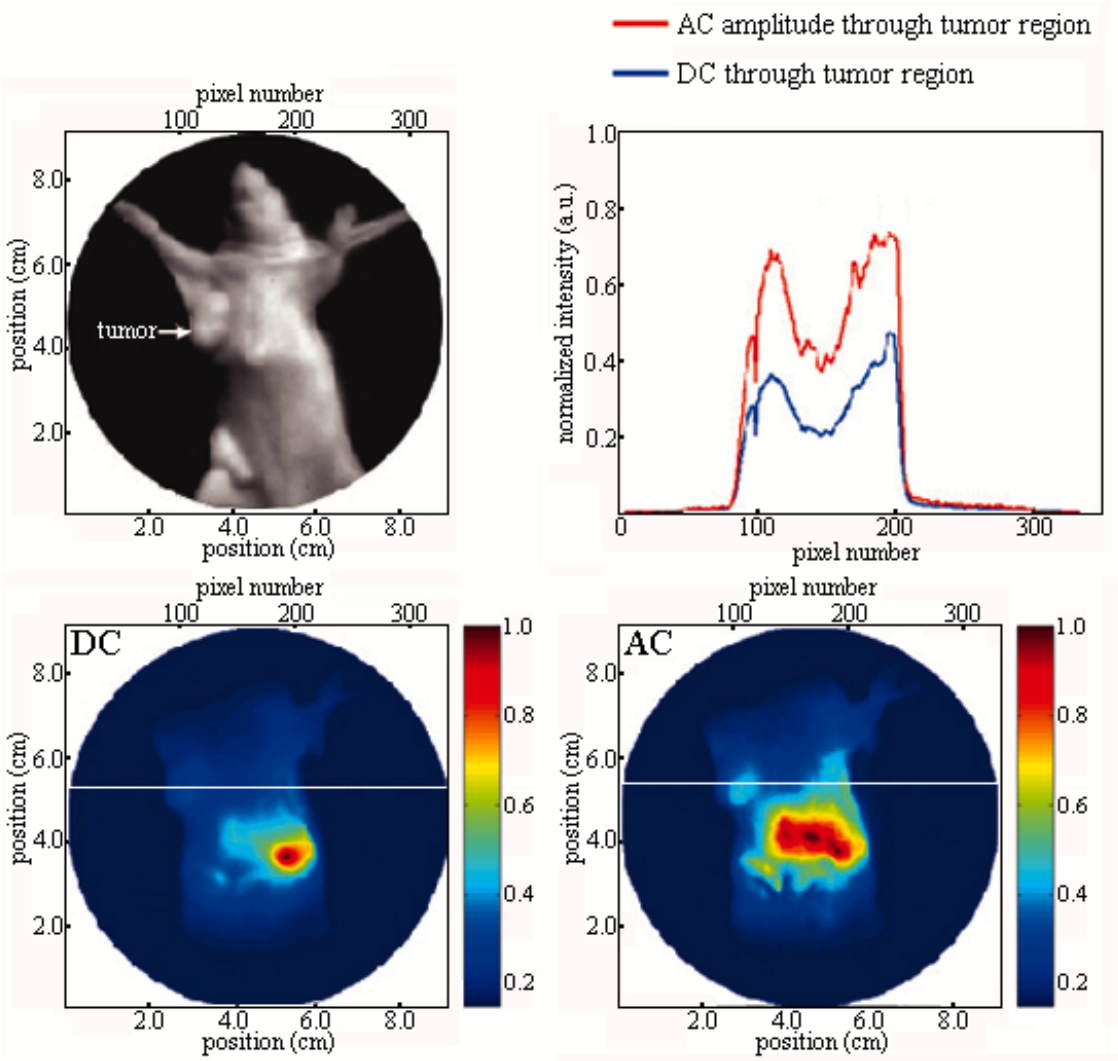

Figure 8.2. White light and frequency-domain images of DC and AC amplitude of a tumor-bearing (MDA-MB-468) mouse collected 96 hours following injection of EGF-Cy5.5. The normalized DC and AC intensity at each pixel on the line through the tumor region (shown in white) are also plotted.

To demonstrate the ICCD detection system's capacity to detect phase lag in FDPM imaging experiments, an experiment was conducted in which a prostate cancer tumor-bearing mouse was imaged with the two contrast agents described in the previous

section, that is, ICG-poly-L-glutamic acid polymer conjugate to target bone and the Cy5.5 conjugate to target MMP expression in the prostate cancer tumor.

FDPM imaging was conducted 24-hours following the intravenous administration of both contrast agents. Two FDPM experiments were conducted, one to image the fluorescence from each of the fluorescent probes. Again, the sufficient separation of the fluorescence emissions of the two fluorophores permits simultaneous imaging of both agents. Excitation light was delivered via an expanded laser diode source (660-nm for Cy5.5, 785-nm for ICG) and optical filters were used to isolate the emission wavelength of interest. In order to improve the modulation of the excitation source, and thus, the results of the FDPM imaging experiments, the expanded source was focused primarily over the region of the animal's leg containing the implanted prostate cancer tumor. Four phase-sensitive fluorescence intensity images were obtained at sixteen equally spaced phase-delays between the frequency synthesizers modulating the excitation source and the intensifier detector. The mean of the phase-sensitive fluorescence images at each phase delay was used in the FFT algorithm to compute the modulation amplitude and the phase-lag.[60]

Figure 8.3 shows the phase-lag images obtained from the experiments. Figure 8.3(a) is the phase-lag image obtained after imaging the fluorescence from the MMP-targeted Cy5.5 conjugate dye; Figure 8.3(b) is the phase-lag image obtained from the fluorescence images of the bone-targeted ICG-poly-L-glutamic acid polymer conjugate. Because the expanded excitation light was focused over the region of the leg containing the tumor, the phase contrast in distant regions of the animal is poor. Nonetheless, in

Figure 8.3(a) it appears that the tumor is delineated by the phase-contrast due to the Cy5.5 conjugate dye. It is difficult to discriminate any structures from the phase contrast due to the ICG polymer conjugate [Figure 8.3(b)] perhaps because ICG-polymer conjugate is located throughout the bones in the leg.

In addition to phase-lag images, the FDPM imaging study yielded images of DC and AC amplitude, and modulation depth (DC/AC). Figure 8.4 displays the FDPM results of the fluorescence imaging study conducted on the Cy5.5 conjugate dye. Figure 8.4(a) is a white light image, and Figures 8.4(b), 8.4(c), 8.4(d) are FDPM images of DC amplitude, AC amplitude, and modulation depth (DC/AC), respectively. The images of DC and AC amplitude clearly delineate the location of the prostate cancer tumor while the image of modulation depth primarily mirrors the region of the expanded excitation

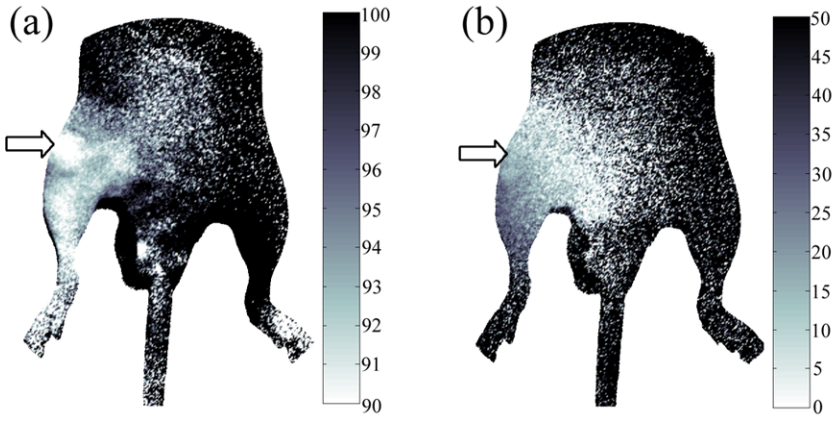

Figure 8.3. Phase-lag images obtained from FDPM imaging studies of (a) Cy5.5 conjugate targeted to MMP in prostate cancer and (b) bone-targeted ICG-polymer conjugate. The arrow indicates the location of the prostate cancer tumor and the scale is in units of degrees.

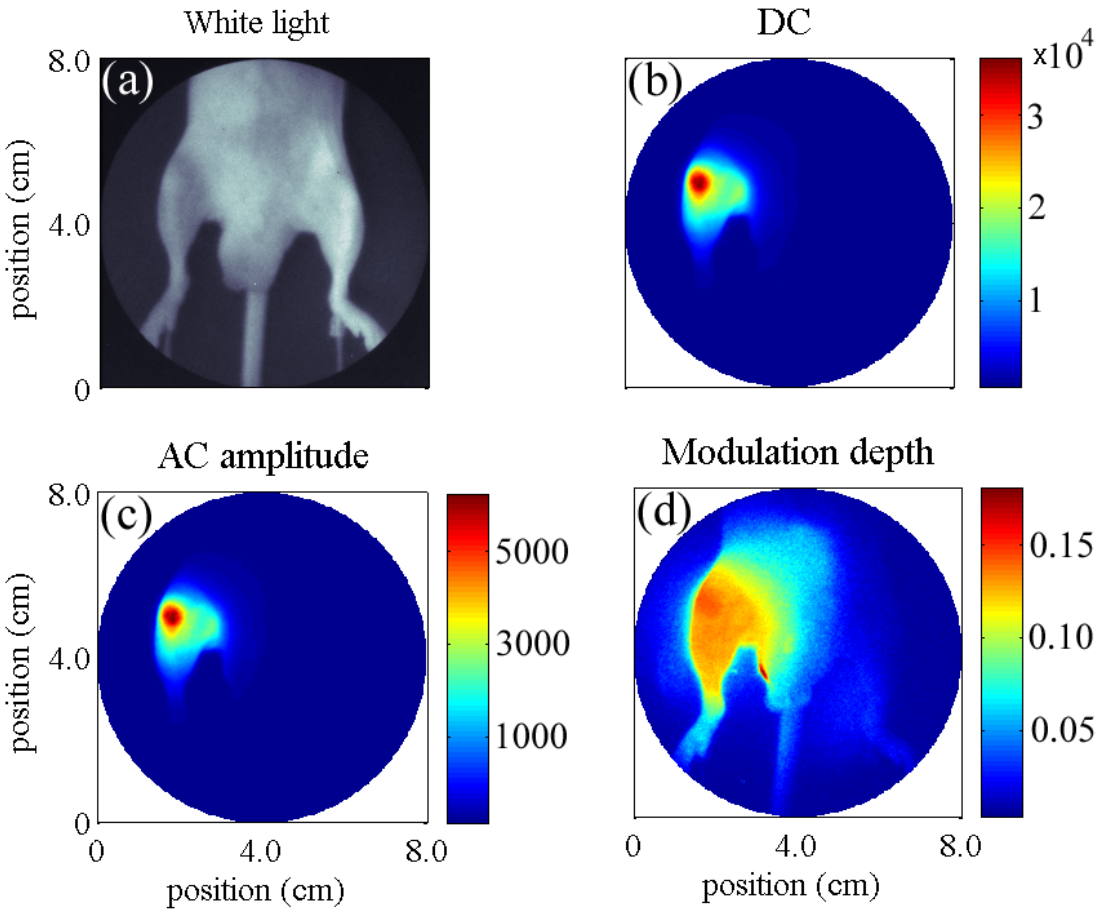

Figure 8.4. Results of the FDPM fluorescence imaging experiment conducted on a prostate cancer tumor-bearing mouse 24-hrs following the administration of a Cy5.5 conjugate dye targeted to MMP in prostate cancer. Panel (a) is a white light image, (b) DC amplitude, (c) AC amplitude, and (d) modulation depth.

light source. Similarly, Figure 8.5 displays the results of the FDPM imaging study on the ICG-polymer conjugate dye. Figure 8.5(a) is a white light image, and Figures 8.5(b), 8.5(c), 8.5(d) are FDPM images of DC amplitude, AC amplitude, and modulation depth (DC/AC), respectively. The images of DC and AC amplitude seem to highlight the patella and a portion of the tibia. When the images in Figures 8.4 and 8.5 are

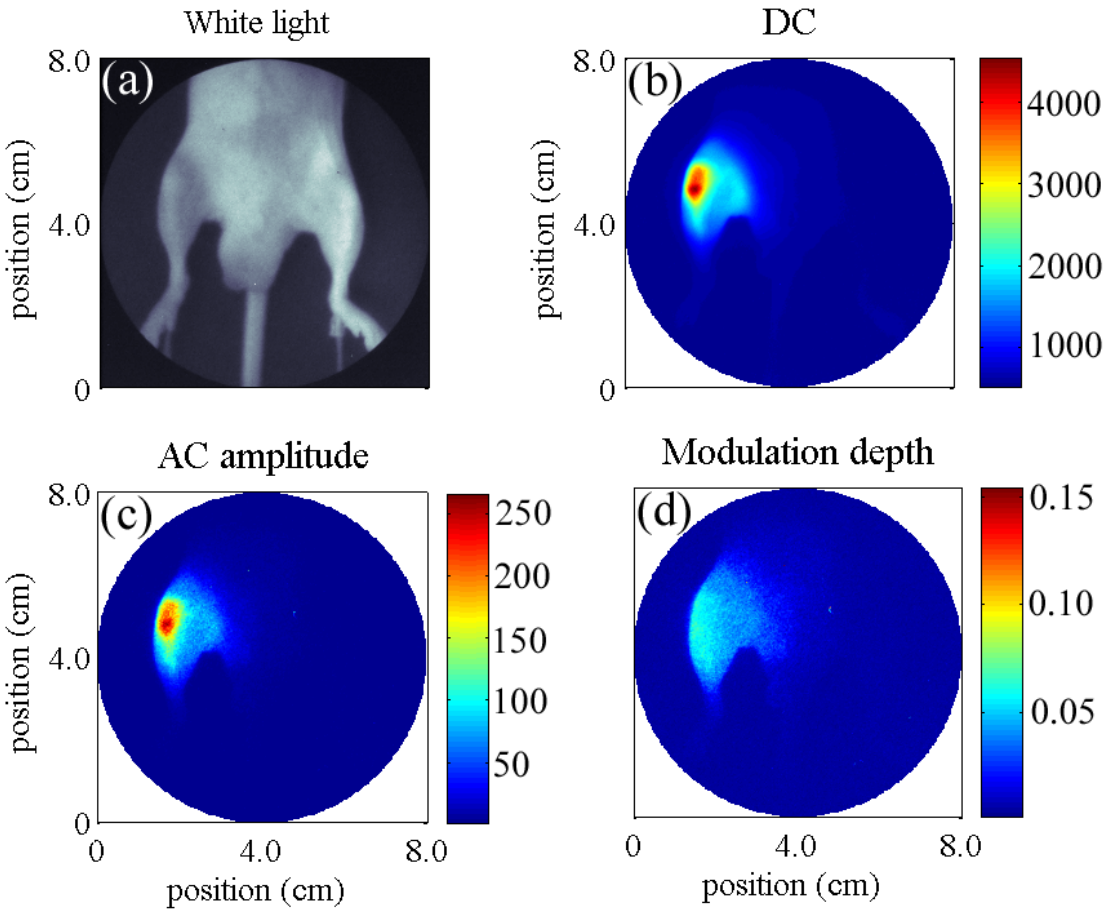

Figure 8.5. Results of the FDPM fluorescence imaging experiment conducted on a prostate cancer tumor-bearing mouse 24-hrs following the administration of a bone-targeting ICG-polymer conjugate dye. Panel (a) is a white light image, (b) DC amplitude, (c) AC amplitude, and (d) modulation depth.

coregistered, the regions of strongest fluorescence signal are displaced with respect to each other, indicating that the fluorescence dyes, do indeed target different locations.

The preliminary FDPM images indicate that there certainly exists room for improvement and a need to optimize the experimental protocol for the acquisition of frequency-domain data in order to improve contrast, especially in the images of phase-lag. Nonetheless, the results of this section demonstrate that a frequency-domain

imaging technique can be used to efficiently image fluorescence laden tumors in small animals. In addition to providing a method to reject ambient light, frequency-domain imaging provides a convenient way to extract temporal information vis-à-vis fluorophore decay kinetics. Finally, the results suggest that *in vivo* FDPM data for tomographic reconstruction may be obtained using an expanded or planar illumination geometry and area detection. Typically, measurements of FDPM are obtained using a point illumination – point detection scheme, where area images are compiled after scanning a single detector across a region of interest and building the image point-by-point. However, a scanning method utilizing point illumination – point detection is a highly inefficient technique to elicit fluorescence from submerged or deeply embedded fluorophores and area measurements can provide a great deal more information or data.[64,118] Current efforts concentrate on the tomographic reconstruction of area measurements of FDPM following planar illumination.[117]

9. SUMMARY AND CONCLUSIONS

A new optical imaging modality has been developed for *in vivo* clinical imaging of near-infrared fluorescence resulting from fluorescent contrast agents specifically targeted to molecular markers of carcinoma. The imaging system is comprised of an intensified charge-coupled device (ICCD) for the detection of ultra-low levels of re-emitted fluorescence following the delivery of excitation light provided by a laser diode whose monochromatic output has been expanded to illuminate an area of the tissue surface. The ICCD detection system is capable of both continuous wave and frequency-domain modes of operation. Furthermore, the intensified-detection allows for sub-second exposure times, permitting the acquisition of dynamic fluorescence imaging immediately following administration of the contrast agent.

The work presented herein also demonstrates the capacity to obtain time-resolved measurements, or measurements obtained in the frequency-domain. In addition to mean signal intensity, frequency-domain measurements provide information regarding the temporal propagation of fluorescent photon density waves. While this information may not be heeded at the current time given that a plethora of information is available using simpler continuous-wave technology, it nonetheless motivates the next step in near-infrared fluorescence optical imaging. Continuous wave optical imaging may be well suited for small animal imaging studies geared toward the development of novel diagnostic imaging agents and therapeutic drugs; however, the future of optical imaging for the detection of heterogeneous large volumes necessitates the use of a technology capable of deep-tissue imaging. Thus, the work presented in this dissertation also serves

to motivate the development of a frequency-domain fluorescence imaging system for use on human subjects.

A summary of the important findings presented in this dissertation include:

1. Frequency-domain photon migration measurements obtained from the surface of homogenous turbid media may be used to accurately determine the absorption and reduced scattering coefficients characteristic of the media. The absorption and reduced scattering coefficients are determined least accurately when relative measurements of average light intensity I_{DC}^{rel} are employed either alone or in a combination with relative modulation amplitude data I_{AC}^{rel} and/or relative phase shift data θ^{rel}. The absorption and reduced scattering coefficients may be found accurate to within 15% and 11%, respectively, of the values obtained from standard single-pixel measurements when θ^{rel} measurements are employed alone or in combination with I_{AC}^{rel} data.

2. Unlike dynamic fluorescence images of indocyanine green (ICG), dynamic fluorescence images of carotene-conjugated 2-devinyl-2- (1-hexyloxyethyl) pyropheophorbide (HPPH-car) may be used discriminate spontaneous canine adenocarcinoma from normal mammary tissue. Upon collecting time-dependent fluorescence images at the tissue surface overlying both normal and diseased tissue volumes immediately following intravenous administration of fluorescent contrast agent into the canine, and fitting these images to a pharmacokinetic model describing the uptake (wash-in) and release (wash-out) of fluorescent dye,

the pharmacokinetics of fluorescent dye may be spatially determined. Mapping the fluorescence intensity owing to ICG indicates that the dye acts as a blood pool or blood persistent agent, for the model parameters show no difference in the ICG uptake rates between normal and diseased tissue regions. In contrast, HPPH-car pharmacokinetics illustrated active uptake into diseased tissues, perhaps owing to the overexpression of LDL receptors associated with the malignant cells.

3. Dynamic fluorescence intensity measurements obtained from a murine Kaposi's sarcoma model immediately following the intravenous injection of an integrin-targeting cyanine dye conjugate, RGD-Cy5.5 may be used in conjunction with a pharmacokinetic model to determine kinetic properties of the conjugate dye. The results indicate that the conjugate dye behaves similarly in normal tissue to the free Cy5.5 dye while it possesses increased uptake in tumor tissue. Furthermore, the rate constant governing the cellular uptake of the conjugate dye within the Kaposi's sarcoma tumor tissue was estimated to have a value of 0.16-sec^{-1}. Moreover, based on the results one may speculate that the integrin receptor turnover occurs approximately every 24-hours. The findings further suggest that if dynamic fluorescence imaging is combined with a suitable pharmacokinetic model describing dye distribution throughout the body, it may be possible to describe molecular phenomena such as binding specificity, degree of receptor expression, and receptor turnover rate.

4. The specificity of a novel EGF-Cy5.5 fluorescent optical probe for epidermal growth factor receptor (EGFr) may be assessed using continuous-wave fluorescence imaging accomplished via an ICCD camera. Fluorescence imaging performed on mice with MDA-MB-468 cancer, known to overexpress EGFr, confirms no favorable binding to tumor by the free dyes ICG and Cy5.5. In contrast, EGF-Cy5.5 exhibits selective accumulation in the MDA-MB-468 tumor. Moreover, tumor uptake of EGF-Cy5.5 is blocked by pre-injection of anti-EGFr antibody C225, further demonstrating specificity of the targeted contrast agent. Furthermore, fluorescence due to the EGF-Cy5.5 conjugate dye may be detected at the site of the MDA-MB-468 tumor, for a period of up to 192-hrs following the administration of the contrast agent.

REFERENCES

1. American Cancer Society, *Cancer Prevention & Early Detection Facts & Figures 2003.* Atlanta, GA (2002).
2. American Cancer Society, *Breast Cancer Facts & Figures 2003-2004.* Atlanta, GA (2003).
3. H. W. Lim and N. A. Soter, *Clinical Photomedicine*, Dekker, New York, 1993.
4. T. L. Troy, D. L. Page and E. M. Sevick-Muraca, "Optical properties of normal and diseased breast tissues: prognosis for optical mammography," *J. Biomed. Opt.* **1**(3), 342-355 (1996).
5. D. J. Hawrysz and E. M. Sevick-Muraca, "Developments toward diagnostic breast cancer imaging using near-infrared optical measurements and fluorescent contrast agents," *Neoplasia* **2**(5), 388-417 (2000).
6. E. M. Sevick-Muraca, E. Kuwana, A. Godavarty, J. P. Houston, A. B. Thompson and R. Roy, "Near infrared fluorescence imaging and spectroscopy in random media and tissues," in *Biomedical Photonics Handbook*, T. Vo-Dinh, Ed. CRC Press, Boca Raton, FL (2003).
7. J. Lakowicz, *Principles of Fluorescence Spectroscopy*, Plenum Press, New York, (1983).
8. D. C. Harris, *Quantitative Chemical Analysis*, W.H. Freeman and Company, New York, (1995).
9. E. M. Sevick-Muraca and C. L. Burch, "Origin of phosphorescence signals re-emitted from tissues," *Opt. Lett.* **19**(23), 1928-1930 (1994).

10. D. K. F. Meijer, B. Weert and G. A. Vermeer, "Pharmacokinetics of biliary excretion in man VI. Indocyanine green," *Eur. J. Clin. Pharmacol.* **35**(3), 295-303 (1988).

11. J. Caeser, S. Shaldon, L. Chiandussi, L. Guevera and S. Sherlock, "The use of indocyanine green in the measurement of hepatic blood flow and as a test of hepatic function," *Clin. Sci.* **21**, 43-57 (1961).

12. Akorn, Inc., "Indocyanine green," <http://www.akorn.com/html/IcGreen_Frame.html> (November 5, 2003).

13. J. F. Zhou, M. P. Chin and S. A. Schafer, "Aggregation and degradation of indocyanine green," *Proc. SPIE* **2128**, 495-505 (1994).

14. E. M. Sevick-Muraca, G. Lopez, J. S. Reynolds, T. L. Troy and C. L. Hutchinson, "Fluorescence and absorption contrast mechanisms for biomedical optical imaging using frequency-domain techniques," *Photochem. Photobiol.* **66**(1), 55-64 (1997).

15. S. Mujumdar, R. Mujumdar, C. M. Grant and A. Waggoner, "Cyanine-labeling reagents: sulfobenzindocyanine succinimidyl esters," *Bioconjugate Chem.* **7**(3), 356-362 (1996).

16. Amersham Biosciences, *BioDirectory - Product Catalog.* Piscataway, NJ (2003).

17. R. Rajagopalan, P. Uetrecht, J. Bugaj, S. Achilefu and R. Dorshow, "Stabilization of the optical tracer agent indocyanine green using noncovalent interactions," *Photochem. Photobiol.* **71**(3), 347-350 (2000).

18. S. Ito, N. Muguruma, Y. Kakehashi, S. Hayashi, S. Okamura, H. Shibata, T. Okahisa, M. Kanamori, S. Shibamura, K. Takesako, M. Nozawa, K. Ishida and M.

Shiga, "Development of fluorescence-emitting antibody labeling substance by near-infrared ray excitation," *Bioorg. Med. Chem. Lett.* **5**(22), 2689-2694 (1995).

19. T. Hirata, H. Kogiso, K. Morimoto, S. Miyamoto, H. Taue, S. Sano, N. Muguruma, S. Ito and Y. Nagao, "Synthesis and reactivities of 3-indocyanine-green-acyl-1,3-thiazolidine-2-thione (ICG-ATT) as a new near-infrared fluorescent-labeling reagent," *Bioorg. Med. Chem. Lett.* **6**(11), 2179-2184 (1998).
20. R. Mujumdar, L. A. Ernst, S. Mujumdar, C. J. Lewis and A. Waggoner, "Cyanine dye labeling reagents: sulfoindocyanine succinimidyl esters," *Bioconjugate Chem.* **4**(2), 105-111 (1993).
21. B. Ballou, G. Fisher, A. Waggoner, D. Farkas, J. Reiland, R. Jaffe, R. Mujumdar, S. Mujumdar and T. Hakala, "Tumor labeling in vivo using cyanine-conjugated monoclonal antibodies," *Cancer Immunol. Immunother.* **41**(4), 257-263 (1995).
22. A. Becker, C. Hessenius, K. Licha, B. Ebert, U. Sukowski, W. Semmler, B. Wiedenmann and C. Grotzinger, "Receptor-targeted optical imaging of tumors with near-infrared fluorescent ligands," *Nat. Biotechnol.* **19**(4), 327-331 (2001).
23. S. Folli, G. Wagnieres, A. Pelegrin, J. M. Calmes, D. Braichotte, F. Buchegger, Y. Chalandon, N. Hardman, C. H. Heusser, J. C. Givel, G. Chapuis, A. Chatelain, H. van den Bergh and J. Mach, "Immunophotodiagnosis of colon carcinomas in patients injected with fluoresceinated chimeric antibodies against carcinoembryonic antigen," *Proc. Natl. Acad. Sci. USA* **89**(17), 7973-7977 (1992).
24. S. Folli, P. Westermann, D. Braichotte, A. Pelegrin, G. Wagnieres, H. van den Bergh and J. Mach, "Antibody-indocyanin conjugates for immunophotodetection of

human squamous cell carcinoma in nude mice," *Cancer Res.* **54**(10), 2643-2649 (1994).

25. N. S. Soukos, M. R. Hamblin, S. Keel, R. L. Fabian, T. F. Deutsch and T. Hasan, "Epidermal growth factor receptor-targeted immunophotodiagnosis and photoimmunotherapy of oral precancer in vivo," *Cancer Res.* **61**(11), 4490-4496 (2001).
26. S. J. Goldsmith, "Receptor imaging: competitive or complementary to antibody imaging?," *Semin. Nucl. Med.* **27**(2), 85-93 (1997).
27. S. Achilefu, J. Bugaj, R. Dorshow, H. N. Jimenez and R. Rajogopalan, "New approach to optical imaging of tumors," *Proc. SPIE* **4259**, 110-114 (2001).
28. S. Achilefu, R. Dorshow, J. Bugaj and R. Rajogopalan, "Tumor specific fluorescent contrast agents," *Proc. SPIE* **3917**, 80-86 (2000).
29. R. K. Jain, "Barriers to drug delivery in solid tumors," *Sci. Am.* **271**(1), 58-65 (1994).
30. J. Bugaj, S. Achilefu, R. Dorshow and R. Rajogopalan, "Novel fluorescent contrast agents for optical imaging of in vivo tumors based on a receptor-targeted dye-peptide conjugate platform," *J. Biomed. Opt.* **6**(2), 122-133 (2001).
31. A. Becker, B. Riefke, B. Ebert, U. Sukowski, H. Rinneberg, W. Semmler and K. Licha, "Macromolecular contrast agents for optical imaging of tumors: comparison of indotricarbocyanine-labeled human serum albumin and transferrin," *Photochem. Photobiol.* **72**(2), 234-241 (2000).

32. A. Zaheer, R. E. Lenkinski, A. Mahmood, A. G. Jones, L. C. Cantley and J. V. Frangioni, "In vivo near-infrared fluorescence imaging of osteoblastic activity," *Nat. Biotechnol.* **19**(20), 1148-1154 (2001).

33. R. Weissleder, C. Tung, U. Mahmood and A. Bogdanov, "In vivo imaging of tumors with protease-activated near-infrared fluorescent probes," *Nat. Biotechnol.* **17**(4), 375-378 (1999).

34. K. Licha, A. Becker, F. Kratz and W. Semmler, "New contrast agents for optical imaging: acid-cleavable conjugates of cyanine dyes with biomolecules," *Proc. SPIE* **3600**, 29-35 (1999).

35. C. Bremer, C. Tung and R. Weissleder, "In vivo molecular target assessment of matrix metalloproteinase inhibition," *Nat. Med.* **7**(6), 743-748 (2001).

36. A. U. Chen and E. M. Sevick-Muraca, "On the use of phosphorescent and fluorescent dyes for lifetime-based imaging within tissues," in *Optical Tomography and Spectroscopy of Tissue: Theory, Instrumentation, Model and Human Studies II*, B. Chance and A.A. Alfano, Eds., pp. 129-138, SPIE Press, Bellingham, WA (1997).

37. J. P. Houston, A. B. Thompson, M. Gurfinkel and E. M. Sevick-Muraca, "Sensitivity and depth penetration of continuous wave versus frequency-domain photon migration near-infrared fluorescence contrast-enhanced imaging," *Photochem. Photobiol.* **77**(4), 420-430 (2003).

38. M. J. Eppstein, D. J. Hawrysz, A. Godavarty and E. M. Sevick-Muraca, "Three-dimensional, Bayesian image reconstruction from sparse and noisy data sets: near-

infrared fluorescence tomography," *Proc. Natl. Acad. Sci. USA* **99**(15), 9619-9624 (2002).

39. A. Godavarty, M. J. Eppstein, C. Zhang, S. Theru, A. B. Thompson, M. Gurfinkel and E. M. Sevick-Muraca, "Fluorescence-enhanced optical imaging in large tissue volumes using a gain-modulated ICCD camera,"*Phys. Med. Biol.* **48**(12), 1701-1720 (2003).
40. J. Lee and E. M. Sevick-Muraca, "Three-dimensional fluorescence enhanced optical tomography using referenced frequency-domain photon migration measurements at emission and excitation wavelengths," *J. Opt. Soc. Am., A* **19**(4), 759-771 (2002).
41. R. Roy, A. Godavarty and E. M. Sevick-Muraca, "Fluorescence-enhanced optical tomography using referenced measurements of heterogeneous media.," *IEEE Trans. Med. Imaging* **22**(7), 824-836 (2003).
42. Roper Scientific, Inc., *Technical Note: Introduction to Image Intensifiers for Scientific Imaging.* Tucson, AZ (2002).
43. C. B. Johnson and L. D. Owen, "Image tube intensified electronic imaging," in *Handbook of Optics*, M. Bass, E.W. van Stryland, D.R. Williams and W.L. Wolfe, Eds., pp. 21.21-21.32, McGraw-Hill, Inc., New York (1995).
44. ITT Industries - Night Vision, *Technical Specifications: Non-Inverting Image Intensifier, Gen 3, 18mm for Special Low-Light-Level Applications - FS9910 Series.* Roanoke, VA (2001).
45. ITT Industries - Night Vision, *FS9910C - Data Sheet* (Roanoke, VA 2001).

46. Scientific Imaging Technologies, Inc., *SITe 1024 x 1024 Scientific-Grade CCD* (Beaverton, OR 1994).

47. Roper Scientific, Inc., *Technical Note: Comparison of Lens-Coupled and Fiberoptic-Coupled ICCD Cameras* (Tucson, AZ 2000).

48. PCO Computer Optics, *Smear in CCD-Sensors* (Kelheim, Germany 2001).

49. D. Dam, Roper Scientific, Inc., *Certificate of Performance - model 7495-0001* (Tucson, AZ 2001).

50. Roper Scientific, Inc., "Roper Scientific - Encyclopedia," <http://www.roperscientific.com/library_encyclopedia.shtml> (October 29, 2003).

51. D. Dam, Roper Scientific, Inc., *Certificate of Performance - model CH350L.* Tucson, AZ (2001).

52. PCO Computer Optics, *Noise - General.* Kelheim, Germany (2001).

53. Kaiser Optical Systems, Inc., *Holographic Notch Plus Filter: Data Sheet part no. HNPF-660.0-2.0.* Ann Arbor, MI (2001).

54. Kaiser Optical Systems, Inc., *Holographic Notch Plus Filter: Data Sheet part no. HNPF-785.0-2.0.* Ann Arbor, MI (2001).

55. CVI Laser Corporation, *Laser Optics and Coatings - Optical Filter Specifications.* Albuquerque, NM (1998).

56. T. E. French, E. Gratton and J. S. Maier, "Frequency domain imaging of thick tissues using a CCD," *Proc. SPIE* **1640**, 254-261 (1992).

57. A. B. Thompson and E. M. Sevick-Muraca, "Near-infrared fluorescence contrast-enhanced imaging with intensified charge-coupled device homodyne detection: measurement precision and accuracy," *J. Biomed. Opt.* **8**(1), 111-120 (2003).

58. G. Wagnieres, J. Mizeret, A. Studzinski and H. van den Bergh, "Frequency-domain fluorescence lifetime imaging for endoscopic clinical cancer photodetection: apparatus design and preliminary results," *J. Fluoresc.* **7**(1), 75-83 (1997).

59. J. Lakowicz and K. Berndt, "Lifetime-selective fluorescence imaging using an rf sensitive camera," *Rev. Sci. Instrum.* **62**(7), 1727-1734 (1991).

60. J. S. Reynolds, T. L. Troy and E. M. Sevick-Muraca, "Multipixel techniques for frequency-domain photon migration imaging," *Biotechnol. Progr.* **13**(5), 669-680 (1997).

61. Photonic Research Systems, "Genomics, proteomics, microarray and PSP imaging solutions with fluorescence lifetime imaging," <http://www.photonic-research.freeserve.co.uk/> (November 5, 2003).

62. P. Horowitz and W. Hill, *The Art of Electronics*, Cambridge University Press, New York, 1995.

63. T. L. Troy, *Biomedical optical imaging with frequency-domain photon migration measurements: experiments and numerical image reconstructions*, Ph.D. dissertation. Purdue University, West Lafayette, IN (1997).

64. A. B. Thompson, *Development of a new optical imaging modality for detection of fluorescence-enhanced disease*, Ph.D. dissertation. Texas A&M University, College Station, TX (2003).

65. M. G. Nichols, E. L. Hull and T. H. Foster, "Design and testing of a white-light, steady-state diffuse reflectance spectrometer for determination of optical properties of highly scattering systems," *Appl. Opt.* **36**(1), 93-104 (1997).

66. T. J. Farrell, M. S. Patterson and B. C. Wilson, "A diffusion theory model of spatially resolved, steady-state diffuse reflectance for the noninvasive determination of tissue optical properties in vivo," *Med. Phys.* **19**(4), 879-888 (1992).

67. R. M. P. Doornbos, R. Lang, M. C. Aalders, F. W. Cross and H. J. C. M. Sterenborg, "The determination of in vivo human tissue optical properties and absolute chromophore concentrations using spatially resolved steady-state diffuse reflectance spectroscopy," *Phys. Med. Biol.* **44**(4), 967-981 (1999).

68. A. Kienle and M. S. Patterson, "Improved solutions of the steady-state and the time-resolved diffusion equations for reflectance from a semi-infinite turbid medium," *J. Opt. Soc. Am., A* **14**(1), 246-254 (1997).

69. M. S. Patterson, B. Chance and B. C. Wilson, "Time resolved reflectance and transmittance for the noninvasive measurement of tissue optical properties," *Appl. Opt.* **28**(12), 2331-2336 (1989).

70. J. B. Fishkin, P. T. C. So, A. E. Cerussi, S. Fantini, M. A. Franceschini and E. Gratton, "Frequency-domain method for measuring spectral properties in multiple-scattering media: methemoglobin absorption spectrum in a tissuelike phantom," *Appl. Opt.* **34**(7), 1143-1155 (1995).

71. B. J. Tromberg, L. O. Svaasand, T. T. Tsay and R. C. Haskell, "Properties of photon density waves in multiple-scattering media," *Appl. Opt.* **32**(4), 607-616 (1993).

72. M. Gerken and G. W. Faris, "Frequency-domain immersion technique for accurate optical property measurements of turbid media," *Opt. Lett.* **24**(23), 1726-1728 (1999).

73. S. Fantini, M. A. Franceschini, J. B. Fishkin, B. Barbieri and E. Gratton, "Quantitative determination of the absorption spectra of chromophores in strongly scattering media: a light-emitting-diode based technique," *Appl. Opt.* **33**(22), 5204-5213 (1994).

74. Z. Sun, Y. Huang and E. M. Sevick-Muraca, "Precise analysis of frequency domain photon migration measurement for characterization of concentrated colloidal suspensions," *Rev. Sci. Instrum.* **73**(2), 383-393 (2002).

75. B. J. Tromberg, R. C. Haskell, S. J. Madsen and L. O. Svaasand, "Characterization of tissue optical properties using photon density waves," *Comments Mol. Cell. Biophys.* **8**(6), 359-386 (1995).

76. S. Fantini, M. A. Franceschini and E. Gratton, "Semi-infinite-geometry boundary problem for light migration in highly scattering media: a frequency-domain study in the diffusion approximation," *J. Opt. Soc. Am., B* **11**(10), 2128-2138 (1994).

77. J. B. Fishkin, O. Coquoz, E. R. Anderson, M. Brenner and B. J. Tromberg, "Frequency-domain photon migration measurements of normal and malignant tissue optical properties in a human subject," *Appl. Opt.* **36**(1), 10-20 (1997).

78. A. Kienle and M. S. Patterson, "Determination of the optical properties of semi-infinite turbid media from frequency-domain reflectance close to the source," *Phys. Med. Biol.* **42**(9), 1801-1819 (1997).

79. R. C. Haskell, L. O. Svaasand, T. T. Tsay, T. C. Feng, M. S. McAdams and B. J. Tromberg, "Boundary conditions for the diffusion equation in radiative transfer," *J. Opt. Soc. Am., A* **11**(10), 2727-2741 (1994).

80. K. M. Yoo, F. Liu and R. R. Alfano, "When does the diffusion approximation fail to describe photon transport in random media?," *Phys. Rev. Lett.* **64**(22), 2647-2650 (1990).

81. H. J. van Staveren, C. J. M. Moes, J. van Marle, S. A. Prahl and M. J. C. van Gemert, "Light scattering in Intralipid-10% in the wavelength range of 400-1100 nm," *Appl. Opt.* **30**(31), 4507-4514 (1991).

82. S. T. Flock, S. L. Jacques, B. C. Wilson, W. M. Star and M. J. C. van Gemert, "Optical properties of Intralipid: a phantom medium for light propagation studies," *Lasers Surg. Med.* **12**(5), 510-519 (1992).

83. S. J. Madsen, M. S. Patterson and B. C. Wilson, "The use of India ink as an optical absorber in tissue-simulating phantoms,"*Phys. Med. Biol.* **37**(4), 985-993 (1992).

84. I. Rokahr, S. Andersson-Engels, S. Svanberg, M. D'Hallewin, L. Baert, I. Wang and K. Svanberg, "Optical detection of human urinary bladder carcinoma utilising tissue autofluorescence and protoporphyrin IX-induced fluorescence following low dose ALA instillation," *Proc. SPIE* **2627**, 2-12 (1995).

85. A. Nilsson, C. S. von Holstein, S. Andersson-Engels, R. Willen, B. Walther and K. Svanberg, "Clinical detection studies of Barrett's metaplasia and oesophageal adenocarcinoma by means of laser-induced fluorescence," *Proc. SPIE* **2627**, 49-56 (1995).

86. C. af Klinteberg, A. M. K. Enejder, I. Wang, S. Andersson-Engels, S. Svanberg and K. Svanberg, "Kinetic fluorescence studies of 5-aminolaevulinic acid induced protoporphyrin IX accumulation in basal cell carcinomas," *J. Photochem. Photobiol., B* **49**(2-3), 120-128 (1999).

87. T. J. Farrell, R. P. Hawkes, M. S. Patterson and B. C. Wilson, "Modeling of photosensitizer fluorescence emission and photobleaching for photodynamic therapy dosimetry," *Appl. Opt.* **37**(31), 7168-7183 (1998).

88. W. R. Potter, D. A. Bellnier and T. J. Dougherty, "Optical methods for in-vivo pharmacokinetics," *Proc. SPIE* **1645**, 166-170 (1992).

89. I. J. Bigio, J. R. Mourant and G. Los, "Elastic-scattering spectroscopy for quantitative measurement of chemotherapy and PDT drug concentrations in vivo," *Proc. SPIE* **3658**, 26-30 (1999).

90. G. A. Wagnieres, W. M. Star and B. C. Wilson, "In vivo fluorescence spectroscopy and imaging for oncological applications," *Photochem. Photobiol.* **68**(5), 603-632 (1998).

91. J. S. Reynolds, T. L. Troy, R. H. Mayer, A. B. Thompson, D. J. Waters, K. K. Cornell, P. W. Snyder and E. M. Sevick-Muraca, "Imaging of spontaneous canine

mammary tumors using fluorescent contrast agents," *Photochem. Photobiol.* **70**(1), 87-94 (1999).

92. X. Li, B. Chance and A. G. Yodh, "Fluorescence heterogeneities in turbid media: limits for detection, characterization, and comparison with absorption," *Appl. Opt.* **37**(28), 6833-6844 (1998).
93. R. Cubeddu, G. Canti, A. Pifferi, P. Taroni and G. Valentini, "Fluorescence lifetime imaging of experimental tumors in hematoporphyrin derivative-sensitized mice," *Photochem. Photobiol.* **66**(2), 229-236 (1997).
94. T. Hasan and J. A. Parrish, "Photodynamic therapy of cancer," in *Cancer Medicine*, J.F. Holland, E. Frei, R.C. Bast, D.W. Kufe, D.L. Morton and R.R. Weichselbaum, Eds., pp. 739-751, Williams & Wilkins, Philadelphia (1997).
95. M. Gurfinkel, A. B. Thompson, W. Ralston, T. L. Troy, A. L. Moore, T. A. Moore, J. D. Gust, D. Tatman, J. S. Reynolds, B. Muggenburg, K. Nikula, R. Pandey, R. H. Mayer, D. J. Hawrysz and E. M. Sevick-Muraca, "Pharmacokinetics of ICG and HPPH-car for the detection of normal and tumor tissue using fluorescence, near-infrared reflectance imaging: A case study," *Photochem. Photobiol.* **72**(1), 94-102 (2000).
96. K. A. Schafer, G. Kelly, R. Schrader, W. C. Griffith, B. Muggenburg, L. A. Tierney, J. F. Lechner, E. B. Janovitz and F. F. Hahn, "A canine model of familial mammary gland neoplasia," *Vet. Pathol.* **35**(3), 168-177 (1998).
97. R. Pandey, A. B. Sumlin, S. Constantine, M. Aoudia, W. R. Potter, D. A. Bellnier, B. W. Henderson, M. A. Rodgers, K. M. Smith and T. J. Dougherty, "Alkyl ether

analogs of chlorophyll-a derivatives. 1. Synthesis, photophysical properties and photodynamic efficacy," *Photochem. Photobiol.* **64**(1), 194-204 (1996).

98. B. W. Henderson, D. A. Bellnier, W. R. Greco, A. Sharma, R. Pandey, L. Vaughan, K. Weishaupt and T. J. Dougherty, "An in vivo quantitative structure-activity relationship for a congeneric series of pyropheophorbide derivatives as photosensitizers for photodynamic therapy," *Cancer Res.* **57**(18), 4000-4007 (1997).
99. K. Furukawa, D. H. Crean, T. S. Mang, H. Kato and T. J. Dougherty, "Fluorescence detection of premalignant, malignant, and micrometastatic disease using hexylpyropheophorbide," *Proc. SPIE* **2371**, 510-514 (1995).
100. E. M. Sevick, J. Lakowicz, H. Szmacinski, K. Nowaczyk and M. Johnson, "Frequency domain imaging of absorbers obscured by scattering," *J. Photochem. Photobiol., B* **16**(2), 169-185 (1992).
101. M. J. Eppstein, D. E. Dougherty, T. L. Troy and E. M. Sevick-Muraca, "Biomedical optical tomography using dynamic parameterization and Bayesian conditioning on photon migration measurements," *Appl. Opt.* **38**(10), 2138-2150 (1999).
102. D. Y. Paithankar, A. U. Chen, B. W. Pogue, M. S. Patterson and E. M. Sevick-Muraca, "Imaging of fluorescent yield and lifetime from multiply scattered light re-emitted from tissues and other random media," *Appl. Opt.* **36**(10), 2260-2272 (1997).
103. O. M. Fischer, S. Streit, S. Hart and A. Ullrich, "Beyond Herceptin and Gleevec," *Curr. Opin. Chem. Biol.* **7**(4), 490-495 (2003).

104. R. Abou-Jawde, T. Choueiri, C. Alemany and T. Mekhail, "An overview of targeted treatments in cancer," *Clin. Ther.* **25**(8), 2121-2137 (2003).

105. J. A. Kim, "Targeted therapies for the treatment of cancer," *Am. J. Surg.* **186**(3), 264-268 (2003).

106. R. Roskoski, Jr., "STI-571: an anticancer protein-tyrosine kinase inhibitor," *Biochem. Biophys. Res. Commun.* **309**(4), 709-717 (2003).

107. R. Schiffelers, G. Koning, T. ten Hagen, M. Fens, A. Schraa, A. Janssen, R. Kok, G. Molema and G. Storm, "Anti-tumor efficacy of tumor vasculature-targeted liposomal doxorubicin," *J. Controlled Release* **91**(1-2), 115-122 (2003).

108. X. Wen, Q. Wu, S. Ke, L. Ellis, C. Charnsangavej, A. Delpassand, S. Wallace and C. Li, "Conjugation with (111)In-DTPA-poly(ethylene glycol) improves imaging of anti-EGF receptor antibody C225," *J. Nucl. Med.* **42**(10), 1530-1537 (2001).

109. X. Wen, Q. Wu, Y. Lu, Z. Fan, C. Charnsangavej, S. Wallace, D. Chow and C. Li, "Poly(ethylene glycol)-conjugated anti-EGF receptor antibody C225 with radiometal chelator attached to the termini of polymer chains," *Bioconjugate Chem.* **12**(4), 545-553 (2001).

110. S. Ke, X. Wen, M. Gurfinkel, C. Charnsangavej, Z. Fan, S. Wallace, E. M. Sevick-Muraca and C. Li, "Near infrared optical imaging of epidermal growth factor receptor in a breast cancer xenografts," *Cancer Res.* **63**(22), 7870-7875 (2003).

111. D. Cuccia, F. Bevilacqua, A. Durkin, S. Merritt, B. J. Tromberg, G. Gulsen, H. Yu, J. Wang and O. Nalcioglu, "In vivo quantification of optical contrast agent

dynamics in rat tumors by use of diffuse optical spectroscopy with magnetic resonance imaging coregistration," *Appl. Opt.* **42**(16), 2940-2950 (2003).

112. I. H. Segel, *Biochemical Calculations*, John Wiley & Sons, New York, (1976).
113. J. S. Ross, P. Kaur, C. E. Sheehan, H. A. G. Fisher, J. Ronald A. Kaufman and B. V. S. Kallakury, "Prognostic significance of matrix metalloproteinase 2 and tissue inhibitor of metalloproteinase 2 expression in prostate cancer," *Mod. Pathol.* **16**(3), 198-205 (2003).
114. T. S. Udayakumar, M. L. Chen, E. L. Bair, D. C. v. Bredow, A. E. Cress, R. B. Nagle and G. T. Bowden, "Membrane type-1-matrix metalloproteinase expressed by prostate carcinoma cells cleaves human laminin-5 β3 chain and induces cell migration," *Cancer Res.* **63**(9), 2292-2299 (2003).
115. J. A. Nemeth, R. Yousif, M. Herzog, M. Che, J. Upadhyay, B. Shekarriz, S. Bhagat, C. Mullins, R. Fridman and M. L. Cher, "Matrix metalloproteinase activity, bone matrix turnover, and tumor cell proliferation in prostate cancer bone metastasis," *J. Natl. Cancer Inst.* **94**(1), 17-25 (2002).
116. *Radiation Protection Dosimetry - Radionuclide and Radiation Protection Data Handbook*, Nuclear Technology Publishing, Kent, England, (1998).
117. R. Roy and E. M. Sevick-Muraca, "Fluorescence-enhanced optical tomography with planar wave illumination," *Appl. Opt.*, submitted (2003).
118. A. B. Thompson, D. J. Hawrysz and E. M. Sevick-Muraca, "Near-infrared fluorescence contrast-enhanced imaging with area illumination and area detection: the forward imaging problem," *Appl. Opt.* **42**(19), 4125-4136 (2003).

119. J. J. Duderstadt and L. J. Hamilton, *Nuclear Reactor Analysis*, John Wiley & Sons, Inc., New York, (1976).

120. G. E. Roberts and H. Kaufman, *Table of Laplace Transforms*, W.B. Saunders Company, Philadelphia, (1966).

APPENDIX A: DIFFUSION APPROXIMATION TO THE RADIATIVE TRANSPORT EQUATION

The propagation of light through an absorbing and scattering medium is described by the radiative transport equation (RTE). Assuming that photons travel at the same speed or energy through a homogeneous medium, the RTE describing the accumulation and loss of photons within the medium is given by:[119]

$$\frac{1}{c}\frac{\partial\varphi\left(\mathbf{r},\hat{\mathbf{\Omega}},t\right)}{\partial t}+\hat{\Omega}\cdot\nabla\varphi\left(\mathbf{r},\hat{\mathbf{\Omega}},t\right)+\left(\mu_s+\mu_a\right)\varphi\left(\mathbf{r},\hat{\mathbf{\Omega}},t\right)= \mu_s\int_{4\pi}p\left(\hat{\mathbf{\Omega}}'\rightarrow\hat{\mathbf{\Omega}}\right)\varphi\left(\mathbf{r},\hat{\mathbf{\Omega}}',t\right)d\hat{\mathbf{\Omega}}'+s\left(\mathbf{r},\hat{\mathbf{\Omega}},t\right), \quad \text{(A.1)}$$

where $\varphi\left(\mathbf{r},\hat{\mathbf{\Omega}},t\right)$ represents the angular flux of photons in direction $\hat{\mathbf{\Omega}}$ at position $\mathbf{r}$ at time t; $s\left(\mathbf{r},\hat{\mathbf{\Omega}},t\right)$ represents the photon source in direction $\hat{\mathbf{\Omega}}$ at position $\mathbf{r}$ at time t; c is the speed of light within the medium, and; $p\left(\hat{\mathbf{\Omega}}'\rightarrow\hat{\mathbf{\Omega}}\right)$ is the probability that scattering events carry photons from $\hat{\mathbf{\Omega}}'$ into $\hat{\mathbf{\Omega}}$. Integrating Eq. (B.1) over all solid angles yields:

$$\frac{1}{c}\frac{\partial\Phi\left(\mathbf{r},t\right)}{\partial t}+\nabla\cdot\mathbf{J}\left(\mathbf{r},t\right)+\mu_a\Phi\left(\mathbf{r},t\right)=S\left(\mathbf{r},t\right), \quad \text{(A.2)}$$

where $\Phi\left(\mathbf{r},t\right)$, $\mathbf{J}\left(\mathbf{r},t\right)$, and $S\left(\mathbf{r},t\right)$ are the angle-independent fluence rate, current density, and angle-independent photon source, respectively, and are represented by:

$$\Phi\left(\mathbf{r},t\right)=\int_{4\pi}\varphi\left(\mathbf{r},\hat{\mathbf{\Omega}},t\right)d\hat{\Omega}, \quad \text{(A.3)}$$

$$\mathbf{J}\left(\mathbf{r},t\right)=\int_{4\pi}\varphi\left(\mathbf{r},\hat{\mathbf{\Omega}},t\right)\hat{\Omega}\,d\hat{\Omega}, \quad \text{(A.4)}$$

$$S(\mathbf{r},t)=\int_{4\pi} s\left(\mathbf{r},\hat{\mathbf{\Omega}},t\right)d\hat{\Omega}. \tag{A.5}$$

Eq. (A.2) contains two dependent variables, namely, the fluence rate, $\Phi(\mathbf{r},t)$, and the current density, $\mathbf{J}(\mathbf{r},t)$. As a result, a second expression for $\mathbf{J}(\mathbf{r},t)$ is required. To obtain this second expression, the angular photon flux is first approximated as the sum of an isotropic fluence rate and a directional flux:

$$\varphi\left(\mathbf{r},\hat{\mathbf{\Omega}},t\right)\cong\frac{1}{4\pi}\Phi(\mathbf{r},t)+\frac{3}{4\pi}\mathbf{J}(\mathbf{r},t)\cdot\hat{\mathbf{\Omega}}. \tag{A.6}$$

The assumption is equivalent to saying that photons are multiply scattered before being absorbed or detected, which holds true when $\mu_s >> \mu_a$. This expression for the angular photon flux, Eq. (A.6), is next substituted into Eq. (A.1), and the resulting expression is multiplied by $\hat{\mathbf{\Omega}}$ and integrated over all solid angles to yield:

$$\frac{1}{c}\frac{\partial\mathbf{J}(\mathbf{r},t)}{\partial t}+\frac{1}{3}\nabla\Phi(\mathbf{r},t)+\left[\mu_a+(1-g)\mu_s\right]\mathbf{J}(\mathbf{r},t)=S_1(\mathbf{r},t) \tag{A.7}$$

where *g* is the average cosine of the scattering angle, and

$$S_1(\mathbf{r},t)=\int_{4\pi} s\left(\mathbf{r},\hat{\mathbf{\Omega}},t\right)\hat{\Omega}\,d\hat{\Omega}. \tag{A.8}$$

Further, Eq. (A.7) can be reduced by assuming that the photon source is isotropic, and the time rate of change in current density is much slower than the collision frequency. Mathematically, these assumptions are stated as:

$$s\left(\mathbf{r},\hat{\mathbf{\Omega}},t\right)\cong s(\mathbf{r},t)\Rightarrow S_1=0, \tag{A.9}$$

$$\frac{\partial J(r,t)}{\partial t} << c\left[\mu_a + (1-g)\mu_s\right] \Rightarrow \frac{\partial J(r,t)}{\partial t} \cong 0, \tag{A.10}$$

and as a result, Eq. (A.7) simplifies to the following form of Fick's Law:

$$\mathbf{J}(\mathbf{r},t) = -D\nabla\Phi(\mathbf{r},t), \tag{A.11}$$

where

$$D = \frac{1}{3\left[\mu_a + \mu_s'\right]}, \tag{A.12}$$

$$\mu_s' = (1-g)\mu_s. \tag{A.13}$$

D is the optical diffusion coefficient and μ_s' is known as the isotropic scattering coefficient. Finally, inserting Eq. (A.11) into Eq. (A.2) yields the time-domain diffusion equation of radiative transfer:[119]

$$\frac{1}{c}\frac{\partial\Phi(\mathbf{r},t)}{\partial t} - D\nabla^2\Phi(\mathbf{r},t) + \mu_a\Phi(\mathbf{r},t) = S(\mathbf{r},t). \tag{A.14}$$

A Fourier transfer of Eq. (A.14) yields the frequency-domain diffusion equation of radiative transfer:

$$\frac{i\omega}{c}\hat{\Phi}(\mathbf{r},\omega) - D\nabla^2\hat{\Phi}(\mathbf{r},\omega) + \mu_a\hat{\Phi}(\mathbf{r},\omega) = \hat{S}(\mathbf{r},\omega) \tag{A.15}$$

where $\hat{\Phi}(\mathbf{r},\omega)$ is the complex AC fluence at position $\mathbf{r}$ and angular frequency ω and can be expressed as:

$$\hat{\Phi}(\mathbf{r},\omega) = \mathrm{I}_{\mathrm{AC}}\exp(-i\theta) \tag{A.16}$$

where I_{AC} and θ represent the AC amplitude and phase lag relative to the source, respectively.

APPENDIX B: LAPLACE TRANSFORM SOLUTION TO THE COUPLED DIFFERENTIAL EQUATIONS OF THE THREE-COMPARTMENT PHARMACOKINETIC MODEL

The Laplace transform $g(s)$ of a function $f(t)$ is defined as

$$g(s) = \int_0^\infty \exp(-st) f(t)\, dt \tag{B.1}$$

where s is a complex variable and the function $f(t)$ is referred to as the inverse Laplace transform of $g(s)$. The Laplace transform and its inverse may be expressed in shorthand by use of the Laplace operator L as

$$g(s) = \mathrm{L}\left[f(t) \right], \tag{B.2}$$

$$f(t) = \mathrm{L}^{-1}\left[g(s) \right]. \tag{B.3}$$

Table B.1 provides the Laplace transform, and hence the inverse transform, of functions frequently encountered in the solution of the coupled, ordinary, linear differential equations that arise in the study of pharmacokinetics. In particular, the table of Laplace transforms is valuable in solving the differential equations that arise in the three-compartment pharmacokinetic model developed in Section 6.2.

The time dependent concentration of contrast agent in each of the three compartments – the blood, extravascular, extracellular space, and the cellular compartment (see Section 6.2), following intravenous bolus administration may be expressed as a set of three coupled, ordinary, linear differential equations given in

Table B.1. Table of Laplace transforms.[120]

α, β, γ are constants (rate constants)

s is the Laplace complex variable

x is a time-dependent variable (concentration)

$\overline{x}$ is the Laplace transform of a time-dependent variable

x_o is the initial condition, i.e. the value of x at $t = 0$

time function, $f(t) = \mathrm{L}^{-1}\left[g(s)\right]$	Laplace transform, $g(s) = \mathrm{L}\left[f(t)\right]$
$\frac{dx}{dt}$	$s\overline{x} - x_o$
$\frac{\exp(-\alpha t) - \exp(-\beta t)}{\beta - \alpha}$	$\frac{1}{(s+\alpha)(s+\beta)}$
$\frac{\alpha - \gamma}{\alpha - \beta}\exp(-\alpha t) + \frac{\beta - \gamma}{\beta - \alpha}\exp(-\beta t)$	$\frac{s+\gamma}{(s+\alpha)(s+\beta)}$
$\frac{1}{\alpha\beta} + \frac{\beta\exp(-\alpha t) - \alpha\exp(-\beta t)}{\alpha\beta(\alpha - \beta)}$	$\frac{1}{s(s+\alpha)(s+\beta)}$

Section 6.2 by Eqs. (6.3), (6.4), and (6.5). Performing the Laplace transform on the differential equations and applying the appropriate initial conditions results in the following expressions:

$$s\overline{C_B} - C_{Bo} = -k_B\overline{C_B} + k_r\overline{C_{EES}}\,, \tag{B.4}$$

$$s\overline{C_{EES}} = -k_{EES}\overline{C_{EES}} + k_p\overline{C_B}\,, \tag{B.5}$$

$$s\overline{C_c} = -k_c\overline{C_{EES}}\,. \tag{B.6}$$

Upon algebraic manipulation, Eqs. (B.4 – B.6) may be rewritten with only the Laplace-transformed concentration terms on the left-hand side.

$$\overline{C_B} = \frac{(s + k_{EES})C_{Bo}}{(s+\alpha)(s+\beta)}, \tag{B.7}$$

$$\overline{C_{EES}} = \frac{k_p C_{Bo}}{(s+\alpha)(s+\beta)}, \tag{B.8}$$

$$\overline{C_c} = \frac{k_c k_p C_{Bo}}{s(s+\alpha)(s+\beta)}, \tag{B.9}$$

where

$$\alpha = \tfrac{1}{2}\left[k_{EES} + k_B + \sqrt{(k_{EES} - k_B)^2 + 4k_r k_p} \right], \tag{B.10}$$

$$\beta = \tfrac{1}{2}\left[k_{EES} + k_B - \sqrt{(k_{EES} - k_B)^2 + 4k_r k_p} \right]. \tag{B.11}$$

Performing the inverse Laplace transform on Eqs. (B.7), (B.8) and (B.9) using the appropriate relationships provided in Table B.1 facilitates the straightforward solution to the system of differential equations. Thus, the time-dependent concentration of dye in each of the three-compartments may be expressed as:

$$C_{EES} = \frac{k_p C_{Bo}\left[\exp(-\beta t) - \exp(-\alpha t)\right]}{\alpha - \beta}, \tag{B.12}$$

$$C_B = \frac{C_{Bo}}{\alpha - \beta}\left[(\alpha - k_{EES})\exp(-\alpha t) - (\beta - k_{EES})\exp(-\beta t)\right], \tag{B.13}$$

$$C_c = \frac{k_p k_c C_{Bo}}{\alpha\beta}\left[1 + \frac{\beta\exp(-\alpha t) - \alpha\exp(-\beta t)}{\alpha - \beta}\right]. \tag{B.14}$$

Furthermore, the observed time-dependent fluorescent intensity may be expressed as a weighted sum of the concentration of dye in each compartment

$$I(t) \cong w_1 C_B + w_2 C_{EES} + w_3 C_C . \tag{B.15}$$

Combining Eqs. (B.12), (B.13), (B.14), and (B.15) enables the time-dependent fluorescent intensity to be written in the form of a double-exponential, five-parameter expression

$$I(t) = I_o + A\left[1 - \exp(-\alpha t)\right] + B\left[1 - \exp(-\beta t)\right], \tag{B.16}$$

where the parameters are given by

$$I_o = w_1 C_{Bo} , \tag{B.17}$$

$$A = \frac{C_{Bo}}{\alpha - \beta}\left[k_p w_2 - (\alpha - k_{EES}) w_1 - \frac{k_c k_p w_3}{\alpha} \right], \tag{B.18}$$

$$B = \frac{C_{Bo}}{\alpha - \beta}\left[(\beta - k_{EES}) w_1 - k_p w_2 + \frac{k_c k_p w_3}{\beta} \right], \tag{B.19}$$

and α and β are complex rate constants previously defined by Eqs. (B.10) and (B.11). Finally, as discussed in Section 6.2, Eq. (B.16) may be further simplified to a four-parameter expression by employing a background subtraction technique, the mathematically equivalent of setting I_o equal to zero.

VITA

MIKHAIL GURFINKEL

PERMANENT ADDRESS

Texas A&M University
Department of Chemical Engineering
College Station, TX 77843-3122

EDUCATION

Texas A&M University, College Station, TX
Ph.D., Chemical Engineering, May 2004

University of Oklahoma, Norman, OK
B.S., Biochemistry, Special Distinction, May 1998

SELECTED PUBLICATIONS

M. Gurfinkel, S. Ke, W. Wang, C. Li, and E.M. Sevick-Muraca, "Imaging pharmacokinetics of molecularly targeted diagnostics and therapeutics," submitted to *Nat. Biotech.* (2003).

M. Gurfinkel, T. Pan, and E.M. Sevick-Muraca, "Determination of optical properties of semi-infinite turbid media using area measurements of frequency-domain photon migration obtained with an ICCD detection system," submitted to *J. Biomed. Opt.* (2003).

S. Ke, X. Wen, M. Gurfinkel, C. Charnsangavej, Z. Fan, S. Wallace, E. M. Sevick-Muraca and C. Li, "Near-infrared optical imaging of epidermal growth factor receptors (EGFr) in a breast cancer xenograft," *Cancer Res.*, accepted (2003).

M. Gurfinkel, S. Ke, X. Wen, C. Li, and E.M. Sevick-Muraca, "Near-infrared fluorescence optical imaging and tomography," *Disease Markers*, accepted (2003).

M. Gurfinkel, A. B. Thompson, W. Ralston, T. L. Troy, A. L. Moore, T. A. Moore, J. D. Gust, D. Tatman, J. S. Reynolds, B. Muggenburg, K. Nikula, R. Pandey, R. H. Mayer, D. J. Hawrysz and E. M. Sevick-Muraca, "Pharmacokinetics of ICG and HPPH-car for the detection of normal and tumor tissue using fluorescence, near-infrared reflectance imaging: a case study," *Photochem. Photobiol.* **72**(1), 94-102 (2000).